UC Davis
UC Davis Electronic Theses and Dissertations

Title
Inertial Force Actuator Applications for Active Vehicle Suspensions

Permalink
https://escholarship.org/uc/item/0q22n9qj

Author
McCrone, David Jordan

Publication Date
2022

Peer reviewed|Thesis/dissertation

eScholarship.org Powered by the California Digital Library
University of California

Inertial Force Actuator Applications for Active Vehicle Suspensions

By

D. JORDAN McCRONE
DISSERTATION

Submitted in partial satisfaction of the requirements for the degree of

DOCTOR OF PHILOSOPHY

in

Mechanical and Aerospace Engineering

in the

OFFICE OF GRADUATE STUDIES

of the

UNIVERSITY OF CALIFORNIA

DAVIS

Approved:

Donald L. Margolis, Chair

Dean C. Karnopp

Zhaodan Kong

Committee in Charge

2022

© D. Jordan McCrone, 2022. All rights reserved.

To...

Contents

List of Figures vi

List of Tables xi

List of Acronyms xii

Abstract xiii

Acknowledgments xiv

Chapter 1. Background 1

Chapter 2. Introduction 7

2.1. A Skyhook / Groundhook MIMO Baseline Analysis 7

2.2. Investigation of Optimal Control of Inertial Force Actuator 18

Chapter 3. Methods 23

3.1. Tire Model 23

3.1.1. Dugoff Model 23

3.1.2. Modified Dugoff 25

3.2. Simulated Roadways 26

3.3. Model Predictive Control 29

3.3.1. Discretizing the vehicle dynamic system model 30

3.3.2. Preparing the Model Predictive Control 31

3.4. The Inertial Force Actuator Model 35

3.5. High Order Vehicle Simulation Model 39

3.5.1. Sprung Mass 39

3.5.2. Suspensions 40

3.5.3. Wheel Rotational Model 41
3.5.4. Tire-Road Interaction 42
3.5.5. Full Set of Equations of Motion 42

Chapter 4. Simulation Study With the Quarter Car Model 47
4.1. Determination of Appropriate Horizon 47
4.2. Quarter Car With Fully Active Suspension Actuator 50
4.2.1. Varying α_a (weighting on the sprung mass acceleration) 51
4.2.2. Varying α_t (weighting on the tire deflection) 53
4.3. Quarter Car With Semi-Active Suspension Actuator 56
4.3.1. Varying α_a (weighting on the sprung mass acceleration) 57
4.3.2. Varying α_t (weighting on the tire deflection) 60
4.4. Quarter Car Traversing a Bump 63
4.4.1. Fully Active 64
4.4.2. Semi-Active 68
4.5. Discussion 71

Chapter 5. Validation With High Order Model 73
5.1. Step Steer Traversing a Random Road 74
5.1.1. Fully Active Suspension 74
5.1.2. Semi-Active Suspension 82
5.2. Discussion of Results 90

Chapter 6. Conclusions 92
6.1. Future Work 93

Appendix A. Additional Plots and Figures 94
A.1. Additional plot outputs for section 2.1 94
A.2. Additional plot outputs for section 4.2.1 95
A.3. Additional plot outputs for section 4.2.2 98
A.4. Additional plot outputs for section 4.3.1 99
A.5. Additional plot outputs for section 4.3.2 103

A.6. Additional plot outputs for section 4.4.1 106
A.7. Additional plot outputs for section 4.4.2 107

Bibliography 109

List of Figures

1.1 Quarter Car model 2

1.2 Skyhook Quarter Car model 2

1.3 Groundhook Quarter Car model 2

1.4 Velocity Response of Passive vs Skyhook 3

1.5 Acceleration Response of Passive vs Skyhook, Groundhook 4

1.6 Dynamic Tire Response of Passive vs Skyhook, Groundhook 5

2.1 Skyhook model reference 7

2.2 Ideal Skyhook and Groundhook model 8

2.3 Actuated system model 9

2.4 Frequency response plots. 13

2.5 1-DoF actuator 14

2.6 Tire Velocity Magnitude Frequency Responses 14

2.7 Sprung Velocity Magnitude Frequency Responses 15

2.8 Actuator Displacement 17

2.9 Actuator travel when a high-pass filter is applied to F_a 17

2.10 Model of actuated system for optimal control 18

2.11 Magnitude Frequency Response Plots - Linear Quadratic Regulator 20

2.12 Actuator Dissipated Energy 22

3.1 Dugoff Tire Model 24

3.2 Dugoff vs Magic Formula 24

3.3 Modified Dugoff F_y level sets 25

3.4 Modified Dugoff α level sets 25

3.5 Class B road profile 27

3.6 Class B road velocity input 27
3.7 Various Road PSDs 28
3.8 Road Spatial Velocity PSDs 28
3.9 Model of proposed actuator 35
3.10 Actuator Force Magnitude Frequency Response - L vs No L 36
3.11 Actuator Force Magnitude Frequency Response 38
3.12 Sprung Mass schematic 39
3.13 Sprung mass bond graph 40
3.14 Vertical suspension diagram and bond graph fragment. 41
3.15 Schematic and Bond Graph fragment of rotating wheel. 41
3.16 Bond Graph fragment of tire resistor field. 42
3.17 Wheel center point lateral velocity bond graph 43
3.18 Wheel center point longitudinal velocity bond graph 43

4.1 Choosing Horizon - Acceleration vs N 48
4.2 Choosing Horizon - Tire Displacement vs N 49
4.3 Choosing Horizon - Suspension Disp. vs N 49
4.4 Choosing Horizon - IFA Disp. vs N 50
4.5 Choosing Horizon - Power vs N 50
4.6 Sprung Mass Acceleration FFT - Varying α_a 51
4.7 Tire Deflection FFT - Varying α_a 52
4.8 Total Combined Power - Varying α_a 52
4.9 Total Energy Required - Varying α_a 53
4.10 Sprung Mass Acceleration FFT - Varying α_t 54
4.11 Tire Deflection FFT - Varying α_t 54
4.12 Total Combined Power - Varying α_t 55
4.13 Suspension Actuator Force - Varying α_t 55
4.14 IFA Force - Varying α_t 56
4.15 Total Energy Required - Varying α_t 56
4.16 Sprung Mass Acceleration FFT - Varying α_a 57

4.17 Tire Deflection FFT - Varying α_a 58
4.18 Suspension Actuator Force - Varying α_a 58
4.19 Inertial Force Actuator (IFA) Force - Varying α_a 59
4.20 Suspension Actuator Power - Varying α_a 59
4.21 IFA Energy Required - Varying α_a 60
4.22 Sprung Mass Acceleration FFT - Varying α_t 61
4.23 Tire Deflection FFT - Varying α_t 61
4.24 IFA Power - Varying α_t 62
4.25 Total Energy Required - Varying α_t 62
4.26 Bump Profile - Varying α_a 63
4.27 Sprung Mass Acceleration - Single Bump, Fully Active 64
4.28 Sprung Mass Velocity - Single Bump, Fully Active 65
4.29 Tire Displacement - Single Bump, Fully Active 65
4.30 IFA Displacement - Single Bump, Fully Active 66
4.31 IFA Force - Single Bump, Fully Active 66
4.32 Suspension Actuator Force - Single Bump, Fully Active 67
4.33 Sprung Mass Acceleration - Single Bump, Semi Active 68
4.34 Sprung Mass Velocity - Single Bump, Semi Active 68
4.35 Tire Displacement - Single Bump, Semi Active 69
4.36 IFA Displacement - Single Bump, Semi Active 69
4.37 Suspension Displacement - Single Bump, Semi Active 70
4.38 IFA Force - Single Bump, Semi Active 71
4.39 Suspension Actuator Force - Single Bump, Semi Active 71

5.1 Vertical Acceleration, high order model 74
5.2 Vehicle Yawrate, high order model 75
5.3 Sprung Mass Vertical Velocity, high order model 75
5.4 Lateral Acceleration, high order model 76
5.5 IFA Displacement, high order model 77
5.6 Tire Spring Displacement, high order model 78

5.7 Suspension Displacement, high order model 79
5.8 IFA Voltage Input, high order model 80
5.9 Suspension Force Input, high order model 81
5.10 Vertical Acceleration, high order model 82
5.11 Vehicle Yawrate, high order model 83
5.12 Sprung Mass Vertical Velocity, high order model 83
5.13 Lateral Acceleration, high order model 84
5.14 IFA Displacement, high order model 85
5.15 Tire Spring Displacement, high order model 86
5.16 Suspension Displacement, high order model 87
5.17 IFA Voltage Input, high order model 88
5.18 Suspension Force Input, high order model 89
5.19 Pareto Front 91

A.1 Quarter Car model 94
A.2 Sprung Mass Acceleration - Varying α_a 95
A.3 Tire Deflection - Varying α_a 95
A.4 Inertial Force Actuator Deflection - Varying α_a 96
A.5 Suspension Deflection - Varying α_a 96
A.6 Suspension Actuator Force - Varying α_a 97
A.7 Inertial Force Actuator Force - Varying α_a 97
A.8 Sprung Mass Acceleration - Varying α_t 98
A.9 Tire Deflection - Varying α_t 98
A.10 Inertial Force Actuator Deflection - Varying α_t 99
A.11 Suspension Deflection - Varying α_t 99
A.12 Sprung Mass Acceleration - Varying α_a 100
A.13 Tire Deflection - Varying α_a 100
A.14 Suspension Deflection - Varying α_a 101
A.15 Inertial Force Actuator Deflection - Varying α_a 101
A.16 IFA Power - Varying α_a 102

A.17 Sprung Mass Acceleration - Varying α_t 103
A.18 Tire Deflection - Varying α_t 103
A.19 Inertial Force Actuator Deflection - Varying α_t 104
A.20 Suspension Deflection - Varying α_t 104
A.21 Suspension Actuator Force - Varying α_t 105
A.22 IFA Force - Varying α_t 105
A.23 Suspension Displacement - Single Bump, Fully Active 106
A.24 Total Actuator Power - Single Bump, Fully Active 106
A.25 Total Actuator Energy - Single Bump, Fully Active 107
A.26 IFA Actuator Power - Single Bump, Semi Active 107
A.27 IFA Energy - Single Bump, Semi Active 108

List of Tables

2.1 Parameter values for passive elements of quarter car 12

2.2 Parameters for virtual elements used for control of MIMO Skyhook+Groundhook 12

2.3 Feedforward control results 18

2.4 Optimal control results 21

3.1 Definitions for variables used in equations of motion 44

5.1 High Order Simulation Results - Fully Active 74

5.2 High Order Simulation Results - Semi-Active 82

List of Acronyms

CG	Center of Gravity
DoF	Degree of Freedom
FFT	Fast Fourier Transform
IFA	Inertial Force Actuator
LQR	Linear Quadratic Regulator
MIMO	Multi-Input, Multi-Output
MPC	Model Predictive Control
MR	Model Reference
ODE	Ordinary Differential Equation
PSD	Power Spectral Density
QC	Quarter Car
RMS	Root Mean Square
TVA	Tuned Vibration Absorber

Abstract

The application of Inertial Force Actuators (IFAs) to vehicle dynamics is investigated. These are modeled as translational motors with a small proof mass attached such that forces applied by the actuator to the vehicle result in motion of the proof mass in inertial space. IFAs are shown to provide specific benefits compared to traditional active suspensions, which exhibit deleterious effects on secondary vehicle signals while pursuing their primary objectives. Since IFAs can be high power and generate high force magnitudes, and are constrained only by their internal stroke and force limits, their application is well suited for zero-mean band-limited white noise inputs such as from a vehicle roadway. The suspension control problem is studied with the incorporation of IFAs in cooperation with traditional actuators in order to meet the vehicle objectives hierarchy. Modern and classical control theory investigate the application of IFAs to control various vehicle output signals. High order vehicle simulation models are generated, and used to validate the controlled system.

Acknowledgments

To Professor Margolis, who has taken every opportunity to share his knowledge and experience.

To my grandfather, whose gentle nudging guided my path toward engineering.

To my father, whose confident encouragement kept me moving forward.

To my friends and family, to whom I owe the deepest debt of gratitude for the unwavering love and support that has been critical to this effort.

CHAPTER 1

Background

Automobile performance represents a major field for research and development in mechanical engineering. Despite their ubiquity and public familiarity, road vehicles are enormously advanced platforms for development, and much of this development is abstracted from the user by the successes of the purpose of the various subsystems that perform tasks such as stabilization, traction control, active suspensions, and many others. The intended purpose of these subsystems usually falls onto a spectrum, the two ends of which are passenger comfort (or ride, as described by the automotive engineer) or vehicle performance (or handling). Luxury vehicle manufacturers tend to focus on ride, while sports car manufacturers tend to focus on handling.

The primary objectives of vehicle suspensions (passive and active) involve four aspects: suspend the vehicle above the road, maintain relatively constant nominal posture with respect to the road, maintain tractive normal force between the tires and the road, and isolate the vehicle from undesired road-induced vibration [**26**]. Conventional passive suspensions contain hardware traditionally consisting of two devices: a spring element k_s, which generates a force related to a relative displacement; and a damper element b, which generates a force related to a relative velocity. Both these elements are attached between the wheel (the *unsprung mass*, m_{us}) and the vehicle body (the *sprung mass*, m_s). The tire can also be considered part of the passive suspension, since its representation for vertical dynamics is also a spring, k_t, acting between the unsprung mass and the road. This configuration is represented by a low order model known as a Quarter Car (QC) (Figure 1.1).

Although the passive suspension configuration described is convenient for compact packaging, it has drawbacks. Analysis of QC models reveals them as having undesirable resonance in the low frequency passband, as well as undesirable high frequency isolation performance [**15**]. From the framework of random process theory, it was found that optimal frequency response characteristics

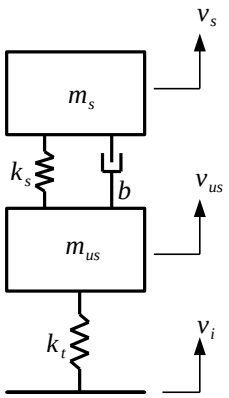

FIGURE 1.1. Quarter Car model

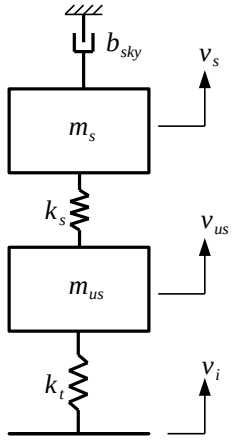

FIGURE 1.2. Skyhook Quarter Car model

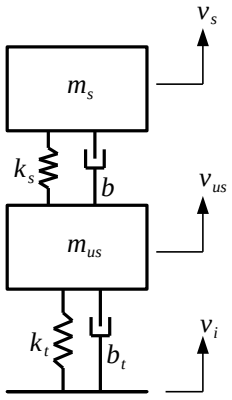

FIGURE 1.3. Groundhook Quarter Car model

are achieved when the damper location is between inertial space and the mass for a single Degree of Freedom (DoF) mechanical resonator [**15**]. This is known as a Skyhook damping (Figure 1.2).

When applied to the 2 DoF quarter car, the Skyhook configuration results in better passband performance with a less pronounced 1st resonance peak, and faster isolation roll-off at the cost of an less damping in the wheel hop mode. Figure 1.4 shows that there is some benefit of maintaining some passive damping between the sprung and unsprung masses in the conventional location, since tire oscillation (2nd resonance) is more damped, although the resulting sprung mass velocity magnitudes are increased in some regions, and high-frequency roll-off benefits of Skyhook are reduced. Also, although no physically realizable passive Skyhook suspension for vehicles has been developed, it serves as an optimal structural configuration for model reference of a controlled suspension, and has been the baseline for vehicle active suspensions for several decades.

Lateral and longitudinal vehicle performance is associated with maintaining a near-constant normal force between the tires and the road. This is due to the nonlinear, concave constitutive relationship between tire-road normal force and lateral and longitudinal tire force [**16**]; compared to a linear relationship between normal and in-plane tire forces, when the relationship is concave and a tire dithers its normal force about a nominal amplitude, the in-plane tire forces are reduced. For this reason, actuators placed in the conventional location (between the unsprung and sprung

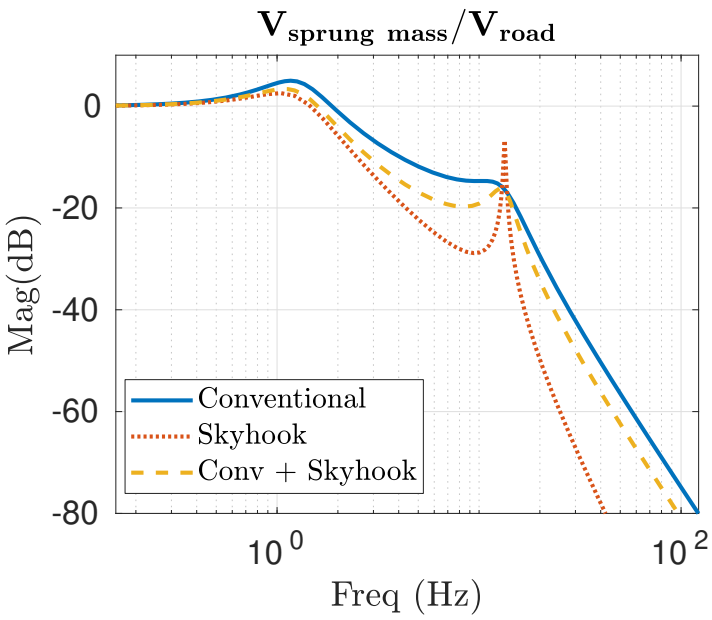

FIGURE 1.4. Frequency response of Conventional passive (Figure 1.1), Skyhook (Figure 1.2), and Skyhook with an included conventional suspension damper (combination of Figures 1.1 and 1.2)

mass, parallel with the suspension spring and damper) inevitably deteriorate vehicle handling performance. This is a well recognized phenomenon [**23**] that is a structural limitation of conventional active suspension configurations manifested as an inverse performative relationship between ride comfort and tire dynamic load (which correlates with vehicle agility). With respect to performance trade-offs associated with active dampers, it has been observed that the trade-offs could be mitigated if one could exert forces more arbitrarily on a vehicle [**15**].

Groundhook [**27**], inspired by Skyhook, originally sought to minimize damage to roadways from heavy trucks. However, by reducing the dynamic tire force transmitted to the road, Groundhook found benefit for handling performance purposes, since large values of dynamic tire force also deteriorate road-holding. The Groundhook model (Figure 1.3) serves as an idealized passive model reference to minimize tire normal force variations due to road-normal velocity inputs, v_i. In reality, the tire damping of Groundhook is difficult to implement with a passive element [**17**]. Therefore, like Skyhook, Groundhook is realized through an active- or semi-active suspension designed to track

a Model Reference (MR) containing a virtual damper in series with the tire spring (parameter b_t in Figure 1.3).

In order to physically realize ideal Skyhook and ideal Groundhook, the systems of Figures 1.2 and 1.3 are often used as a MR (or target reference) for a force actuator in series with the suspension to follow. The drawback of this simple configuration is that when one objective (tire deflection or sprung mass velocity) is followed, the other deteriorates. Figures 1.5 and 1.6 depict the magnitude frequency responses for sprung mass acceleration to input velocity. These were done through simulations in which an active actuator between the unsprung and sprung masses is targetting the MRs of Figures 1.2 and 1.3. The plots compare the performances of having Skyhook or Groundhook as a target. The subsequent deterioration of the untargeted signal with respect to the passive setup is noted through Root Mean Square (RMS) values of the alternative signals.

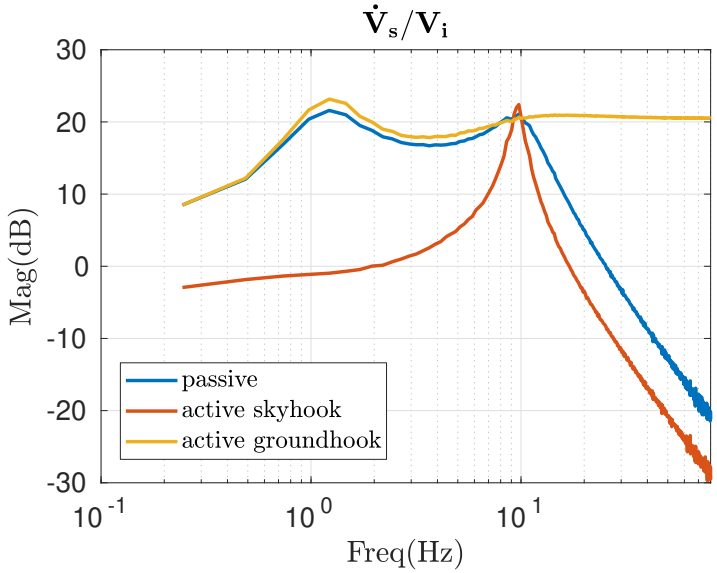

FIGURE 1.5. Magnitude frequency response of Conventional passive (Figure 1.1), Skyhook (Figure 1.2), and Groundhook(Figure 1.3). The RMS value of acceleration for the active skyhook is about half that of the passive; the RMS value of acceleration for the active groundhook is about double that of the passive.

Efforts have been made to mitigate the known performance and handling trade-offs observed in conventional active suspensions. Human comfort from vertical dynamics has highest sensitivity in the 4-8 Hz Frequency band [**13**], while tire sensitivity is highest at its resonance, usually

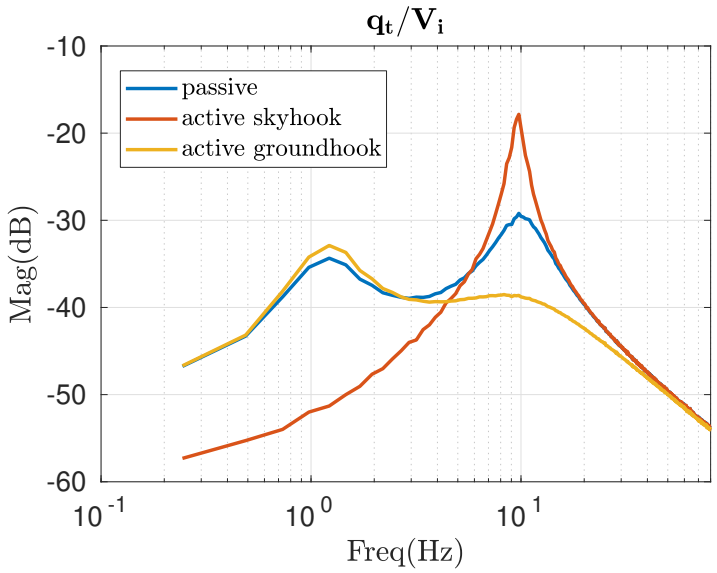

FIGURE 1.6. Magnitude frequency response of Conventional passive (Figure 1.1), Skyhook (Figure 1.2), and Groundhook(Figure 1.3). The RMS value of tire deflection for the active groundhook is about double that of the passive; the RMS value of tire deflection for the active groundhook is about half that of the passive.

around 8-13 Hz. Researchers have tried frequency-dependent hybrid Skyhook control which seeks to minimize the deterioration at their respective resonant frequencies [**24**]. Others applied H_∞ optimal control techniques to a quarter car with a conventional semi-active actuator and compared results to Skyhook control, and found that the high-order H_∞ controller produced could provide a more comfortable ride across a wider band of frequencies [**21**]. These techniques still result in a performance trade-off, however the designer has more control over the frequency response shape.

Theoretical research has been conducted on energy regeneration capabilities of active suspensions . Experimental results show that the unmodeled energy dissipative (resistive) elements of actuators results in significantly less regeneration capability than theoreticians predict.

Measurements of road elevation profiles indicate that vertical input from the road can be modeled as a white noise stochastic process with a flat power spectral density (PSD) in the velocity [**14**]. The vertical velocity PSD is determined by forward vehicle speed and a static road roughness coefficient. The road unevenness enters the vehicle as a disturbance, and degrades both the ride comfort

and vehicle handling objectives. However, since physical roadway inputs are well characterized, new vehicle system research is well-suited for simulation studies.

IFAs have been applied to a wide array vibrations problems. In structural systems they are used as active force generators to counteract structural resonances where a simple Tuned Vibration Absorber (TVA) would be insufficient, or where the dynamic properties of complex structures are variable [**9**]. Other researchers have utilized such actuators for automotive applications to minimize structure-borne acoustic noise [**5**] . In another pair of studies, IFAs were analyzed for generic structural vibration isolation [**6**] [**7**]. These studies made the observation that inertial actuators should have a natural frequency that is lower that the natural frequency of the system to be isolated for best performance. The application of an inertial actuator to control vibration of a single DoF mechanical resonator has also been investigated using velocity feedback (similar to Skyhook) [**11**]. Their main interest was in comparing performance of an inertial actuator to an actuator in parallel with the resonator spring, and identifying conditions under which the controlled system remained stable. Also for vibration isolation of a generic single DoF mechanical resonator, Ref [**30**] developed a velocity feedback algorithm that showed reduced vibration of the system. They analyzed the system stability and performance trade-offs, and investigated the conditions under which the inertial actuator would harvest or dissipate power. IFAs have even been proposed for stability purposes on high speed trains [**29**] .

Due to the trade-offs between handling and comfort, and the structural limitations of the conventional actuator configuration, this research proposes the application of IFAs for active control of vehicles. In particular, the focus will be on applying these actuators in Multi-Input, Multi-Output (MIMO) arrangements with conventional active suspensions. The purpose is to allow for the application of inertial forces onto the vehicle by the reactive force of pushing on the small inertia.

.

CHAPTER 2

Introduction

2.1. A Skyhook / Groundhook MIMO Baseline Analysis

Given that Skyhook is the gold standard comparison for active suspension systems, this research begins with the analysis of a Skyhook + Groundhook system utilizing both conventional and inertial actuators in a Multi-Input, Multi-Output (MIMO) design. We begin with the development of a Model Reference (MR). A schematic of the proposed MR is shown in Figure 2.2, along with a bond graph of the system. Equations are derived, resulting in the linear state space model shown in Equation 2.1.

From these equations, the transfer functions $\frac{v_s}{v_i}|_{des}(s)$ and $\frac{v_i - v_{us}}{v_i}|_{des}(s)$ are derived, and will be used to generate controllers for the active system desribed below. These represent the sprung mass velocity response and the dynamic tire velocity response of the MR.

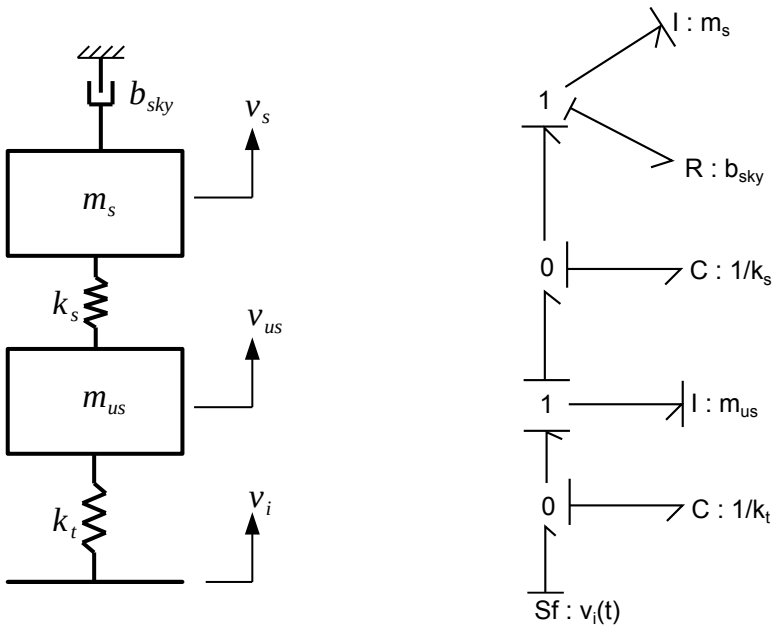

FIGURE 2.1. Skyhook QC model

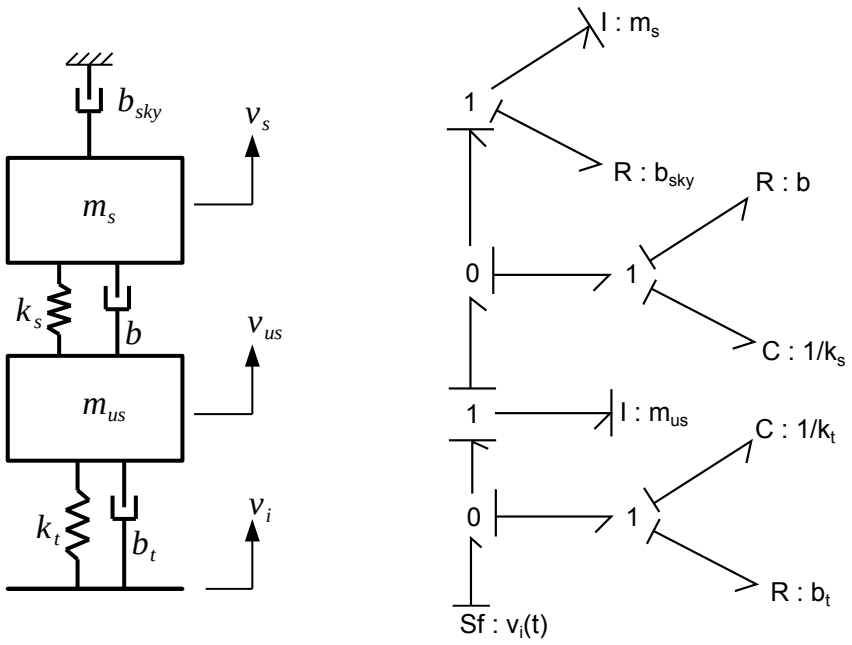

FIGURE 2.2. Ideal Skyhook and Groundhook model

$$\begin{bmatrix} \dot{q_t} \\ \dot{q_s} \\ \dot{p_s} \\ \dot{p_{us}} \end{bmatrix} = \begin{bmatrix} 0 & 0 & 0 & \frac{-1}{m_{us}} \\ 0 & 0 & -\frac{-1}{m_s} & -\frac{1}{m_{us}} \\ 0 & k_s & \frac{-b_s - b_{sky}}{m_s} & \frac{b_s}{m_{us}} \\ k_t & -k_s & \frac{b_s}{m_s} & \frac{-b_s - b_t}{m_{us}} \end{bmatrix} \begin{bmatrix} q_t \\ q_s \\ p_s \\ p_{us} \end{bmatrix} + \begin{bmatrix} 1 \\ 0 \\ 0 \\ b_t \end{bmatrix} v_i \tag{2.1}$$

$$\frac{v_s}{v_i}|_{des}(s) = \frac{bb_t s^2 + (k_t b + b_t k_s)s + k_s k_t}{\Delta_{MR}} \tag{2.2}$$

(2.3)

$$\frac{v_i - v_{us}}{v_i}|_{des}(s) = \frac{m_s m_{us} s^4 + (bm_s + bm_{us} + b_{sky} m_{us})s^3 + (bb_{sky} + k_s m_s + k_s m_{us})s^2 + b_{sky} k_s s}{\Delta_{MR}}$$

where

$$\begin{aligned} \Delta_{MR} = {} & m_s m_{us} s^4 + (bm_s + b_t m_s + bm_{us} + b_{sky} m_{us})s^3 \\ & \cdots + (bb_t + bb_{sky} + b_t b_{sky} + k_s m_s + k_t m_s + k_s m_{us})s^2 \\ & \cdots + (b_t k_s + b_{sky} k_s + bk_t + b_{sky} k_t)s + k_s k_t \end{aligned} \tag{2.4}$$

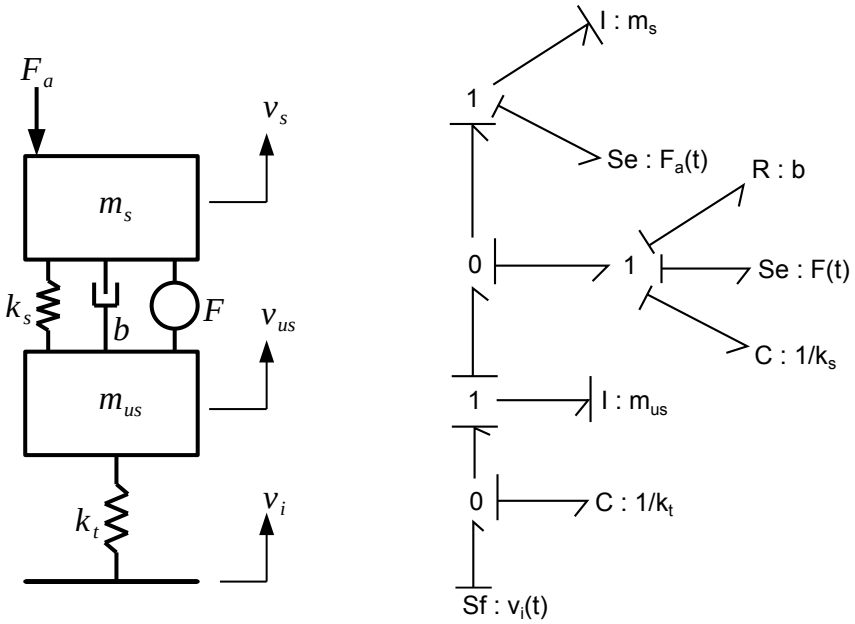

FIGURE 2.3. Actuated system model

The actuated system model to be controlled is shown in Figure 2.3, along with a bond graph derived from the schematic. Again, bond graphs are used to generate state space Equations (2.5).

$$\begin{bmatrix} \dot{q}_t \\ \dot{q}_s \\ \dot{p}_s \\ \dot{p}_{us} \end{bmatrix} = \begin{bmatrix} 0 & 0 & 0 & \frac{-1}{m_{us}} \\ 0 & 0 & -\frac{-1}{m_s} & -\frac{1}{m_{us}} \\ 0 & k_s & \frac{-b_s}{m_s} & \frac{b_s}{m_{us}} \\ k_t & -k_s & \frac{b_s}{m_s} & \frac{-b_s}{m_{us}} \end{bmatrix} \begin{bmatrix} q_t \\ q_s \\ p_s \\ p_{us} \end{bmatrix} + \begin{bmatrix} 1 & 0 & 0 \\ 0 & 0 & 0 \\ 0 & 1 & -1 \\ 0 & -1 & 0 \end{bmatrix} \begin{bmatrix} v_i \\ F \\ F_a \end{bmatrix} \tag{2.5}$$

From this model, we derive the following transfer functions:

$$\frac{v_s}{v_i}(s) = \frac{(bk_t)s + k_s k_t}{\Delta} \tag{2.6}$$

$$\frac{v_s}{F}(s) = \frac{m_{us}s^3 + k_t s}{\Delta} \tag{2.7}$$

$$\frac{v_s}{F_a}(s) = \frac{-m_{us}s^3 - bs^2 + (-k_s + k_t)s}{\Delta} \tag{2.8}$$

$$\frac{v_i - v_{us}}{v_i}(s) = \frac{m_s m_{us}s^4 + (bm_s + bm_{us})s^3 + (k_s m_s + k_s m_{us})s^2}{\Delta} \tag{2.9}$$

$$\frac{v_i - v_{us}}{F}(s) = \frac{m_s s^3}{\Delta} \tag{2.10}$$

$$\frac{v_i - v_{us}}{F_a}(s) = \frac{bs^2 + k_s s}{\Delta} \tag{2.11}$$

where

$$\Delta = m_s m_{us} s^4 + (b_s m_s + b_s m_{us}) s^3 + (k_s m_s + k_t m_s + k_s m_{us}) s^2 + b_s k_t s + k_s k_t \tag{2.12}$$

These equations relate the outputs of interest (sprung mass velocity and tire spring velocity) to the controlled inputs (F and F_a) and the disturbance input (v_i). It should be noted that the inertial force, F_a, will ultimately come from an inertial proof mass actuator. To develop the control, it is recognized that the total responses of the outputs will be a superposition of the inputs multiplied by the respective transfer functions of Equation 2.11; and since the control forces are still undetermined, the outputs are now arbitrarily forced to be equal to the MR inputs:

$$\begin{aligned} v_s(s) &= \frac{v_s}{v_i}(s)v_i(s) + \frac{v_s}{F}(s)F(s) + \frac{v_s}{F_a}(s)F_a(s) &&= \left.\frac{v_s}{v_i}\right|_{des}(s)v_i(s) \\ v_i - v_{us}(s) &= \frac{v_i - v_{us}}{v_i}(s)v_i(s) + \frac{v_i - v_{us}}{F}(s)F(s) + \frac{v_i - v_{us}}{F_a}(s)F_a(s) &&= \left.\frac{v_i - v_{us}}{v_i}\right|_{des}(s)v_i(s) \end{aligned} \tag{2.13}$$

Rearranging these equations results in the matrix form of Equation 2.14. The matrix at the left hand side of Equation 2.14 can be inverted and multiplied on both sides, leaving only the actuator forces transfer function matrix that provide the feedforward control forces required on each of the actuators in order to track the MR (Equations 2.15 and 2.16).

$$\begin{bmatrix} \frac{v_s}{F}(s) & \frac{v_s}{F_a}(s) \\ \frac{v_i - v_{us}}{F}(s) & \frac{v_i - v_{us}}{F_a}(s) \end{bmatrix} \begin{bmatrix} F(s) \\ F_a(s) \end{bmatrix} = \begin{bmatrix} \left.\frac{v_s}{v_i}\right|_{des} - \frac{v_s}{v_i}(s) \\ \left.\frac{v_{us} - v_s}{v_i}\right|_{des} - \frac{v_i - v_{us}}{v_i}(s) \end{bmatrix} v_i(s) \tag{2.14}$$

The inversion produces the control laws below.

$$F(s) = \frac{num_F}{den_c} \tag{2.15}$$

$$F_a(s) = \frac{num_{F_a}}{den_c} \tag{2.16}$$

(2.17)

$$num_F = (-2m_s{m_{us}}^2)s^5 + (-2bm_{us}{}^2 - 2b_{sky}m_{us}{}^2 - 4bm_sm_{us} - b_tm_sm_{us})s^4$$
$$\cdots + \Big(- 2b^2m_s - 2b^2m_{us} - 2k_sm_{us}{}^2 - bb_tm_s - bb_tm_{us} - 4bb_{sky}m_{us} - b_tb_{sky}m_{us}$$
$$\cdots - 4k_sm_sm_{us} - 2k_tm_sm_{us}\Big)s^3 + \Big(- 2b^2b_{sky} - bb_tb_{sky} - 4bk_sm_s - b_tk_sm_s - 2bk_tm_s$$
$$\cdots - 4bk_sm_{us} - b_tk_sm_{us} - 4b_{sky}k_sm_{us} - 2bk_tm_{us} - 2b_{sky}k_tm_{us}\Big)s^2 + \Big(- 2k_s{}^2m_s$$
$$\cdots - 2k_s{}^2m_{us} - 4bb_{sky}k_s - b_tb_{sky}k_s - 2bb_{sky}k_t - 2k_sk_tm_s - 2k_sk_tm_{us}\Big)s$$
$$\cdots - (2b_{sky}k_s{}^2 + 2b_{sky}k_tk_s)$$

(2.18)

$$num_{F_a} = \Big(- 2m_s{m_{us}}^2\Big)s^5 - \Big(2bm_{us}{}^2 + 2b_{sky}m_{us}{}^2 + 2bm_sm_{us} + b_tm_sm_{us}\Big)s^4$$
$$\cdots - \Big(2k_sm_{us}{}^2 + bb_tm_s + bb_tm_{us} + 2bb_{sky}m_{us} + b_tb_{sky}m_{us} + 2k_sm_sm_{us} + 2k_tm_sm_{us}\Big)s^3$$
$$\cdots - \Big(b_tk_sm_s + 2bk_tm_s + b_tk_sm_{us} + 2b_{sky}k_sm_{us} + 2bk_tm_{us} + 2b_{sky}k_tm_{us}\Big)s^2$$
$$\cdots - \Big(bb_{sky}k_t + 2k_sk_tm_s + 2k_sk_tm_{us}\Big)s + b_{sky}k_sk_t$$

(2.19)

$$den_c = \Big(m_sm_{us})s^4 + (bm_s + b_tm_s + bm_{us} + b_{sky}m_{us}\Big)s^3 + \Big(bb_t + bb_{sky} + b_tb_{sky} + k_sm_s$$
$$\cdots + k_tm_s + k_sm_{us}\Big)s^2 + \Big(b_tk_s + b_{sky}k_s + bk_t + b_{sky}k_t\Big)s + k_sk_t$$

The controlled quarter car of Figure 2.3 is simulated using parameters of Tables 2.1 and 2.2 and is given an input of a ISO 8608 Class C road [**14**](equivalent to a moderately rough road) with vehicle traveling at 25 kph forward speed. It should be noted that the only arbitrarily selected parameters for the control are the damping coefficients of the MR (Table 2.2).

Magnitude bode plots of several responses are shown in Figure 2.4. Several items from these plots should be mentioned. First, and most important, is that the sprung mass velocity response is improved across the entire frequency band in that actuated system *without* degradation of tire

Parameter	Value
$\mathbf{m_s}$	312.5 kg
$\mathbf{m_{us}}$	52.5 kg
$\mathbf{k_s}$	20.85 kN/m
$\mathbf{b}$	2042 N m/s
$\mathbf{k_t}$	350.3 kN/m

TABLE 2.1. Parameter values for passive elements of quarter car

Parameter	Value
$\mathbf{b_t}$	4084 N m/s
$\mathbf{b_{sky}}$	6126 N m/s

TABLE 2.2. Parameters for virtual elements used for control of MIMO Sky-hook+Groundhook

velocity, a result that can only be achieved with the addition of an inertial actuator. Second, the nonlinear semi-active system, when used in conjunction with a fully active inertial force actuator, only slightly deteriorates the output response. Lastly, the region of highest human sensitivity to vertical acceleration (4-8 Hz, the frequencies between the two resonances) has been reduced in all cases. These results have motivated further study of the proposed conventional + IFA suspension configuration.

The model and control analysis thus far has depended on several unrealistic assumptions, the most egregious being that the intended inertial force F_a has been perfectly applied to the vehicle with no regard for *how*. Armed with the training provided by bond graphs' port-based approach, we assume an inertial actuator connected to the sprung mass is a simple 1-DOF oscillator in parallel with a force actuator (Figure 2.5). The bond with effort labeled F_a could be ported into Figure 2.3 to replace the effort source there labeled F_a.

The equations of motion of the system of Figure 2.5 are

$$\begin{bmatrix} \dot{q}_a \\ \dot{p}_a \end{bmatrix} = \begin{bmatrix} 0 & \frac{-1}{m_a} \\ k_a & \frac{-b_a}{m_a} \end{bmatrix} \begin{bmatrix} q_a \\ p_a \end{bmatrix} + \begin{bmatrix} 0 \\ b_a \end{bmatrix} v_s + \begin{bmatrix} 0 \\ 1 \end{bmatrix} F_c \tag{2.20}$$

where q_a is the actuator spring displacement, p_a is the actuator momentum, and F_c is the force actuator in parallel with the actuator spring, as shown in Figure 2.5.

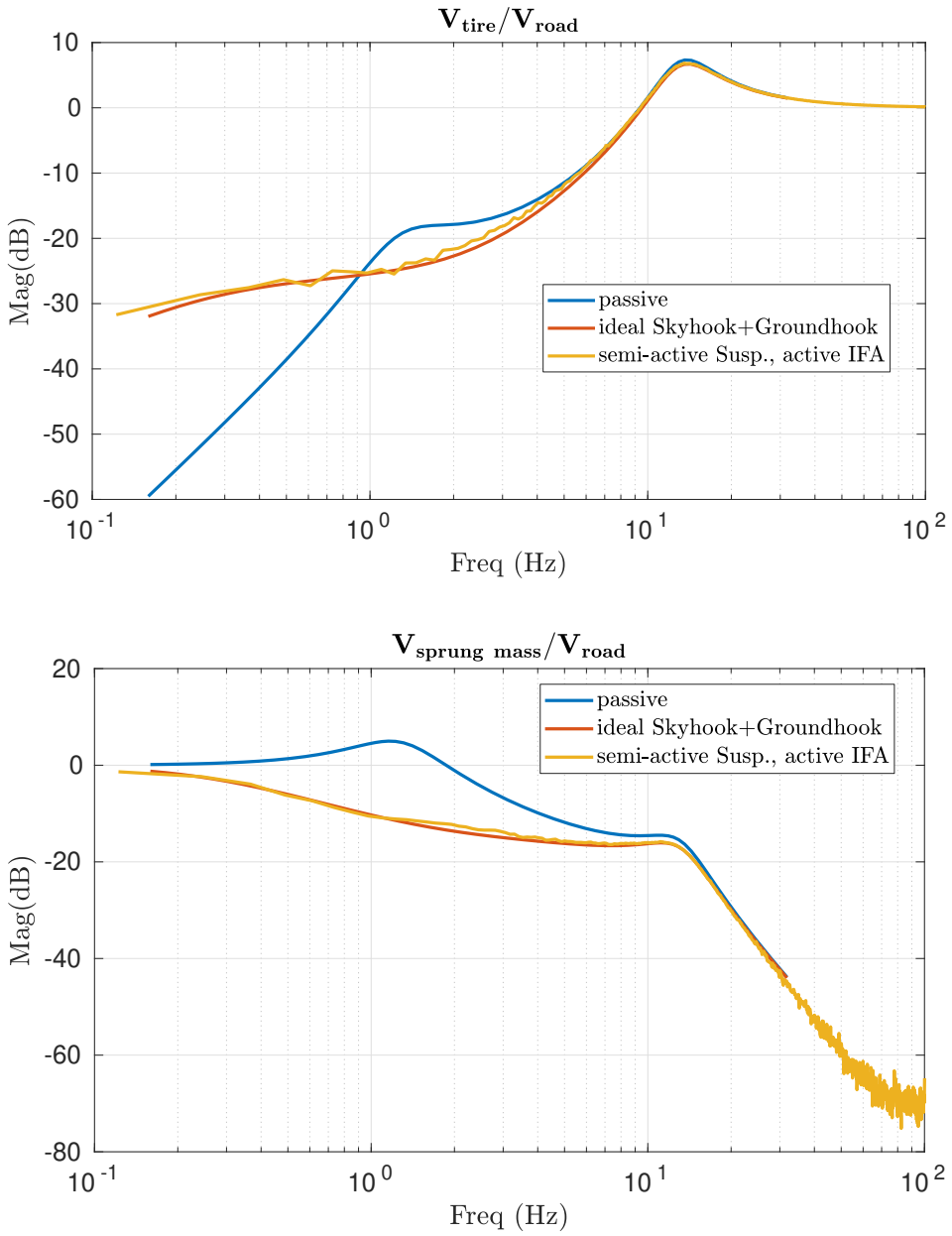

FIGURE 2.4. Frequency response plots. Passive: response to v_i road input of system of Figure 2.3 with zero forcing. Ideal: response to v_i road input of system of Figure 2.3 with control law from Equations 2.14. Semi˙active: response to v_i road input of system of Figure 2.3 with control law from Equations 2.14, but with passivity constraint on suspension actuator.

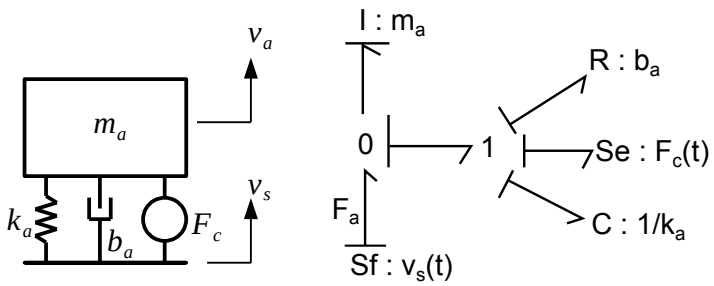

FIGURE 2.5. A model of a 1-Degree of Freedom (DoF) inertial actuator and its bond graph

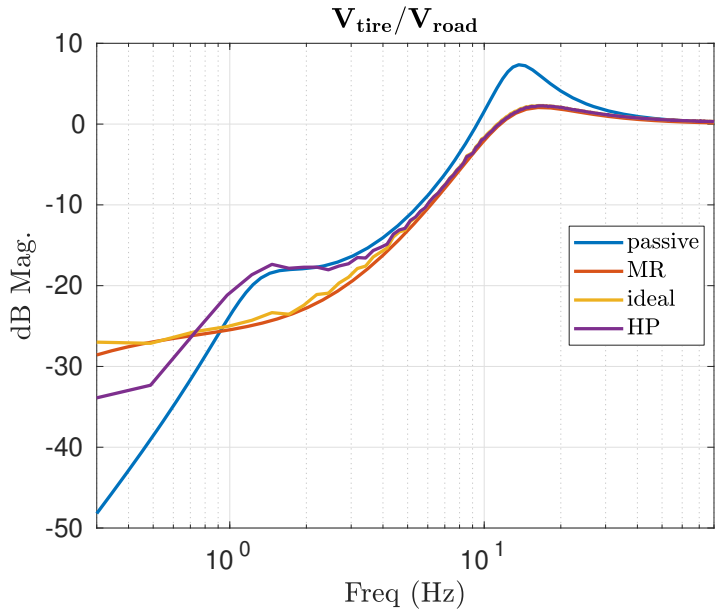

FIGURE 2.6. Tire Velocity magnitude frequency response plots (computed from Fast Fourier Transform (FFT) of simulation timeseries unless noted otherwise). Passive: passive system (Figure A.1, computed from transfer function). MR: Model reference (Figure 2.2, computed from transfer function). Ideal: Feed-forward controlled system with inertial force F_a (Figure 2.3). HP: same as Ideal, but with a high-pass filter applied to F_a.

Instead of integrating the added dynamics to re-compute the control law of Equation 2.14 for the new controlled input F_c, we derive the transfer functions from the equations of motion of the

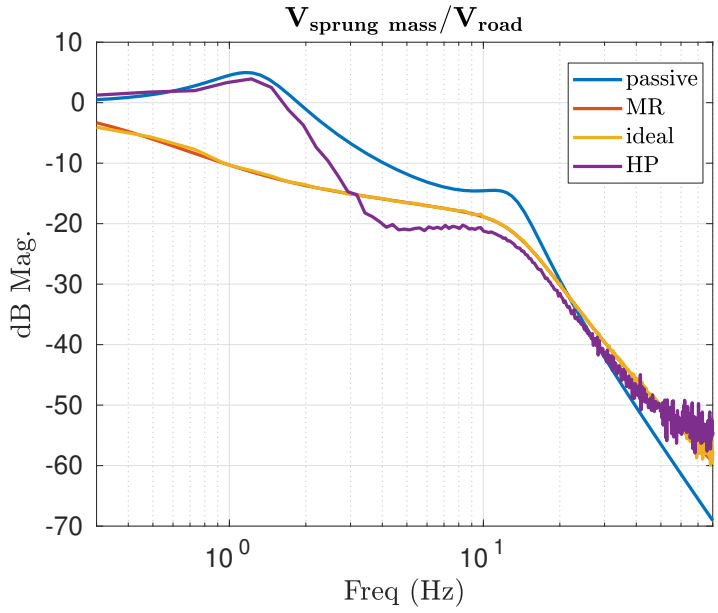

FIGURE 2.7. Sprung Velocity magnitude frequency response plots (computed from FFT of simulation timeseries unless noted otherwise). Passive: passive system (Figure A.1, computed from transfer function). MR: Model reference (Figure 2.2, computed from transfer function). Ideal: Feed-forward controlled system with inertial force F_a (Figure 2.3). HP: same as Ideal, but with a high-pass filter applied to F_a.

1-DOF, 2nd order, 2-input actuator as Equations 2.21.

$$\begin{aligned} \frac{p_a}{v_s}(s) &= \frac{b_a s + k_a}{s^2 + \frac{b_a}{m_a}s + \frac{k_a}{m_a}} \qquad \frac{p_a}{F_c}(s) = \frac{s}{s^2 + \frac{b_a}{m_a}s + \frac{k_a}{m_a}} \\ \frac{q_a}{v_s}(s) &= \frac{s}{s^2 + \frac{b_a}{m_a}s + \frac{k_a}{m_a}} \qquad \frac{q_a}{F_c}(s) = \frac{\frac{1}{m_a}}{s^2 + \frac{b_a}{m_a}s + \frac{k_a}{m_a}} \end{aligned} \tag{2.21}$$

The output, F_a, can be calculated by following causality shown in Figure 2.5. By inspection, we see that $F_a = \frac{dp_a}{dt} = sP_a(s)$. Therefore, from Equations 2.21 we can derive transfer functions for the output F_a as

$$\frac{F_a}{v_s}(s) = \frac{b_a s^2 + k_a s}{s^2 + \frac{b_a}{m_a}s + \frac{k_a}{m_a}} \qquad \frac{F_a}{F_c}(s) = \frac{s^2}{s^2 + \frac{b_a}{m_a}s + \frac{k_a}{m_a}}$$

Again applying the principle of superposition we arrive at the total actuator force F_a

$$F_a(s) = \frac{F_a}{v_s}(s)v_s(s) + \frac{F_a}{F_c}(s)F_c(s) \tag{2.22}$$

Solving Equation 2.22 for F_c,

$$F_c(s) = \left(\frac{F_a}{F_c}(s)\right)^{-1} F_a(s) - \frac{F_a}{v_s}(s)\left(\frac{F_a}{F_c}(s)\right)^{-1} v_s(s) \tag{2.23}$$

Because the transfer function $\frac{F_a}{F_c}(s)$ is proper, but not strictly proper, the direct inversion is justified. Since we already have the timeseries from the simulation for signals F_a and v_s, we can pass them through their respective 'filters' in Equation 2.23 to acquire the control signal $F_c(t)$ on the actuator of Figure 2.5 that imposes the controlled signal F_a from Equation 2.14 onto the sprung mass.

Next, we can acquire the q_a timeseries, which represents the actuator displacement for the simulation.

$$q_a = \frac{q_a}{v_s}v_s + \frac{q_a}{F_c}F_c \tag{2.24}$$

Parameters are chosen such that the simple actuator has $m_a = \frac{m_s}{100}$, natural frequency of around 1 Hz, and very little damping. Results are shown in Figure 2.8. The results show that the system and parameters are totally unrealistic for the given inputs.

As a second attempt, we could increase the spring rate to try to keep the actuator displacement near equilibrium, but this would result in F_c needing to fight the spring and damper more often. Since the results of Figure 2.8 suggest a DC component is required by the control, we try passing the controller output signal through a high-pass (HP) filter $\frac{s}{s+w_h}$ before allowing it to become a force in the actuator. We arbitrarily choose a cutoff w_h of around 2 Hz. Results are shown in Figure 2.9, and the actuator displacement has been reduced by a factor of 100. The impact of the HP filter on the tire and sprung mass dynamics can be seen in Figures 2.6 and 2.7, which show that the system with the HP filter maintains better performance compared to the passive system.

Signal Root Mean Square (RMS) results for the system simulations discussed so far are shown in Table 2.3. The results suggest that some benefit may be found in implementing an IFA with a conventional active suspended vehicle, but further adjustments to the control parameters of the

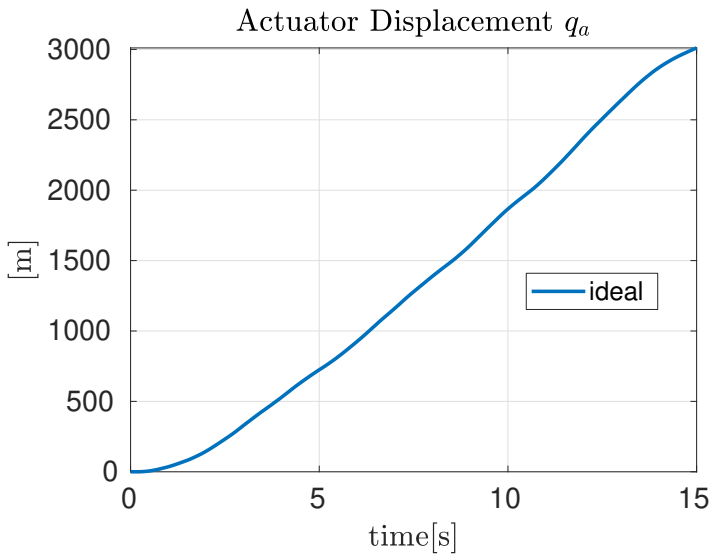

FIGURE 2.8. Actuator travel explodes to 3km in one direction, suggesting large DC component to F_a

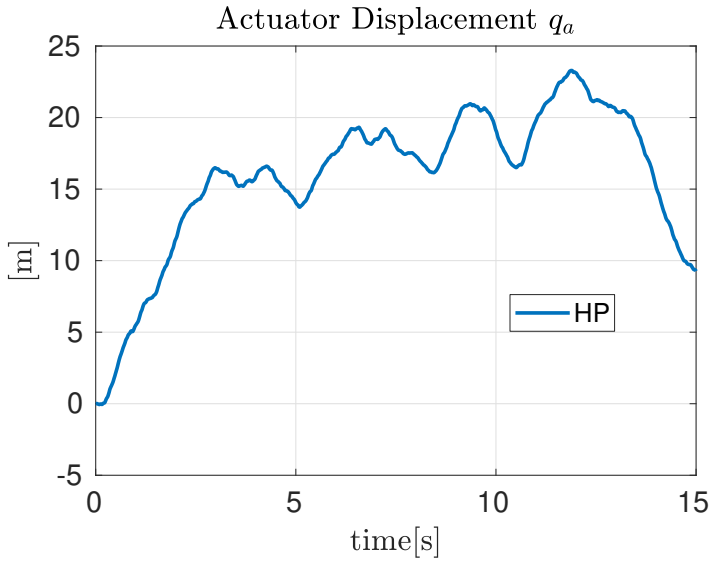

FIGURE 2.9. Actuator travel when a high-pass filter is applied to F_a

system discussed shows diminishing benefit. Therefore, a different approach is tried with optimal control.

	Passive	Ideal	HP
$\dot{\mathbf{v}}_\mathbf{s}, \frac{m}{s^2}$	1.17	0.730	0.672
$\mathbf{v_s}$, $\frac{m}{s}$	0.06262	0.0240	0.0562
$\mathbf{q_t}$,m	0.00200	0.00157	0.00154
$\mathbf{q_a}$,m		1649	16.6
$\mathbf{q_s}$,m	.00622	.00960	.00723
$\mathbf{F_a}$,N		497	452
$\mathbf{F}$,N		380	380

TABLE 2.3. Results of simulation using feedforward control (all results are RMS values)

2.2. Investigation of Optimal Control of Inertial Force Actuator

In this section, a preliminary analysis, utilizing optimal control theory, is presented. We begin by introducing a 3 degree of freedom system model (Figure 2.10). This is the same model as Figure 2.3, except a proof mass is added (with associated spring and damper) so that certain actuator-specific variables can be minimized in the optimal control.

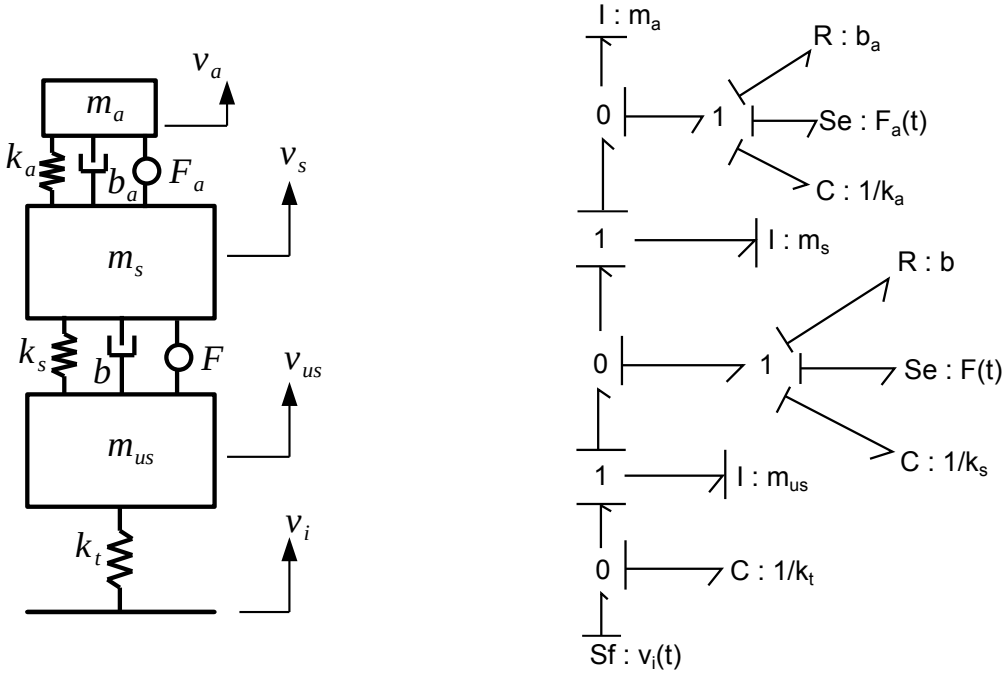

FIGURE 2.10. Model of actuated system for optimal control

From the bond graph of Figure 2.10, we derive the system equations in linear state space form (Equations 2.25).

$$
(2.25)\qquad
\begin{bmatrix} \dot{q_t} \\ \dot{q_s} \\ \dot{q_a} \\ \dot{p_{us}} \\ \dot{p_s} \\ \dot{p_a} \end{bmatrix} =
\begin{bmatrix}
0 & 0 & 0 & \frac{-1}{m_{us}} & 0 & 0 \\
0 & 0 & 0 & \frac{1}{m_{us}} & -\frac{1}{m_s} & 0 \\
0 & 0 & 0 & 0 & \frac{1}{m_s} & \frac{-1}{m_a} \\
k_t & -k_s & 0 & -\frac{b}{m_{us}} & \frac{b}{m_s} & 0 \\
0 & k_s & -k_a & \frac{b}{m_{us}} & \frac{-b_a - b}{m_s} & \frac{b_a}{m_a} \\
0 & 0 & k_a & 0 & \frac{b_a}{m_s} & \frac{-b_a}{m_a}
\end{bmatrix}
\begin{bmatrix} q_t \\ q_s \\ q_a \\ p_{us} \\ p_s \\ p_a \end{bmatrix} +
\begin{bmatrix}
1 & 0 & 0 \\
0 & 0 & 0 \\
0 & 0 & 0 \\
0 & 0 & -1 \\
0 & -1 & 1 \\
0 & 1 & 0
\end{bmatrix}
\begin{bmatrix} v_i \\ F_a \\ F \end{bmatrix}
$$

We frame the optimal control problem as an infinite horizon, continuous-time quatradic optimization, also known as a Linear Quadratic Regulator (LQR). First, a cost function is proposed,

$$
(2.26)\qquad J = \int_0^\infty \alpha_q q_a^2 + \alpha_a \dot{p_s}^2 + \alpha_t q_t^2 + \alpha_F F^2 + \alpha_{F_a} F_a^2 \;\; dt
$$

where the α_i are tuned parameters whose values are selected to provide desirable results for the system outputs (consisting of system states and state derivatives) and control force signals that we want to minimize. This cost function is converted into standard form by transforming the α_i such that they populate the Q,R, and N matrices of

$$
(2.27)\qquad J = \int_0^\infty x^T Q x + u^T R u + 2 x^T N u \;\; dt
$$

For details on populating the elements of Q, R, and N from states and state derivatives, see section SECTION. The cost function is minimized by the full-state feedback control law

$$
(2.28)\qquad u = -Kx
$$

with static gain matrix K, where $K = R^{-1}(B^T P + N^T)$ and P is found by solving the Riccati equation

$$
A^T P + PA - (PB + N)R^{-1}(B^T P + N^T) + Q = 0
$$

The vehicle passive element parameters of Table 2.1 are again used, and the model with the feedback control law of Equation 2.28 simulated over a disturbance input v_i with road elevation

profile of an ISO 8608 Class C road [**14**] with vehicle traveling at 25 kph forward speed (the same input as in Section 2.1). For comparison, a passive quarter car is simulated over the same road input. After some tuning of the α_i cost function parameters of Equation 2.26, the frequency response plots of Figure 2.11 were generated.

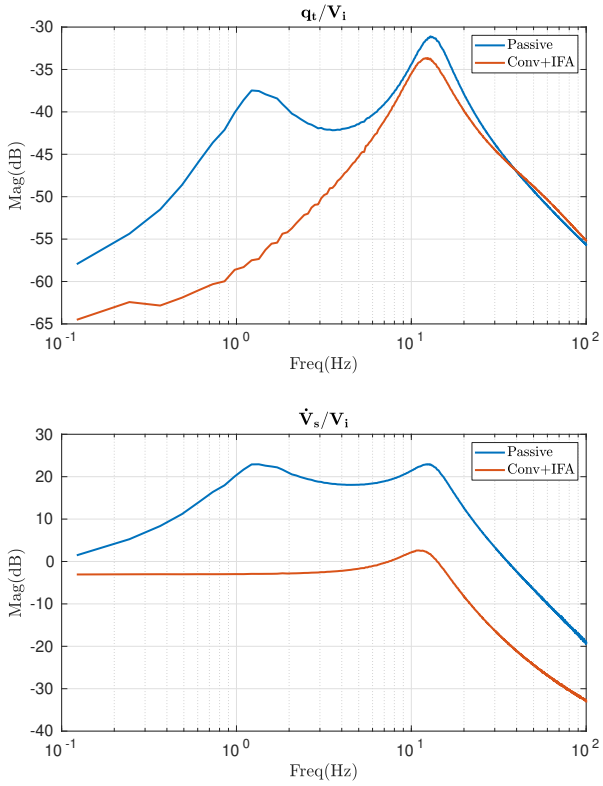

FIGURE 2.11. Magnitude frequency response plots of passive system of Figure A.1 and active system of Figure 2.10 to a ISO 8608 Class C random road input.

Figure 2.11 shows that *both* tire displacement and sprung mass acceleration are reduced across the frequency band. These results are normally mutually exclusive, exhibiting a waterbed effect on one when the other is optimized [**28**], and further suggests novelty of the proposed model as it applies to vehicle dynamics. Some results of interest in Table 2.4 are the degree to which the RMS sprung mass acceleration, RMS tire displacement, and RMS sprung mass jerk are reduced.

It should be noted from Table 2.4 that the suspension displacement RMS has increased significantly. This is an inevitable byproduct of the chosen cost (Equation 2.26), and in the limit of zero sprung mass acceleration and zero tire spring displacement (which is, according to road-holding

	$\dot{\mathbf{v}}_\mathbf{s}, \frac{m}{s^2}$	$\ddot{\mathbf{v}}_\mathbf{s}, \frac{m}{s^3}$	$\mathbf{q_t}, m$	$\mathbf{q_a}, m$	$\mathbf{q_s}, m$	$\mathbf{F_a}, N$	$\mathbf{F}, N$	$\mathbf{Power_{F_a}}, W$	$\mathbf{Power_F}, W$
Passive	0.6063	46.38	.0012	0.0081	0.0028				
Active	0.0568	4.53	.0009	0.0088	0.0120	455.07	475.4	433.91	46.30

TABLE 2.4. Results of simulation using optimal controller (all results are RMS values)

and comfort, the desired response of the system), the spring displacement has significant dynamic deflection, following the road input exactly. In this initial study, the spring displacement was omitted from the cost in order to maximize the benefits of the controlled system on the primary output signals while permitting undesireable results to other signals. This allowed for viewing of other signals' worst case outputs in the face of minimizing the primary signals. Suspension deflection is an important signal for consideration, and too much could be inadmissible. As such, the proposed research will consider such practicalities and endeavor to include design constraints into the control.

Another item to note is the total power RMS which, when compared to the power required to maintain constant velocity of an automobile (60mph is on the order of 10kW [**18**] [**20**]), seems quite large. However, *average* power is a better indicator of performance, because unlike the RMS power, average power (Equation 2.29) takes into account power flow direction if the actuator power electronics are designed to allow bi-directional power flow (regeneration). Figure 2.12 shows that the combined actuators' running average power dissipated (equivalent to the integral power load on the vehicle electrical supply over time) is extremely small: just under 3 Watts.

$$P_{avg} = \frac{1}{T}\int_0^T P(t)dt \tag{2.29}$$

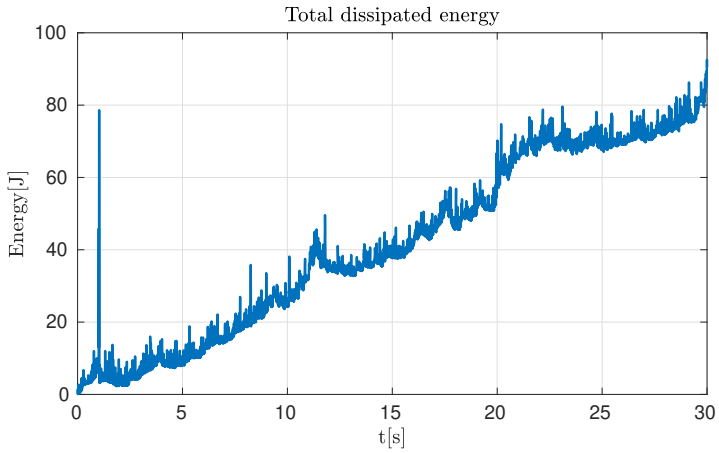

FIGURE 2.12. Integral of the sum of the instantaneous power vs time signals of the two actuators

.

CHAPTER 3

Methods

3.1. Tire Model

3.1.1. Dugoff Model. The tire model used for simulation is the Dugoff tire model [**10**]. This model captures nonlinear tire characteristics well in most operating ranges while remaining computationally tractible. Although the Dugoff tire model, in its complete form, can account for combined lateral and longitudinal loading, our current model only assumes lateral forces. This is called the free-rolling assumption, since longitudinal forces due to slip are neglected. The lateral (F_y) and longitudinal (F_x) tire forces are described by

$$F_X = \frac{C_x s}{1-s} \tag{3.1}$$

$$F_Y = \frac{C_\alpha \tan\alpha}{1-s} \tag{3.2}$$

$$z = \frac{\mu F_z}{2\sqrt{F_y^2 + F_x^2}} \tag{3.3}$$

$$f(z) = \begin{cases} z(2-z), z < 1 \\ 1, z \geq 1 \end{cases} \tag{3.4}$$

$$F_x = F_X f(z) \tag{3.5}$$

$$F_y = F_Y f(z) \tag{3.6}$$

The model input variables are F_z, the tire normal force; α, the tire slip angle; and s, the tire slip ratio. Outputs of the model are F_x and F_y, the forces applied to the tire at the contact patch. This represents a monotonic function in three variables. A snapshot of the model when $s = 0$ is shown in Figure 3.1. It should be noted that this model does not represent tire characterstics well very far into the nonlinear region, since real tires eventually saturate, whereas the Dugoff model is monotonic in all variables.

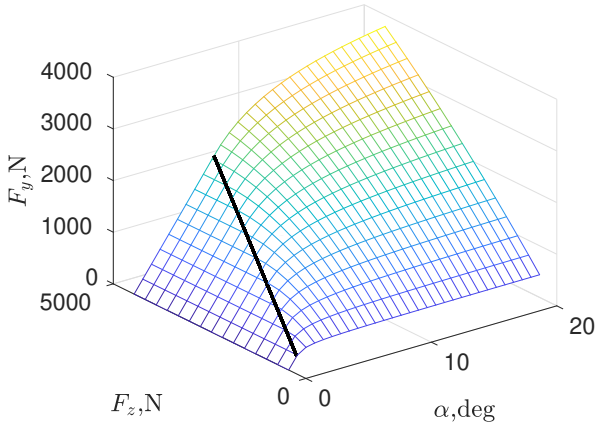

FIGURE 3.1. Dugoff Tire model, with the boundary between linear and nonlinear regions highlighted (assuming slip ratio, s, is negligible)

Figure 3.2 compares Dugoff and Magic Formula tire models, where the Magic Formula is considered to be the gold standard tire model. This shows that the Dugoff model is satisfactory for lower slip angles. Given that Magic Formula is a highly parameterized model, it is difficult to implement without access to tire test data; also, the specificity of the parameters of Magic Formula are for the saturation regions (visible in Figure 3.2), and inherently make their results less general. Since the interest is in general applicability of the control methods herein to vehicles, the Dugoff model is preferrable. This selection has the secondary benefit of reduced computation time in simulation.

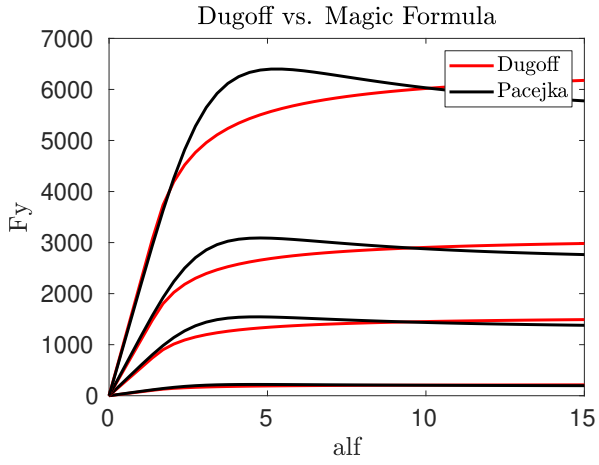

FIGURE 3.2. A comparison of Dugoff and Pacejka (Magic Formula) tire model lateral force vs slip angle for various normal loads

3.1.2. Modified Dugoff. In order to capture the physical effect of lateral force rolloff as a result of normal tire force modulation when traversing a random road, a dynamic cornering coefficient, C_α, is used [**19**]. A cubic law is assumed for $C_\alpha(F_z)$, and a linear law for $C_x(F_z)$. The results of the modification are shown in Figures 3.3 and 3.4.

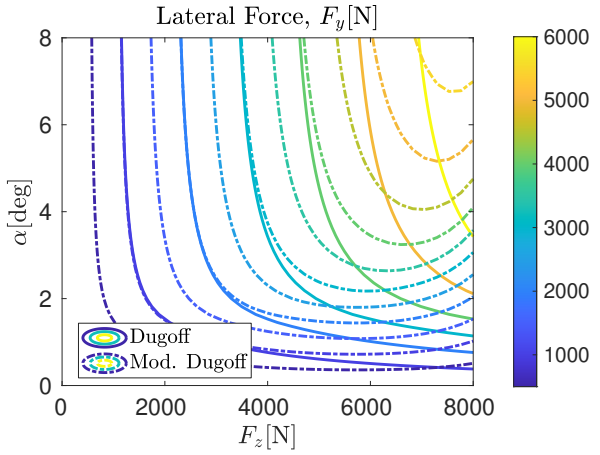

FIGURE 3.3. Dugoff Tire model with modified C_α (this plot assumes a constant forward speed and that slip ratio, s, is negligible). This is a top view of the surface plot of $F_y = f(\alpha, F_z)$.

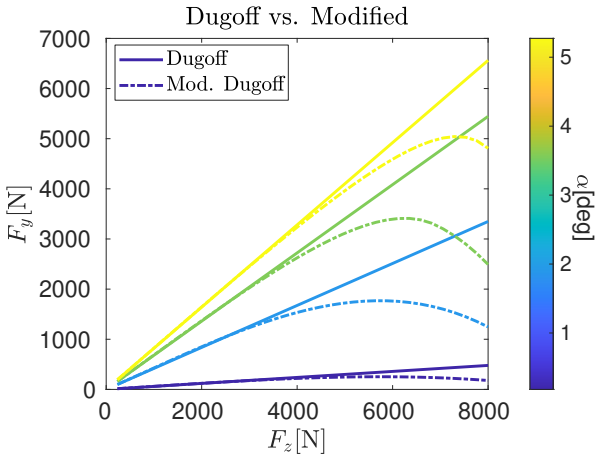

FIGURE 3.4. Dugoff Tire model modified with C_α (this plot assumes a constant forward speed and that slip ratio, s, is negligible). This is a front view of the surface plot of $F_y = f(\alpha, F_z)$.

3.2. Simulated Roadways

ISO 8608 specifies methods for characterizing roadways. These roads are placed into categories based on their elevation profile Power Spectral Density (PSD). A method for generating simulated roads is provided in [**4**] as

$$y(x) = 2^k 10^{-3} \frac{n_0}{\Delta n} \sqrt{\Delta n} \sum_{i=1}^{N} \frac{1}{i} \cos(2\pi i \Delta n x + \phi_i) \tag{3.7}$$

where

$$n_0 = 0.1$$

$$\Delta n = \frac{1}{\text{road length}, m}$$

$$N = \frac{x \text{ sampling interval}, m}{\Delta n}$$

However, since bond graph modeling will be used throughout this research, Equation 3.7 must be tranformed into a flow (velocity):

$$\frac{dy}{dx}(x) = -2^k 10^{-3} n_0 2\pi \sqrt{\Delta n} \sum_{i=1}^{N} \sin(2\pi i \Delta n + \phi_i) \tag{3.8}$$

$$\frac{dy}{dt}(t) = \frac{dx}{dt}\frac{dy}{dx} \tag{3.9}$$

$$= -2^{k+1} \pi U n_0 10^{-3} \sqrt{\Delta n} \sum_{i=1}^{N} \sin(2\pi i \Delta n + \phi_i) \tag{3.10}$$

and where k is a number from 1 to 5 corresponding with ISO8608 road class A to E, respectively, ϕ_i is a random vector that is held constant across all x locations for which a y elevation is calculated, and $U = \frac{dx}{dt}$ is forward speed, m/s. A plot of a Class B road using these equations is shown in Figure 3.5.

Figure 3.6 shows what the input to a vehicle traversing the roadway of Figure 3.5 at 40mph using Equation 3.10.

The spatial PSD of the roadway in Figure 3.5 is plotted and compared with ISO 8608 definitions of several roadway classes in Figure 3.7.

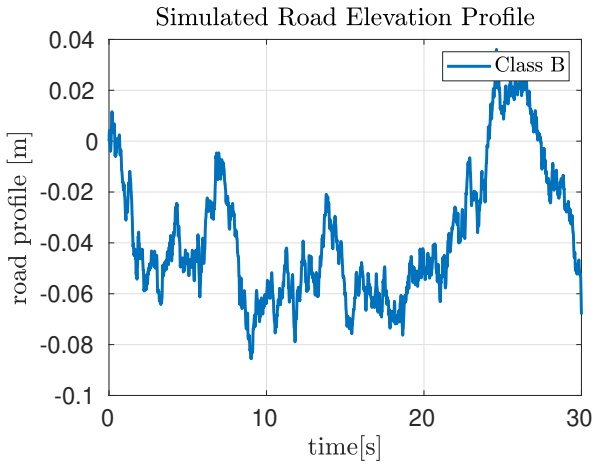

FIGURE 3.5. A characteristic simulated Class B road elevation profile. Such roads are used in subsequent simulations.

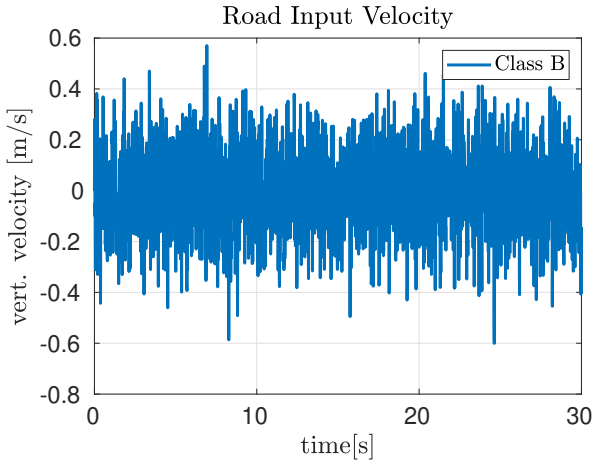

FIGURE 3.6. The tire ground input velocity profile of a car travelling on the road of Figure 3.5 at 40mph.

After generating the roadway in this manner, it is passed through a filter that is designed to attenuate undulations with wavelengths shorter than the contact patch. This is accomplished by passing the generated roadway through the spatial-domain first-order filter

$$F_{C.P.}(s) = \frac{1}{x_f s + 1} \tag{3.11}$$

where x_f is the length of the contact patch. This filter is necessary because the quarter car tire is assumed to be a point contact with the road. A more accurate model could include an averaging of

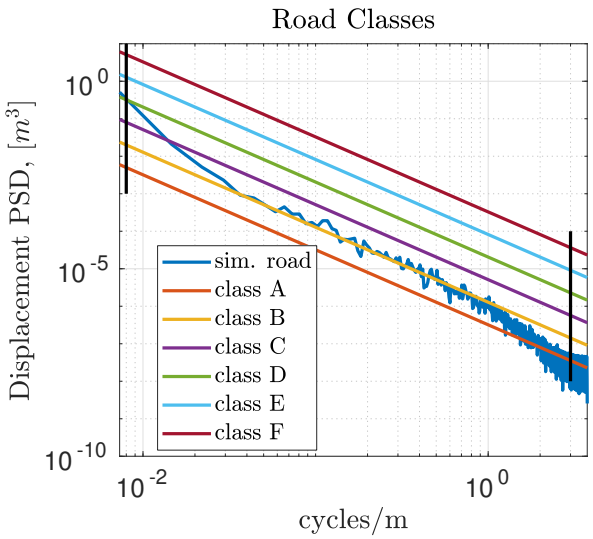

FIGURE 3.7. Spatial PSD of the roadway of Figure 3.5 simulated Class B road elevation profile. Similar simulated roads are used in subsequent simulations.

the road elevation across the contact patch during simulation, but the input pre-filter approximates this effect at a lower cost. Figure 3.8 shows the Velocity spatial PSD of the roadway of Figure 3.5, along with the same roadway but passed through the filter of Equation 3.11.

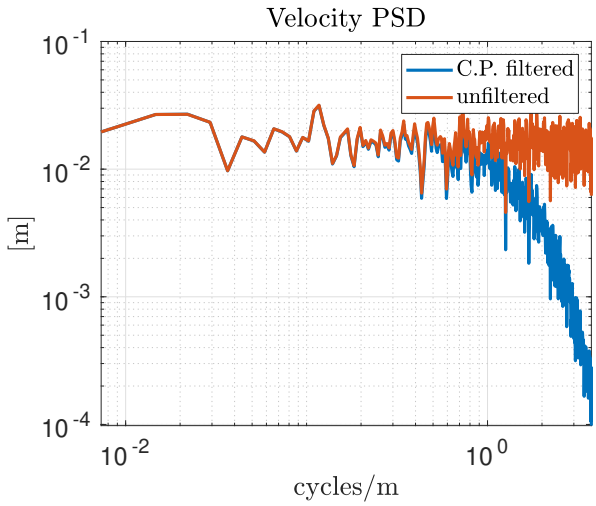

FIGURE 3.8. Spatial Velocity PSD of the roadway of Figure 3.5 simulated Class B road elevation profile. Spatial Velocity PSDs are usually flat for simulated and measured roads; however, after pre-filtering using Equation 3.11 to approximate the contact patch averaging effect, the PSD is no longer flat.

3.3. Model Predictive Control

Model Predictive Control (MPC) is a full-state feedback control method that solves an opimization problem at every control time step [**8**]. It has several benefits over classical control, including the ability to use input preview information, and to maintain state- and controlled-input constraints in the optimization; due to the the latter, it is chosen as the primary control algorithm for this research. The general form is

$$\min_{u_0,\ldots,u_{N-1}} J(X,U) \tag{3.12a}$$

$$\text{subject to } x_{k+1} = A_d x_k + B_d u_k \tag{3.12b}$$

$$x_0 = x(t) \tag{3.12c}$$

$$x_k \in \mathcal{X} \text{ for } k \in 0, 1, ..., N-1 \tag{3.12d}$$

$$u_k \in \mathcal{X}_f \tag{3.12e}$$

$$u_k \in \mathcal{U} \tag{3.12f}$$

Where $\mathcal{U}, \mathcal{X}$, and $\mathcal{X}_f$ are polyhedral sets that define the input, state, and final state constraints. The final state is defined as x_N, the state vector at the control horizon. For this research, a quadratic cost function, $J(X,U)$, is utilized.

First, the MPC equations are modified to include information from the disturbance and controlled inputs throughout the control and prediction horizon. In general, the control and prediction horizons can differ. One may wish to include an extended prediction horizon when there is high trust in the model and disturbances are small or infrequent; however, vehicle roadways, as shown in Section 3.2, provide high excitation across a wide band of frequencies. This means that the sensor preview horizon would ideally be both long, and high-resolution. This is a problem for MPC, since the high-resolution has implications for the control frequency. Fast sampling rate for MPC control implies high computational demand, and unrealistically high fidelity from a road preview sensor. Thus, in this work, a short horizon with sampling rate of 100Hz is selected. This rate corresponds with the frequency that many existing automotive networks send and receive control signals.

3.3.1. Discretizing the vehicle dynamic system model. The controller internal model is linear, and is represnted by the continuous dynamics

$$\dot{x} = Ax + Bu_c + B_w w \tag{3.13}$$

where u_c are the controlled (actuator) inputs and w are the roadway disturbance inputs. In order to represent this model in a manner that can be utilized by a digital controller, the system must be discretized to be of the form

$$x[k+1] = A_d x[k] + B_d u_c[k] + B_{dw} w[k] \tag{3.14}$$

The first choice was to use the Euler forward difference formula

$$x[k+1] = [A\Delta t - I]x[k] + B\Delta t u_c[k] + B_w \Delta t w[k] \tag{3.15}$$

However, as will be shown, this $\mathcal{O}(1)$ approximation proved too inaccurate to accurately propagate the states across the prediction horizon. In order to arrive at a more accurate representation of the continuous dynamics using equation 3.14, it is first noted that the solution of equation 3.13 is

$$x(t) = e^{A(t-t_0)}x(t_0) + \int_{t_0}^{t} e^{A(t-\tau)}(Bu_c(\tau) + B_w w(\tau))d\tau \tag{3.16}$$

If we assume that the inputs to the system are zero-order hold (piecewise-constant values from some t_0 to $t_0 + \Delta t$) then the inputs can be removed from under the integral, with the equation reduced to discrete form

$$x(t) = e^{A(t-t_0)}x(t_0) + \int_{t_0}^{t} e^{A(t-\tau)}d\tau(Bu_c + B_w w) \tag{3.17}$$

For fixed intervals, Equation 3.17 reduces to Equation 3.14, where

$$\begin{aligned} A_d &= e^{A\Delta t} \\ B_d &= \int_0^{\Delta t} e^{-A\tau}d\tau B \\ B_{dw} &= \int_0^{\Delta t} e^{-A\tau}d\tau B_w \end{aligned} \tag{3.18}$$

Lastly, since the system matrix A is invertible [**22**] then B_d and B_{dw} can be calculated using the power-series representation of the matrix exponential as

$$\begin{aligned} B_d &= [A_d - I]A^{-1}B \\ B_{dw} &= [A_d - I]A^{-1}B_w \end{aligned} \tag{3.19}$$

Since the controlled signal u_c is in actuality output by the MPC as a piecewise-constant signal, the discrete model can be quite accurate. This means that if the linear model of Equation 3.13 perfectly represents the real system, and the calculated controlled inputs are perfectly applied to the real system, the only inaccuracy of the discrete system model enters through the continuous disturbance w.

3.3.2. Preparing the Model Predictive Control. In order to transform the MPC equations for simulation using MATLAB's quadratic programming (quadprog) algorithm, several steps must first be taken. First, the equality constraints that represent the dynamics of the system are re-written to represent the discretized propagation of the states through the horizon. This is done by creating new matrices $G0_{eq}$ and $E1_{eq}$, such that the equation

$$G0_{eq}\tilde{z} = E1_{eq}\tilde{x_0} \tag{3.20}$$

where

$$\tilde{z} = [\vec{x}_1^T \quad \vec{x}_2' \cdots \vec{x}_n' \quad \vec{u}_0' \quad \vec{u}_1' \quad \cdots \quad \vec{u}_{n-1}']' \tag{3.21}$$

and

$$\tilde{x} = [\vec{x}_0' \quad \vec{w}_0' \quad \vec{w}_1' \quad \cdots \quad \vec{w}_{n-1}']' \tag{3.22}$$

This assumes a new variable $\tilde{z}$, which contains the propagation of states and the controlled inputs across the horizon, and is the optimizing variable (also known as the optimizer REF) for the MPC control. Matrix $G0_{eq}$ has the form

$$G0_{eq} = \begin{bmatrix} I & & & & -B_d & & & \\ -A_d & \ddots & & & & \ddots & & \\ & \ddots & \ddots & & & & \ddots & \\ & & & & & & & \\ & & & -A_d & I & & & -B_d \end{bmatrix} \tag{3.23}$$

Where the size of $G0_{eq}$ is $mN \times N(m+n)$

Matrix $E1_{eq}$ has the form

$$E1_{eq} = \begin{bmatrix} A_d & B_{dw} & & \\ & & \ddots & \\ & & & B_{dw} \end{bmatrix} \tag{3.24}$$

Where the size of $E1_{eq}$ is $mN \times N(m+n)$

3.3.2.1. *Cost Function Generation.* When working with MPC, we choose a cost function of the form

$$J = \int_0^\infty \alpha_q q_a^2 + \alpha_a \dot{p}_s^2 + \alpha_t \dot{q}_t^2 + \alpha_F F^2 + \alpha_V V^2 \quad dt \tag{3.25}$$

where the α_i are tuned parameters whose values are selected to provide desirable results for the system outputs (consisting of system states and state derivatives) and control force signals that we want to minimize: q_a is actuator spring displacement, which we desire to keep in a nominal position away from the limits so that the Inertial Force Actuator (IFA) is always ready to apply a desired force that minimizes the primary outputs; $\dot{p}_s$ is the derivative of sprung mass momentum, which is a primary signal we want to minimize for passenger comfort; q_t is the tire spring displacement, which is a primary signal we want to minimize for vehicle handling performance; F is the suspension actuator force; V is the IFA actuator voltage. Suspension spring displacement, q_s, is not included

in the cost function, but is permitted to make full use of its range, and if it nears its limits, will be automatically limited by the constrained optimization. This cost function is converted into quadratic matrix form by transforming the α_i such that they populate the Q,R, and N matrices of

$$J = \int_0^\infty x^T Q x + u^T R u + 2x^T N u \;\; dt \tag{3.26}$$

In order to include state derivative terms (such as vertical acceleration and tire deflection velocity) in the quadratic cost function, new quadratic cost matrices are derived below. Given that $\dot{x} = Ax + Bu_c$,

$$\dot{x}' Q_a \dot{x} = [Ax + Bu_c]' Q_a [Ax + Bu_c] \tag{3.27}$$

$$= (Ax)' Q_a Ax + (Ax)' Q_a B u_c + (Bu_c)' Q_a Ax + (Bu_c)' Q_a B u_c \tag{3.28}$$

$$= x' A' Q_a Ax + x' A' Q_a B u_c + u_c' B' Q_a Ax + u_c' B' Q_a B u_c \tag{3.29}$$

$$= x' Q_d x + 2x' N_d u_c + u_c' R_d u_c \tag{3.30}$$

where the two quantities $x' A' Q_a B u_c + u_c' B' Q_a Ax$ reduce to $2x' N_d u_c$ since both quantities in the summation result in the same scalar quantity (i.e. $x' N_d u_c = u_c' N_d' x$). This shows how costs related to state derivatives through matrix Q_a can be transformed into state- and input-cost matrices. The Q_d, N_d, and R_d matrices can be directly summed with linear quadratic matrices, arriving at the final matrix to be used in the quadratic cost.

In the case of preview control, the formulation is a bit more involved, since the measured future disturbances will impact the resultant states and controlled inputs calculated in the optimization. Given $\dot{x} = Ax + Bu_c + B_d w$,

$$\dot{x}' Q_a \dot{x} = [Ax + Bu_c + B_d w]' Q_a [Ax + Bu_c + B_d w] \tag{3.31}$$

$$\begin{aligned} &= (Ax)' Q_a Ax + (Ax)' Q_a B u_c + (Bu_c)' Q_a Ax + (Bu_c)' Q_a B u_c \\ &\quad \cdots + (Ax)' Q a B_d w + (Bu_c)' Q_a B_d w + (B_d w)' Q_a Ax + (B_d w)' Q_a B u_c \\ &\quad \cdots + (B_d w)' Q_a B_d w \end{aligned} \tag{3.32}$$

$$= x'Q_{a1}x + 2x'N_{a1}u_c + u_c'R_{a1}u_c \tag{3.33a}$$

$$\cdots + 2x'F_{a1}w + 2u'F_{a2}w \tag{3.33b}$$

$$\cdots + w'B_a'Q_aB_dw \tag{3.33c}$$

where $Q_{a1} = A'Q_aA$, $N_{a1} = A'Q_aB$, $R_{a1} = B'Q_aB$, $F_{a1} = A'Q_aB_d$, and $F_{a2} = B'Q_aB_d$. Terms in 3.33a are the quadratic costs of the state derivatives, terms 3.33b are the linear costs of the state derivative, and terms 3.33c can be omitted from the cost function since it results in a constant offset. These become part of the quadratic cost of the control horizon that is solved at each control time step through

$$\min_{\tilde{z}} J = [\tilde{z}'x_0'] \begin{bmatrix} \bar{H} & 0 \\ 0 & Q_1 \end{bmatrix} [\tilde{z}'x_0']' + F1'[\tilde{z}'x_0']' \tag{3.34}$$

where

$$Q_1 = Q + Q_{a1} \tag{3.35}$$

$$R_1 = R + R_{a1} \tag{3.36}$$

$$\bar{H}_{N(m+n)+m \times N(m+n)+m} = \begin{bmatrix} Q_1 & & & & & & \\ & \ddots & & & & & \\ & & Q_1 & & & & \\ & & & R_1 & & & \\ & & & & \ddots & & \\ & & & & & R_1 & \end{bmatrix} \tag{3.37}$$

$$F_{1,N(m+n)+m\times 1} = \begin{bmatrix} & 2A'Q_aB_d & & \\ & & \ddots & \\ & & & 2A'Q_aB_d \\ 2B'Q_aB_d & & & \\ & \ddots & & \\ & & \ddots & \\ & & & 2B'Q_aB_d \\ 2A'Q_aB_d & & & \end{bmatrix} \begin{bmatrix} w_0 \\ \vdots \\ w_{N-1} \end{bmatrix} \tag{3.38}$$

3.4. The Inertial Force Actuator Model

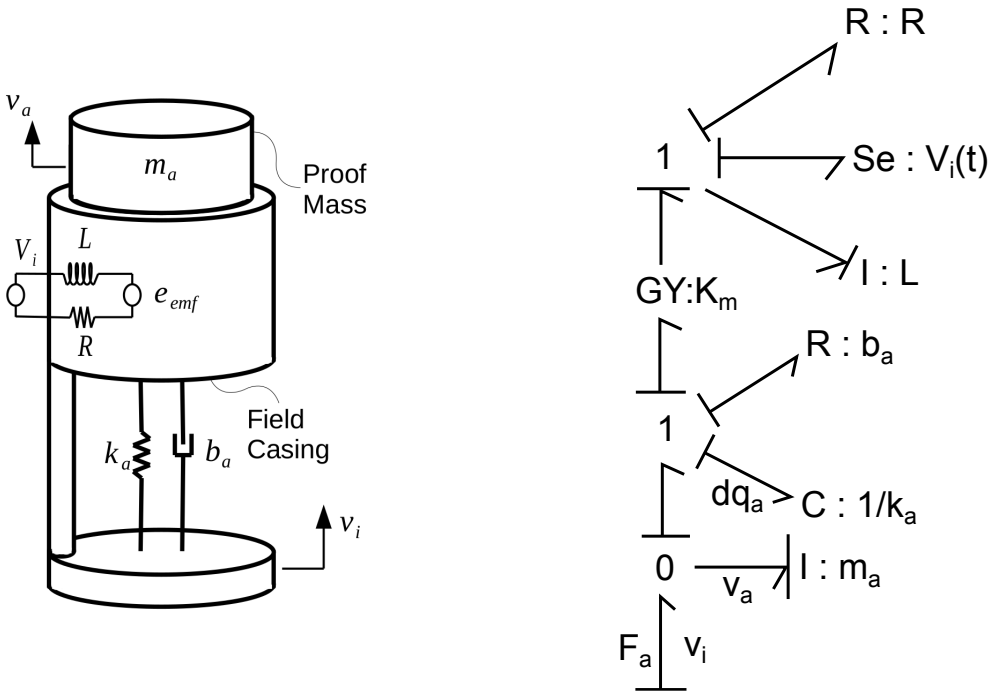

FIGURE 3.9. Model of proposed actuator

A model of the proposed inertial force actuator is shown in Figure 3.9. This is a third order model which is causal with three energy storing elements. It is comprised of a voice coil transducer, which is the translational analog of a rotational electric motor, mounted in series with a spring and damper, all of which are attached to the proof mass. The actuator is assumed to be linear (linear parameters for the system were gathered from [**1**] [**2**] [**3**]), and are of the same orders of magnitude

for max displacements and force magnitudes that preliminary simulation studies deemed necessary for the actuator. Evaluation of the bond graph produces the linear state space system of Equation 3.39.

$$\begin{bmatrix} \dot{i} \\ \dot{v_a} \\ \dot{q_a} \end{bmatrix} = \begin{bmatrix} \frac{-R}{L} & \frac{-K_e}{L} & 0 \\ \frac{K_e}{m_a} & \frac{-b_a}{m_a} & \frac{k_a}{m_a} \\ 0 & -1 & 0 \end{bmatrix} \begin{bmatrix} i \\ v_a \\ q_a \end{bmatrix} + \begin{bmatrix} \frac{1}{L} & \frac{K_e}{L} \\ 0 & \frac{b_a}{m_a} \\ 0 & 1 \end{bmatrix} \begin{bmatrix} V_i \\ v_i \end{bmatrix} \tag{3.39}$$

The transfer function from voltage input to base force excitation is given by Equation 3.40.

$$\frac{F_a}{V_i} = \frac{K_e(m_a s^2 + b_a s + k_a)}{m_a L s^3 + (b_a L + R m_a)s^2 + (K_e^2 + b_a R + k_a L)s + k_a R} \tag{3.40}$$

The inclusion of electromagnetic dynamics in the model is justified by looking at the bode plot of the full model compared to when inductance is omitted (Figure 3.10). By setting the mechanical spring and damper to zero, we get the transfer function of the fundamental electro-mechanical 2nd order gyrator, Equation 3.41.

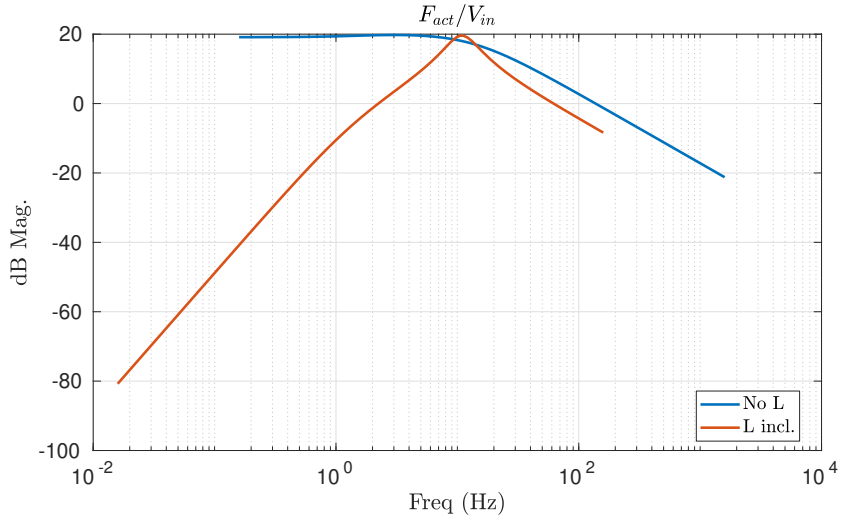

FIGURE 3.10. Frequency response plot (actuator voltage input to force output) for a model containing electrical inductance compared to one without.

$$\frac{F_a}{V_i} = \frac{\frac{K_e}{L}s}{s^2 + \frac{R}{L}s + \frac{K_e^2}{m_a L}} \tag{3.41}$$

The single transfer function zero shows that steady state tracking is not possible. This is a byproduct of Faraday's law of induction, which forms the constitutive law for the inductor of the electrical subsystem,

$$\frac{di}{dt} = \frac{V_i}{L}$$

from which we can see that for a constant input voltage, there is a constant rate increase on actuator current. This is serendipitous for our purpose, since we do not *want* the proof mass to track in the low frequency range because of the requirement that the proof mass remain nominally centered.

The transfer function of Equation 3.41 also shows the physical parameters that can be adjusted to affect the damping and natural frequency of the fundamental electro-mechanical gyrator. We see that there are 2 parameters, m_a and K_e, that can be arbitrarily placed to change the magnitude and resonant frequency. R can be increased beyond nominal values to independently increase the damping of the system, although this would negatively impact the power required to operate the controlled actuator.

The bode magnitude plot of the transfer function of Equation 3.40 for various parameter values shows that the system cannot track in the steady state. As previously mentioned, this is fine for the application of this research, since we want to reject long wavelength inputs. Another characteristic is the high gain region which evenlopes the frequency range of human sensitivity that the active suspension should endeavor to minimize.

As mentioned, the parameters were chosen from existing actuators. The proposed research will maintain this model structure and evaluate the effects of parameter selection on achieving primary control objectives (e.g. vibration isolation and/or road holding) while meeting secondary constraints (e.g. displacements and minimal power consumption).

Another benefit of this actuator, a byproduct of its high-frequency bandwidth, is that it allows for the IFA to potentially be used to suppress the high-frequency noise introduced by conventional

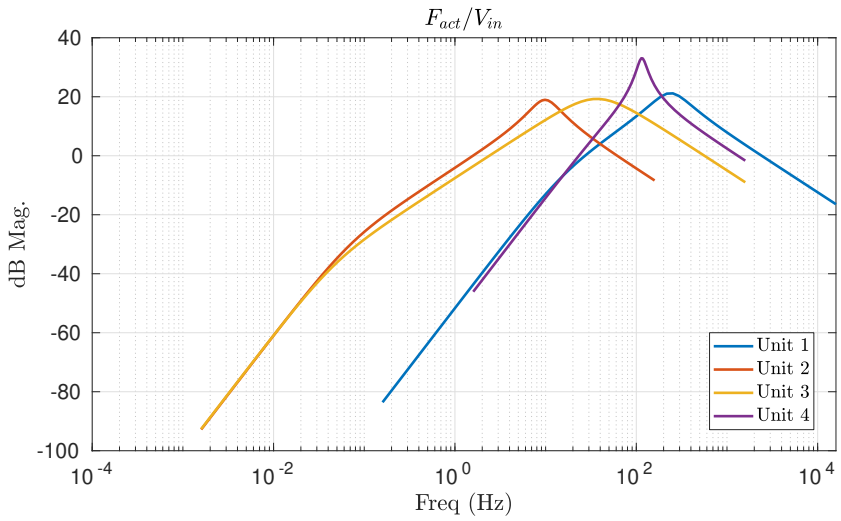

FIGURE 3.11. Frequency response plot (actuator voltage input to force output) for various off-the shelf units.

semi-active actuators. This is a prime mover for a preview control framework and analysis to be explored in the future.

3.5. High Order Vehicle Simulation Model

This section is devoted to the development of a high order vehicle simulation model. This model will be considered the "real" vehicle for validation of the actuated/controlled system. The system is modularized using Bond Graphs.

3.5.1. Sprung Mass. The sprung mass is intended to represent the chassis/cabin. It is modeled as a 6 DoF rigid body with body fixed coordinates.

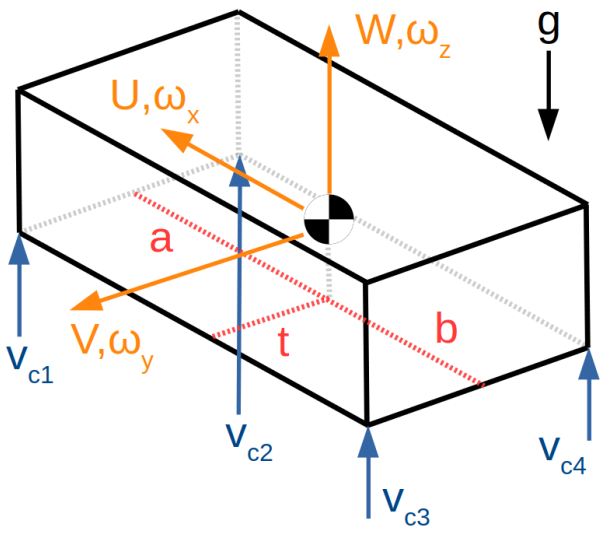

FIGURE 3.12. Diagram of sprung mass rigid body with Center of Gravity (CG), force-, and velocity-inputs located

The bond graph of the system of Figure 3.12 is represented via the bond graph fragments if Figure 3.13.

The effort sources g_x, g_y, g_z on the left (translation) bond graph represent the gravity forces after the inertial-vertical gravity vector has been rotated into the sprung mass-fixed frame (Equation 3.42, and the partial bonds are where other bond graph modules connect to the sprung mass. Note that several bonds may be represented by the single bond in some cases, since many subsystems may sum to connect at the same 1-junction. This is a simple connection since the bond graph is causal.

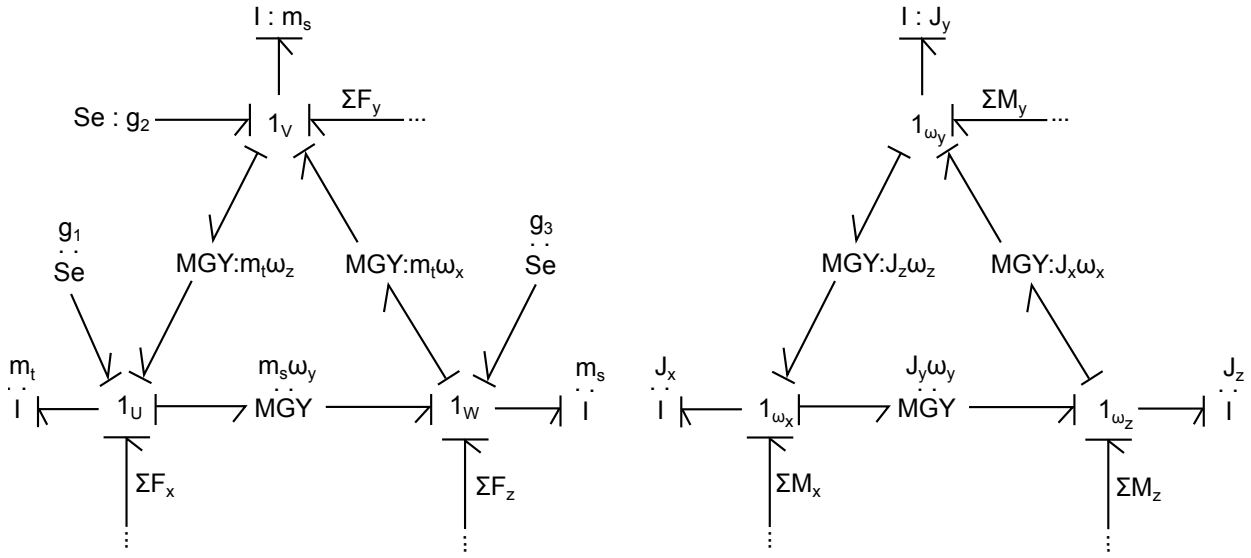

FIGURE 3.13. Bond graph fragments of sprung mass rigid body: left(translational); right(rotational).

(3.42)

$$\begin{bmatrix} g_x \\ g_y \\ g_z \end{bmatrix} = \begin{bmatrix} 1 & 0 & 0 \\ 0 & \cos\theta_x & -\sin\theta_x \\ 0 & \sin\theta_x & \cos\theta_x \end{bmatrix} \begin{bmatrix} \cos\theta_y & 0 & -\sin\theta_y \\ 0 & 1 & 0 \\ \sin\theta_y & 0 & \cos\theta_y \end{bmatrix} \begin{bmatrix} \cos\theta_z & \sin\theta_z & 0 \\ -\sin\theta_z & \cos\theta_z & 0 \\ 0 & 0 & 1 \end{bmatrix} \begin{bmatrix} 0 \\ 0 \\ -g \end{bmatrix}$$

$$= \begin{bmatrix} \cos\theta_y\cos\theta_z & \cos\theta_y\sin\theta_z & -\sin\theta_y \\ -\cos\theta_x\sin\theta_y - \cos\theta_z\sin\theta_x\sin\theta_y & \cos\theta_x\cos\theta_z - \sin\theta_x\sin\theta_y\sin\theta_z & -\cos\theta_y\sin\theta_x \\ \cos\theta_x\cos\theta_z\sin\theta_y - \sin\theta_x\sin\theta_z & \cos\theta_z\sin\theta_x + \cos\theta_x\sin\theta_y\sin\theta_z & \cos\theta_x\cos\theta_y \end{bmatrix} \begin{bmatrix} 0 \\ 0 \\ -g \end{bmatrix}$$

3.5.2. Suspensions. The suspensions are modeled as vertically-oriented. A diagram and associated bond graph for the vertical suspension dynamics are shown in Figure 3.14. The wheels, tires, brake hardware, and some suspension inertias are conveniently lumped into a single inertia called the unsprung mass. This includes all of the weight that is not statically supported by the suspension. Roadway unevenness is included as vertical velocity input at the base of each tire spring. Gravitational forces act downward on the unsprung mass. Other subsystem connections are shown in the bond graph, and include the anti sway bar and sprung mass modules.

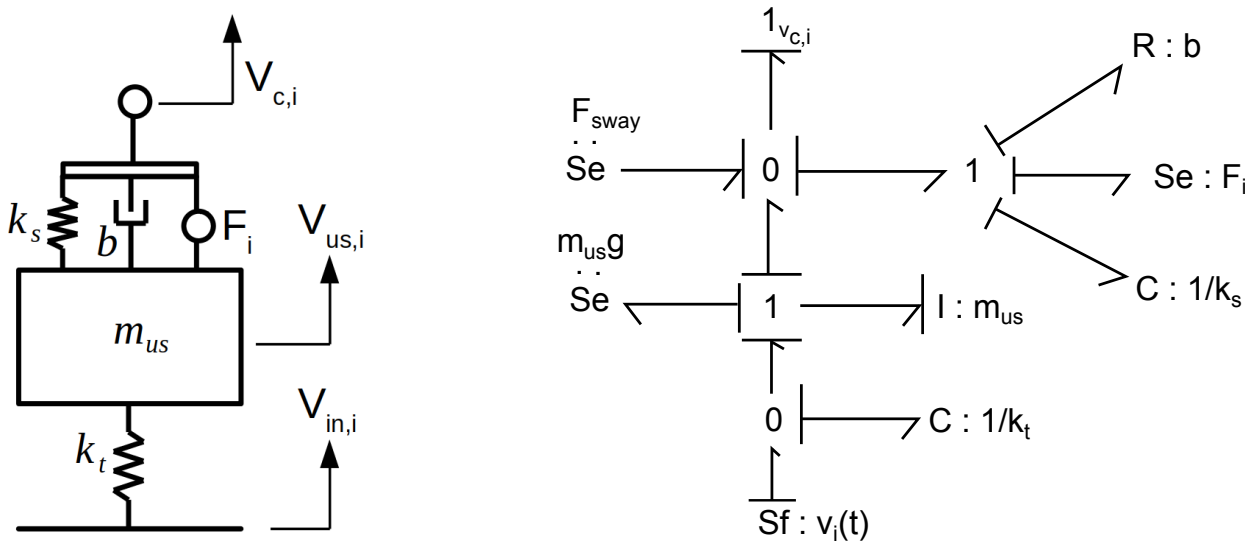

FIGURE 3.14. Vertical suspension diagram and bond graph fragment.

3.5.3. Wheel Rotational Model. The diagram and bond graph fragment for the wheel rotational inertia, J_w, is shown in Figure 3.15. The road-wheel interaction is the R-element characterizing the nonlinear friction through the tire model (Section 3.1), and the other is the torque applied to the wheels, either accelerating or braking. The high level simulation model will employ a proportional-integral controller to maintain constant forward speed applied to the front left (τ_1) and front right (τ_2) wheels.

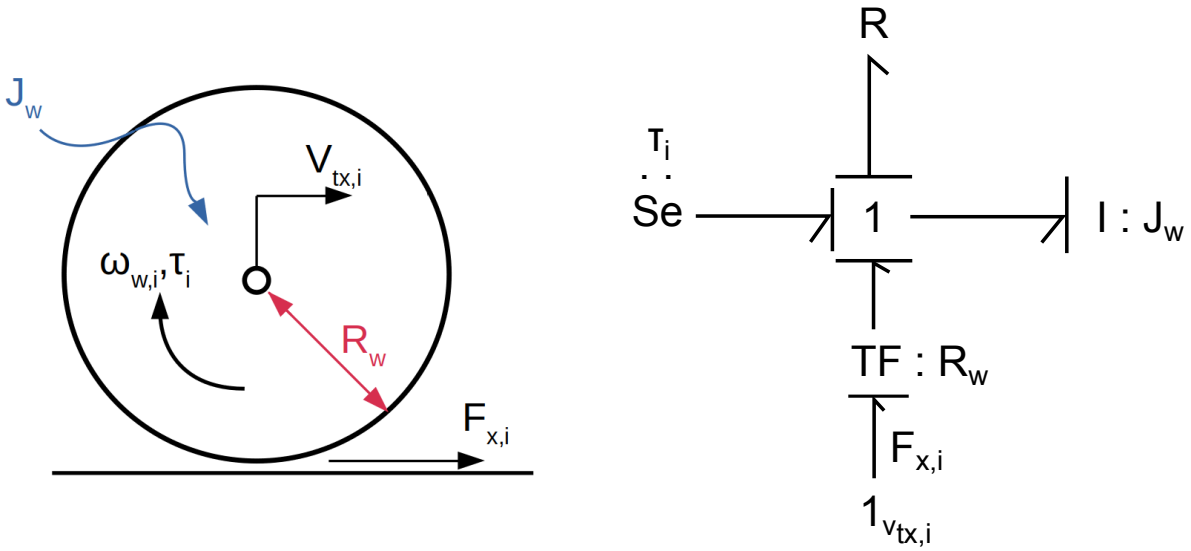

FIGURE 3.15. Schematic and Bond Graph fragment of rotating wheel.

3.5.4. Tire-Road Interaction. The tire longitudinal and lateral forces are generated through slip and slip angle [**19**]. Slip is defined as

$$s_i = \frac{|R_w \omega_{w,i} - V_{w,i}|}{\max(|R_w \omega_{w,i}|, |V_{w,i}|)} \tag{3.43}$$

Slip angle is defined as

$$\alpha_i = \delta_i - \tan^{-1} \frac{V_{ty,i}}{V_{tx,i}} \tag{3.44}$$

The tire forces are related to the slip and slip angles through a tire model, and are represented as the two poert R-element of Figure 3.16.

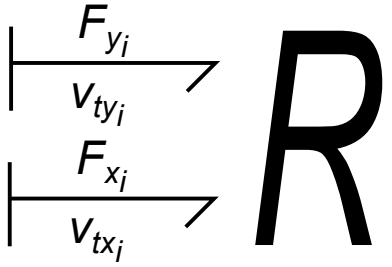

FIGURE 3.16. Bond Graph fragment of tire resistor field.

The details of the internals of the resistor fields are discussed in more detail in Section 3.1. The velocities $V_{tx,i}$,$V_{ty,i}$ are all kinematically related to state variables of the sprung mass, as shown in the bond graph fragments of Figures 3.17 and 3.18.

3.5.5. Full Set of Equations of Motion. When all of the above bond graph fragments are connected, the resulting set of dynamic equations is a 40th order nonlinear Ordinary Differential Equation (ODE). Variable descriptions are shown in Table 3.1.

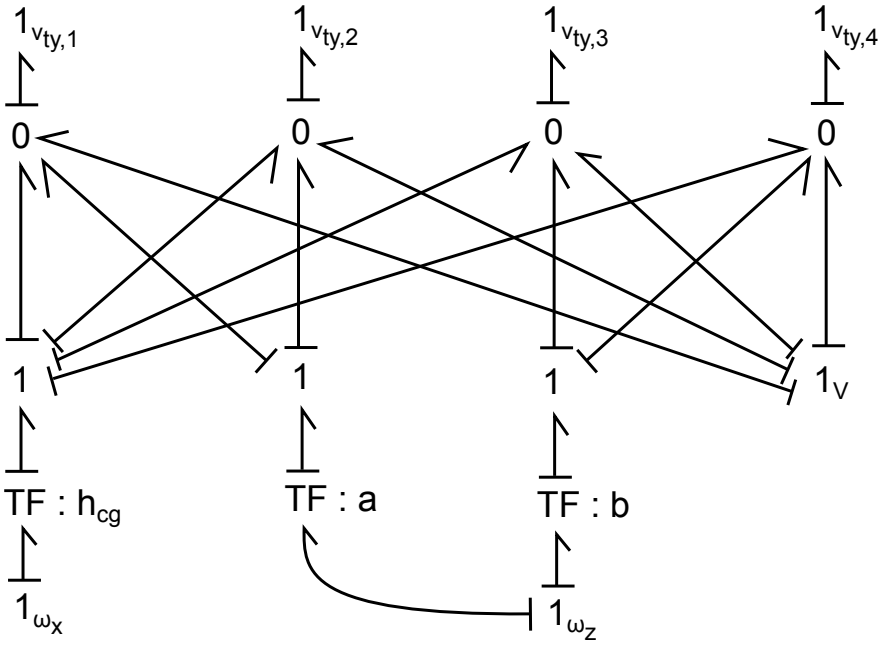

FIGURE 3.17. Bond Graph fragment of wheel center point velocities connecting to sprung mass rigid body states

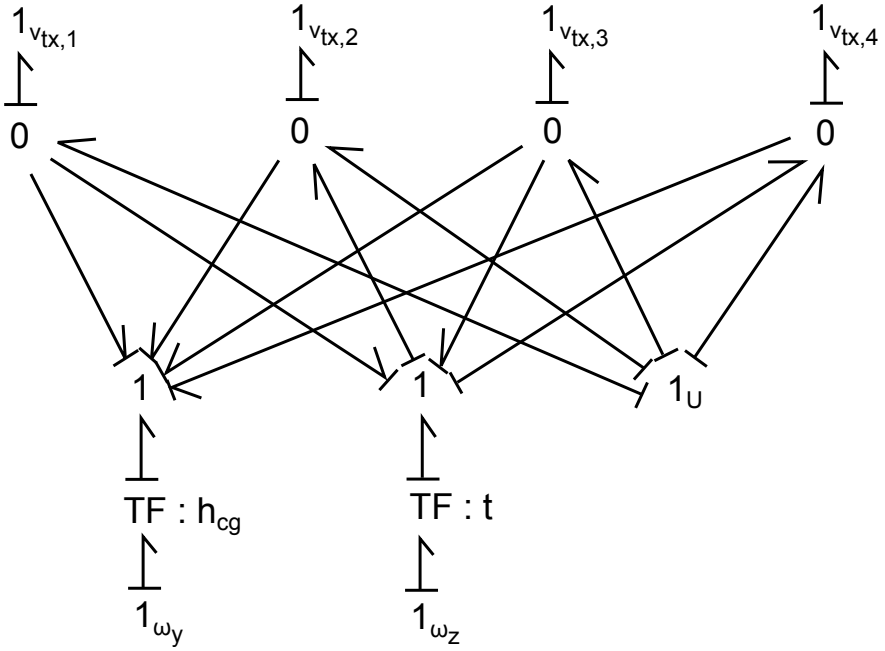

FIGURE 3.18. Bond Graph fragment of wheel center point velocities connecting to sprung mass rigid body states

Variable	Description
α_i	slip angle of tire at corner i
$F_{in,i}$	suspension force actuator input at corner i
$F_{j,i}$	generated tire force at corner i along body-fixed $j = (x, y)$
$F_{s,i}$	total suspension force at corner i
$F_{z,i}$	tire normal force at corner i
λ_i	electrical flux momentum of IFA at corner i
$p_{a,i}$	IFA vertical momentum at corner i
p_i	sprung mass momentum along body-fixed directions $(i = x, y, z)$
$p_{us,i}$	unsprung mass vertical momentum of corner i
$p_{\omega,i}$	sprung mass angular momentum along body-fixed $i = (x, y, z)$
$q_{a,i}$	IFA spring displacment at corner i
$q_{s,i}$	suspension spring displacement at corner i
$q_{t,i}$	tire spring deflection at corner i
s_i	slip ratio of tire at corner i
τ_i	wheel torque at corner i
θ_i	sprung mass angular orientation
$v_{c,i}$	suspension top mount point vertical velocity of corner i
v_i	sprung mass body-fixed velocity along direction $i = (x, y, z)$
$v_{in,i}$	road input velocity at corner i
$V_{in,i}$	IFA voltage input at corner i
$v_{us,i}$	unsprung mass vertical velocity at corner i
$v_{t,i}$	wheel velocity along body-fixed $i = (x, y)$
ω_i	sprung body-fixed angular velocity $(i = (x, y, z))$;wheel angular velocity $(i = w)$

TABLE 3.1. Definitions for variables used in equations of motion

$$\dot{\vec{q}}_t = \vec{v}_{in} - \vec{p}_{us} \tag{3.45}$$

$$\vec{v}_c = \frac{p_z}{m_s} + \begin{bmatrix} t\omega_x - a\omega_y \\ -t\omega_x - a\omega_y \\ t\omega_x + b\omega_y \\ -t\omega_x + b\omega_y \end{bmatrix} \tag{3.46}$$

$$\dot{\vec{q}}_a = \vec{v}_c - \frac{\vec{p_a}}{m_a} \tag{3.47}$$

$$\dot{\vec{q}}_s = \vec{v}_{us} - \vec{v}_c \tag{3.48}$$

$$\vec{v}_{t,x} = \frac{p_x}{m_t} - h_{cg}\omega_y + \begin{bmatrix} -t\omega_z \\ t\omega_z \\ -t\omega_z \\ t\omega_z \end{bmatrix} \tag{3.49}$$

$$\vec{v}_{t,y} = \frac{p_y}{m_t} + h_{cg}\omega_x + \begin{bmatrix} a\omega_z \\ a\omega_z \\ -b\omega_z \\ -b\omega_z \end{bmatrix} \tag{3.50}$$

$$\vec{\alpha}_{1,2} = \vec{\delta} - \tan^{-1}\frac{\vec{v}_{t,y(1,2)}}{\vec{v}_{t,x(1,2)}} \tag{3.51}$$

$$\vec{\alpha}_{3,4} = -\tan^{-1}\frac{\vec{v}_{t,y(3,4)}}{\vec{v}_{t,x(3,4)}} \tag{3.52}$$

$$\vec{s} = \frac{R_w\vec{\omega}_w - \vec{v}_{t,x}}{\max|\vec{v}_{t,x}||R_w\vec{\omega}_w|} \tag{3.53}$$

$$\vec{F}_z = \begin{Bmatrix} k_t\vec{q}_t, \vec{q}_t \geq \vec{0} \\ \vec{0}, \vec{q}_t < \vec{0} \end{Bmatrix} \tag{3.54}$$

$$\vec{F}_x = \vec{f}(\vec{\alpha}, \vec{F}_z, \vec{s}, \vec{\omega_w}, \vec{v}_{t,x}) \tag{3.55}$$

$$\vec{F}_y = \vec{f}(\vec{\alpha}, \vec{F}_z, \vec{s}, \vec{\omega_w}, \vec{v}_{t,x}) \tag{3.56}$$

$$\vec{F}_s = \vec{k}_s \cdot \vec{q}_s + \vec{b}_s \cdot \dot{\vec{q}}_s + \vec{F}_{in} + \begin{bmatrix} \frac{k_{tau,f}}{l^2}(q_{s1} - q_{s2}) \\ -\frac{k_{tau,f}}{l^2}(q_{s1} - q_{s2}) \\ \frac{k_{tau,f}}{l^2}(q_{s3} - q_{s4}) \\ -\frac{k_{tau,f}}{l^2}(q_{s3} - q_{s4}) \end{bmatrix} \tag{3.57}$$

$$\vec{F}_a = k_a \cdot \vec{q}_a + b_a \cdot \dot{\vec{q}}_a + \frac{K_e}{L}\vec{\lambda} \tag{3.58}$$

$$\dot{p}_x = \sum_{i=1}^{4} F_{x,i} + m_t(\omega_z v_y - \omega_y v_z) + m_s g \sin\theta_y \tag{3.59}$$

$$\dot{p}_y = \sum_{i=1}^{4} F_{y,i} + m_t(\omega_x v_z - \omega_z v_x) + m_s g \cos\theta_y \sin\theta_x \tag{3.60}$$

$$\dot{p}_z = \sum_{i=1}^{4} F_{s,i} + \sum_{i=1}^{4} F_{a,i} + m_s(\omega_y v_x - \omega_x v_y) + m_s g \cos\theta_x \cos\theta_y \tag{3.61}$$

$$\dot{p}_{\omega,x} = (J_y - J_z)\omega_y\omega_z + t\sum_{i=1}^{4}\left(-1^i(F_{a,i} - F_{s,i}) + h_{cg}F_{y,i}\right) \tag{3.62}$$

$$\dot{p}_{\omega,y} = (J_z - J_x)\omega_x\omega_z + h_{cg}\sum_{i=1}^{4}(F_{x,i}) + a\sum_{i=1}^{2}(F_{a,i} - F_{s,i}) + b\sum_{i=3}^{4}(F_{s,i} - F_{a,i}) \tag{3.63}$$

$$\dot{p}_{\omega,z} = (J_x - J_y)\omega_x\omega_y + \sum_{i=1}^{2}(aF_{y,i} - tF_{x,2i-1}) + \sum_{i=3}^{4}\left(-bF_{y,i} + tF_{x,2(i-2)}\right) \tag{3.64}$$

$$\dot{\vec{p}}_{us,z} = m_{us}g + \vec{F}_z - \vec{F}_s \tag{3.65}$$

$$\dot{\vec{p}}_{\omega,w} = \vec{\tau}_i - R_w\vec{F}_x \tag{3.66}$$

$$\dot{\vec{p}}_a = \vec{F}_a - m_a g \tag{3.67}$$

$$\dot{\vec{\lambda}} = \vec{V}_{in} - \frac{R}{L}\vec{\lambda} + K_e\dot{\vec{q}}_a \tag{3.68}$$

$$\dot{\vec{\theta}} = \vec{\omega} \tag{3.69}$$

.

CHAPTER 4

Simulation Study With the Quarter Car Model

4.1. Determination of Appropriate Horizon

The model prediction and preview sensoring takes place over a specified horizon. In the discretized control, this parameter sets the horizon through

$$t_n = N\Delta t \tag{4.1}$$

where t_n is the prediction horizon, Δt is the discrete control time step, and N is the number of control time steps into the future that should be included in the horizon. For this study, Δt and N are fixed. In order to choose appropriate values, multiple things are taken into consideration. First, Δt is chosen to be something reasonable and practically implementable. A sample rate of100Hz is commonly used for controllers and sensors in vehicle systems, thus we will choose the prescribed value of $\Delta t = 0.01$s and perturb slightly around this value for comparisons. N also has its selection limited by hardware. The size of the quadratic cost matrix scales with N^2, and the algorithm time complexity will scale accordingly. Therefore it is best to keep N as small as possible.

An initial approach was to choose N such that the lowest frequency dynamics are included in the control horizon. This would mean that the model prediction would witness one full wavelength of propogation of the unforced system. This would lead to a selection of N based on the following equation

$$\Delta t N = \lambda_L \tag{4.2}$$

where λ_L is the wavelength of the lowest frequency dynamics of the dynamic system. This value could be determined from the eigenvalues of the linearized system matrix, A.

The lowest frequencies of our system are designed to be about 1Hz. Therefore, by the method discussed, N should be selected to be 100. However, through simulation, it was determined that

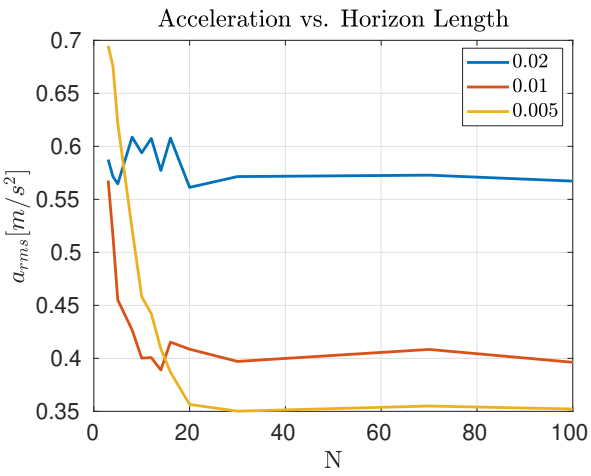

FIGURE 4.1. Plot of vehicle RMS acceleration vs N for a suite of simulations. Each simulation was run for 60 seconds over a Class B road at 40mph.

such a control horizon is intractable for solving in a reasonable time. Therefore, an experimental procedure was selected.

In this section, we present an experimental procedure for selecting the smallest value of N that produces desireable results. Although the results of this procedure may depend on many factors including control weightings, disturbance input amplitudes, and system state trajectories, we will extrapolate the results from this section and apply them to all future simulations.

Figures 4.1 and 4.2 show the Root Mean Square (RMS) vertical sprung mass acceleration and RMS tire deflection (the primary signals we are seeking to minimize) as a function of prediction horizon. Plots are shown for $\Delta t = 0.02s$, $\Delta t = 0.01s$, and $\Delta t = 0.005s$. Although $\Delta t = 0.01s$ is used exclusively in the rest of this research, the behavior of adjacent time steps is insightful for relative performance gains or losses. Interestingly, these plots show that results for $\Delta t = 0.02s$ show no discernible change as N varies. Figure 4.1 shows that sprung mass acceleration does not show performance gains above $N = 10$ for $\Delta t = 0.01s$, while Figure 4.2 shows that tire deflection performs similarly.

Secondary signals that we want to remain small are shown in Figures 4.3, 4.4 and 4.5. Figure 4.3 shows that the suspension excursion increases with increased horizon up to a point, then decreases again for large N; Figure 4.5 shows similar results for active system power. Inertial Force Actuator

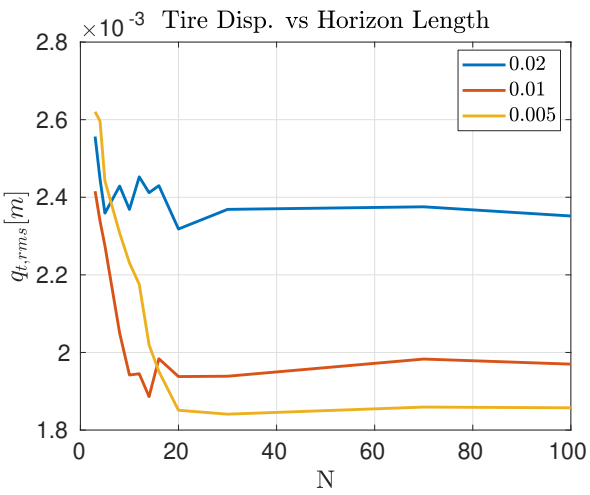

FIGURE 4.2. Plot of vehicle RMS tire displacement vs N for a suite of simulations. Each simulation ran for 60 seconds over a Class B road at 40mph.

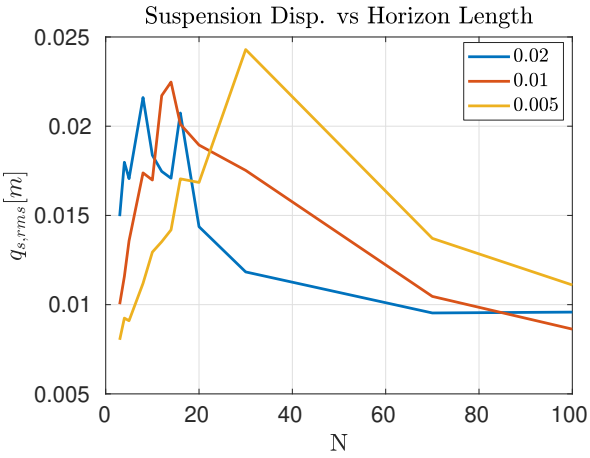

FIGURE 4.3. Plot of vehicle RMS suspension displacement vs N for a suite of simulations. Each simulation was run for 60 seconds over a Class B road at 40mph.

(IFA) deflection shows significant benefit above very small values of N, then no benefit beyond $t_n = 0.1s$.

Using these simulations as a guide, $N = 10$ is selected for all subsequent studies. It is worth noting that simulations using $N = 10$ and $\Delta t = 0.01s$ complete faster than real-time on a 10 year old and relatively unremarkable desktop computer.

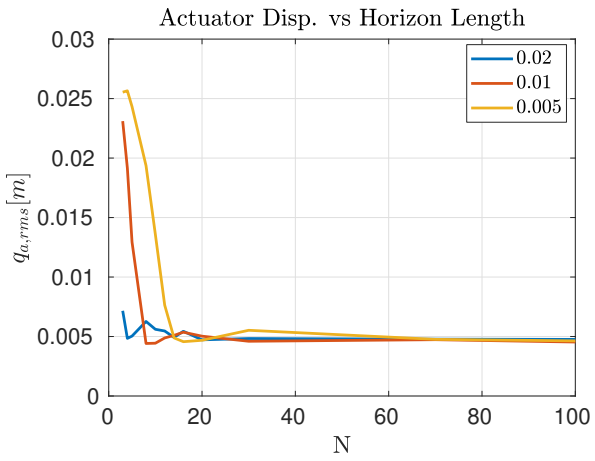

FIGURE 4.4. Plot of vehicle RMS IFA Displacement vs N for a suite of simulations. Each simulation was run for 60 seconds over a Class B road at 40mph.

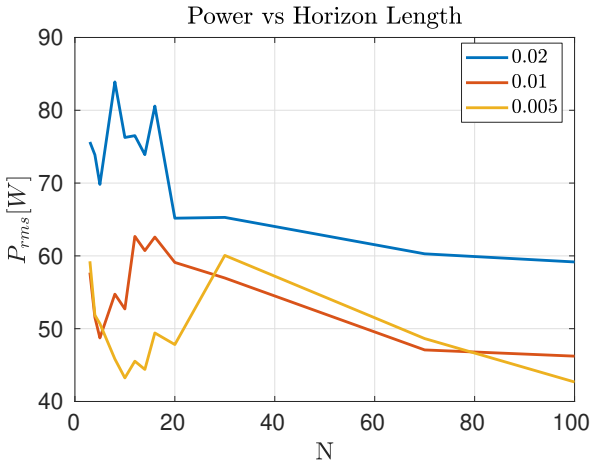

FIGURE 4.5. Plot of vehicle RMS Power vs N for a suite of simulations. The power represents the total controlled-output power calculated at each time step. Each simulation was run for 60 seconds over a Class B road at 40mph.

4.2. Quarter Car With Fully Active Suspension Actuator

Referring to Equation 3.25, the simulation parameters for results shown in this section are

$$\alpha_q = 0 \tag{4.3}$$

$$\alpha_a = \begin{bmatrix} 5 & 5e-1 & 1e0 & 5e0 & 1e1 & 2e1 & 3e1 \end{bmatrix} \tag{4.4}$$

$$\alpha_t = \begin{bmatrix} 5e6 & 1e7 & 4e7 & 7e7 & 1e8 & 3e8 \end{bmatrix} \tag{4.5}$$

(4.6) $$\alpha_F = 4e-3$$

(4.7) $$\alpha_V = 3e-2$$

These parameters were chosen to show system output sensitivity in their viscinity. The vehicle is travelling on a Class B road at 40mph. In the MPC, the IFA is constrained to +/- 3cm and the suspension displacment is constrained to +/- 8cm. Suspension force is constrained to +/- 1500N and IFA voltage is constrained to +/- 800 V.

4.2.1. Varying α_a (weighting on the sprung mass acceleration). Below are simulation results for various selections of α_a while $\alpha_t = 1e8$. In all simulations in this section, the RMS tire deflection and RMS sprung mass acceleration are less than the passive system.

Figure 4.6 shows that the sprung mass acceleration has been reduced at the ride frequency and in the human-sensitive frequency ranges. Figure 4.7 shows the tire deflection Fast Fourier Transform (FFT), which shows that the tire deflection is reduced at resonant frequencies. Figures A.4 and A.5 show that the MPC is properly maintaining the specific hard constraints and, in the context of other plots, validates the controlled system as being effective at managing primary and secondary objectives.

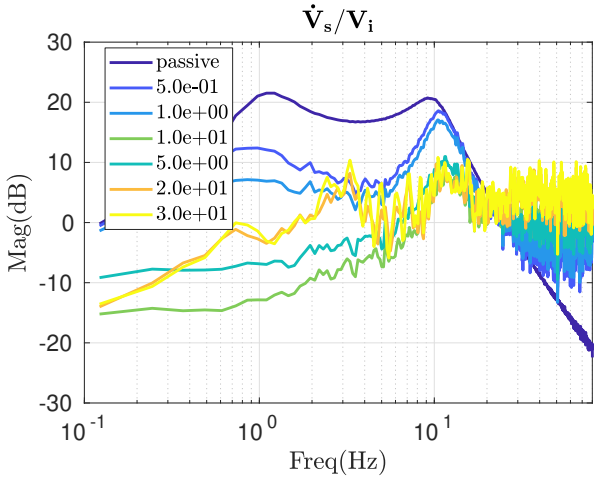

FIGURE 4.6. Plot of Sprung Mass Vertical Acceleration FFT vs Frequency with varying α_a weighting parameter.

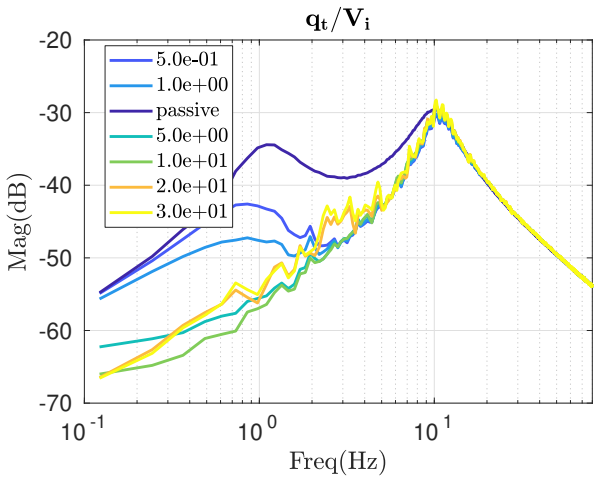

FIGURE 4.7. Plot of Tire Deflection FFT vs Frequency with varying α_a weighting parameter.

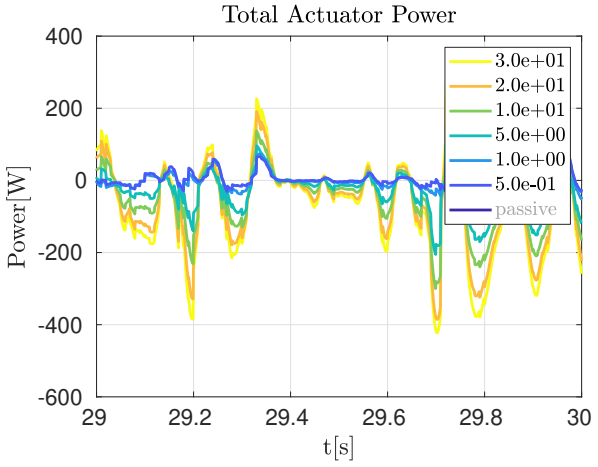

FIGURE 4.8. Plot of Total Power vs Time with varying α_a weighting parameter. Total power is the instantaneous sum of power to the IFA and the suspension actuator.

Other important results include the power required to operate the actuated system. Below are several power and energy plots that give insight to the system's feasibility. Figure 4.8 shows that penalizing acceleration higher results in increased power demand; however, the peaks are within the limits of the off-the-shelf IFA parameters chosen for simulation. Plots of the actuator forces are also shown below, and are reasonable.

Another way to look at the power is by looking at the total energy, defined as

$$E_{total} = \int_0^{t_{end}} P_{ifa}(t) + P_{susp}(t)dt \tag{4.8}$$

This integrates the instantaneous bidirectional sum of power going into and out of the two actuators. This value gives insight into the energy demands on a battery electric system. Figure 4.9 shows that for some configurations, energy can theoretically be continuously supplied to the battery from the road even while reducing both tire deflection and sprung mass acceleration. Also, taking the last data point of this plot as a reference, it says that, in the case with the highest penalization of α_a, while the total combined actuator power RMS is 134W, the supply-side power demand is only around 30W. The former represents bi-directional power flowing through the actuators and should be used for actuator specification, while the latter indicates impact on range of an electric vehicle.

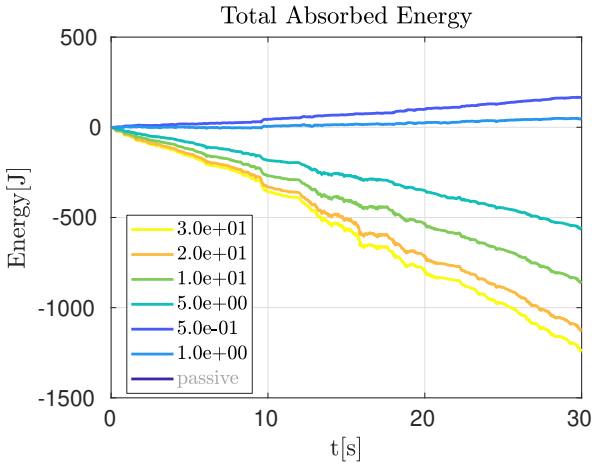

FIGURE 4.9. Plot of Absorbed Energy vs Time with varying α_a weighting parameter.

4.2.2. Varying α_t (weighting on the tire deflection). Below are simulations results for various selections of α_t while $\alpha_a = 10$. In all simulations in this section, the RMS tire deflection and RMS sprung mass acceleration are less than the passive system.

Figure A.8 shows that the sprung mass acceleration has been reduced at the ride frequency and at in the human-sensitive frequency ranges. Figure 4.11 shows the tire deflection FFT, which shows that the tire deflection is reduced at resonant frequencies. Figures A.10 and A.11 show that

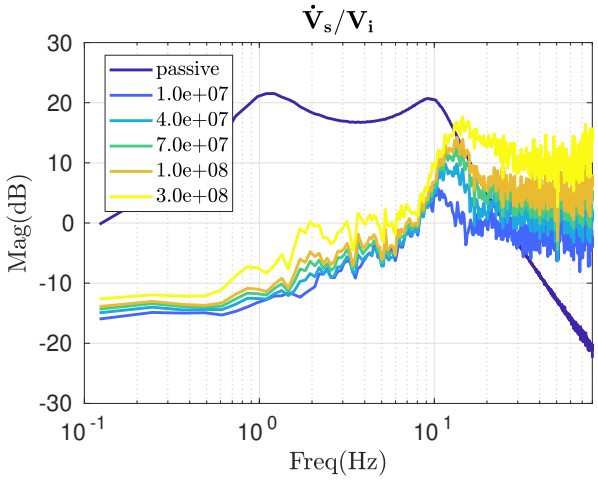

FIGURE 4.10. Plot of Sprung Mass Acceleration FFT vs Frequency with varying α_t weighting parameter.

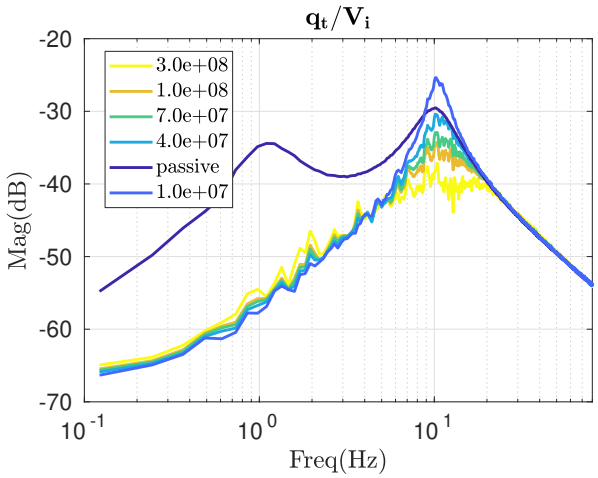

FIGURE 4.11. Plot of Tire Deflection FFT vs Frequency with varying α_t weighting parameter.

the MPC is properly maintaining the specific hard constraints and, in the context of other plots, validates the controlled system as being effective at managing primary and secondary objectives.

Other important results include the power required to operate the actuated system. Below are several power and energy plots that give insight to the system's feasibility. Figure 4.12 shows that penalizing tire deflection results in increased power demand; however, the peaks are within the

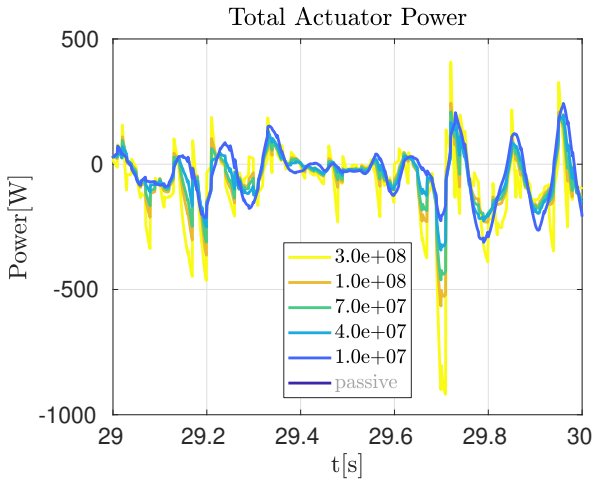

FIGURE 4.12. Plot of Total Power vs Time with varying α_t weighting parameter.

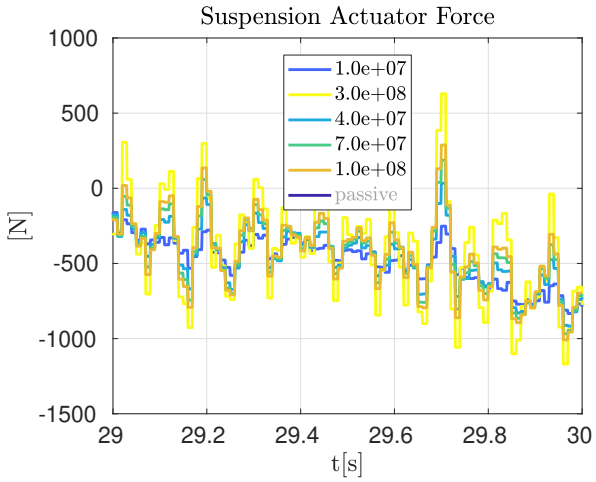

FIGURE 4.13. Plot of Suspension Actuator Force vs Time with varying α_t weighting parameter.

limits of the off-the-shelf IFA parameters chosen for simulation. Plots of the actuator forces are also shown in Figure 4.14, and are reasonable.

Again using Equation 4.8, Figure 4.15 shows the energy demand on the battery over time. Using the last data point of this plot as a reference, in the case with the highest penalization of α_t, while the total combined actuator power RMS is 184W, the supply-side power demand is only around 76W.

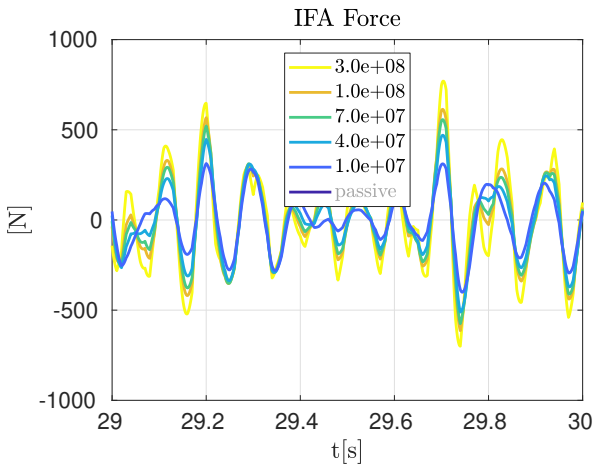

FIGURE 4.14. Plot of IFA Force vs Time with varying α_t weighting parameter.

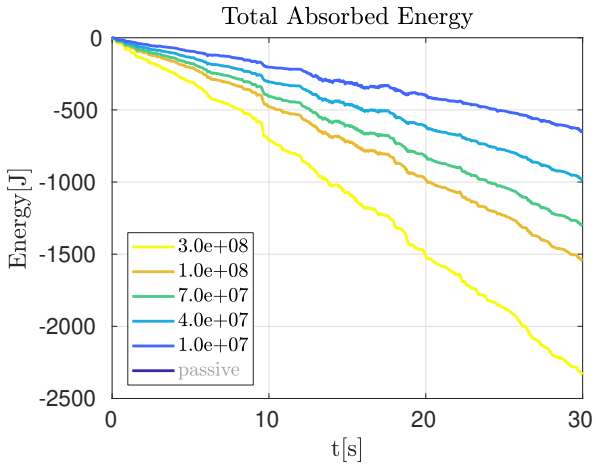

FIGURE 4.15. Plot of Absorbed Energy vs Time with varying α_t weighting parameter.

4.3. Quarter Car With Semi-Active Suspension Actuator

Referring to Equation 3.25, the simulation parameters for results shown in this section are

$$\alpha_q = 0 \tag{4.9}$$

$$\alpha_a = \begin{bmatrix} 5 & 5e-1 & 5e0 & 1e1 \end{bmatrix} \tag{4.10}$$

$$\alpha_t = \begin{bmatrix} 5e6 & 1e5 & 1e6 & 1e7 & 1e8 & 3e8 \end{bmatrix} \tag{4.11}$$

$$\alpha_F = 4e-3 \tag{4.12}$$

(4.13) $$\alpha_V = 3e - 2$$

These parameters were chosen to show system output sensitivity in their viscinity. The vehicle is again travelling on a Class B road at 40mph. In the MPC, the IFA is constrained to +/- 3cm and the suspension displacment is constrained to +/- 8cm. Suspension force is constrained to +/- 1500N and IFA voltage is constrained to +/- 800 V. Additionally, the suspension actuator is in a semi-active (clipped-optimal) constraint configuration such that it is a strictly dissipative device. Semi-active is sub-optimal since it enforces the clipped-optimal constraint [**25**].

4.3.1. Varying α_a (weighting on the sprung mass acceleration). Below are simulation results for various selections of α_a while $\alpha_t = 1e8$. In all simulations in this section, the RMS tire deflection and RMS sprung mass acceleration are less than the passive system.

Figure 4.16 shows that the sprung mass acceleration has been reduced at the ride frequency and in the human-sensitive frequency ranges. Figure 4.17 shows the tire deflection FFT. The tire deflection is reduced at resonant frequencies. Figures A.15 and A.14 show that the MPC is properly maintaining the specific hard constraints and, in the context of other plots, validates the controlled system as being effective at managing primary and secondary objectives. Figure 4.18 shows that the suspension actuator force goes to zero when the passivity condition can't be achieved.

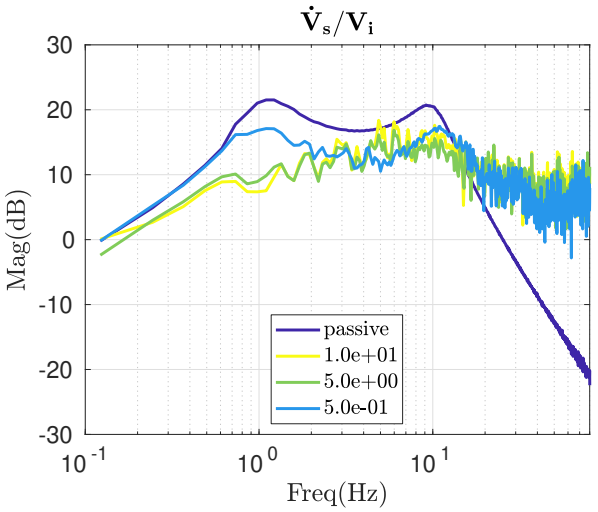

FIGURE 4.16. Plot of Sprung Mass Acceleration FFT vs Frequency with varying α_a weighting parameter.

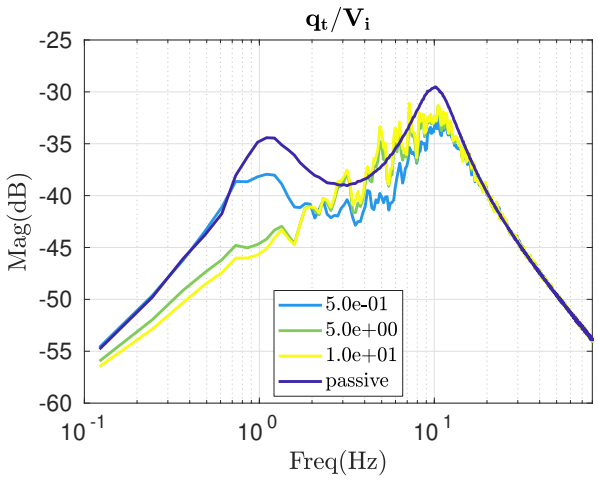

FIGURE 4.17. Plot of Tire Deflection FFT vs Frequency with varying α_a weighting parameter.

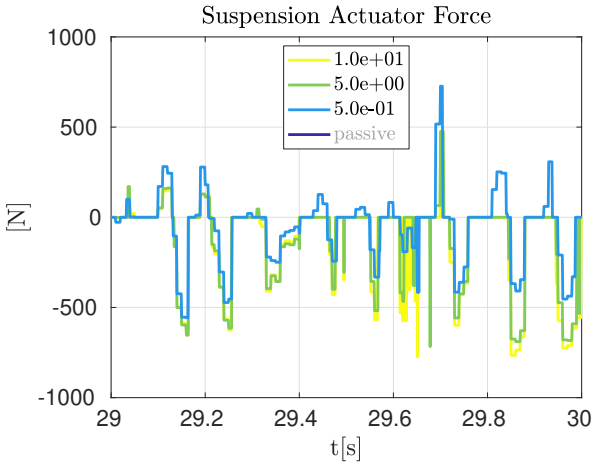

FIGURE 4.18. Plot of Suspension Actuator Force vs Time with varying α_a weighting parameter.

Other important results include the power required to operate the actuated system. Below are several power and energy plots that give insight to the system's feasibility. Figure A.16 shows that increasing the acceleration penalty results in increased power demand, and the performance is within the limits of the off-the-shelf IFA parameters chosen for simulation. Plots of the actuator forces are also shown below, and are reasonable.

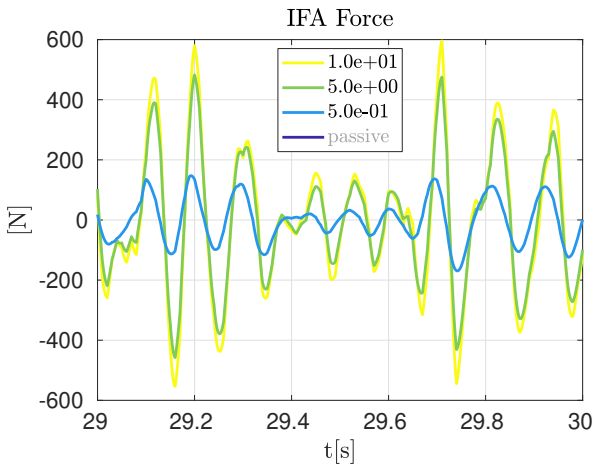

FIGURE 4.19. Plot of IFA Force vs Time with varying α_a weighting parameter.

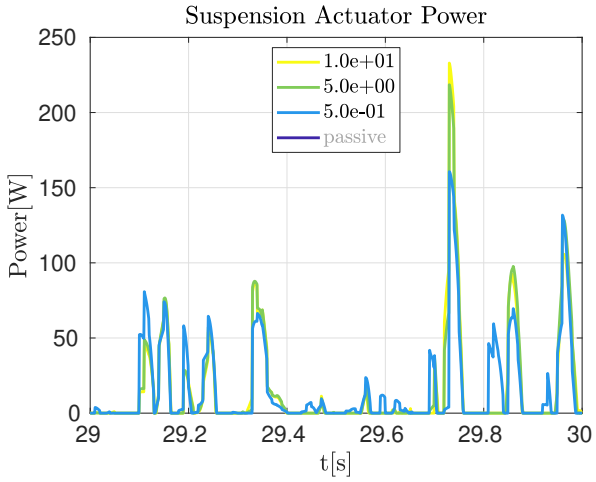

FIGURE 4.20. Plot of Suspension Actuator Power vs Time with varying α_a weighting parameter. The passivity constraint of the device is clearly evident.

The suspension passivity constraint is most clearly visible in the suspension actuator power plot, Figure 4.20. The active component load is entirely borne by the IFA, and is shown in Figure A.16.

From Equation 4.8, Figure 4.21 shows the energy demand on the battery over time. Taking the last data point of this plot as a reference, in the case with the highest penalization of α_t while the IFA power RMS is 140W, the supply-side power demand is only around 66W.

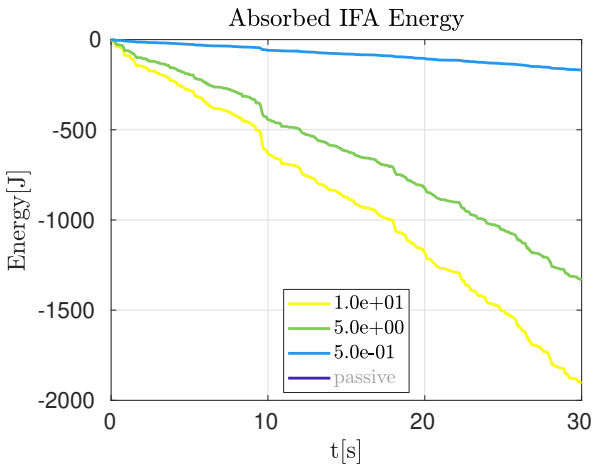

FIGURE 4.21. Plot of Absorbed IFA Energy vs Time with varying α_a weighting parameter.

4.3.2. Varying α_t (weighting on the tire deflection). Below are simulations results for various selections of α_t while $\alpha_a = 10$. In all simulations in this section, the RMS tire deflection and RMS sprung mass acceleration are less than the passive system.

Figure 4.22 shows that the sprung mass acceleration has been reduced at the ride frequency and at in the human-sensitive frequency ranges. Figure 4.23 shows the tire deflection FFT, which shows that the tire deflection penalization should not be reduced too far, lest the resonance increases. Figures A.19 and A.20 show that the MPC is properly maintaining the specific hard constraints and, in the context of other plots, validates the controlled system as being effective at managing primary and secondary objectives for this input condition.

Other important results include the power required to operate the actuated system. Below are several power and energy plots that give insight to the system's feasibility. Figure 4.24 shows that higher penalization of tire deflection higher results in increased power demand; however, the peaks are within the limits of the off-the-shelf IFA parameters chosen for simulation. Plots of the actuator forces are also shown below, and are reasonable.

Using Equation 4.8, Figure 4.25 shows the energy demand on the battery over time Taking the last data point of this plot as a reference, it says that, in the case with the highest penalization of α_t, while the total combined actuator power RMS is 256W, the supply-side power demand is only around 115W.

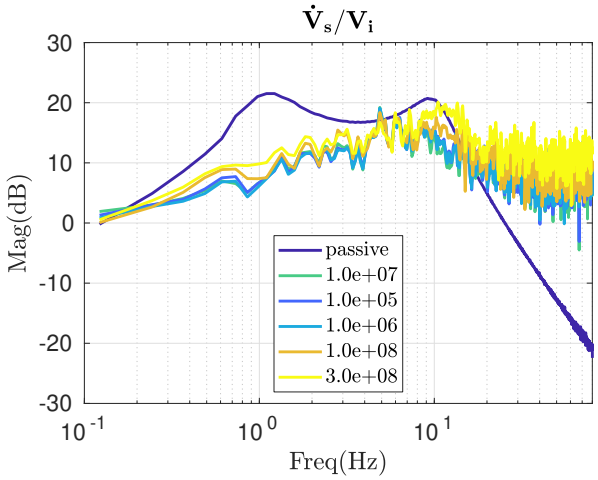

FIGURE 4.22. Plot of Sprung Mass Acceleration FFT vs Frequency with varying α_t weighting parameter.

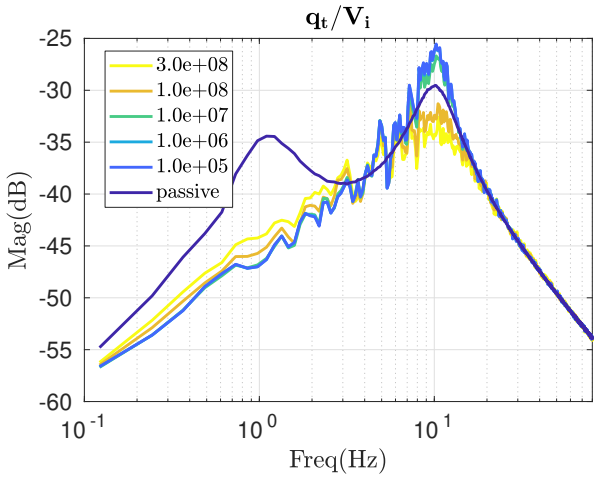

FIGURE 4.23. Plot of Tire Deflection FFT vs Frequency with varying α_t weighting parameter.

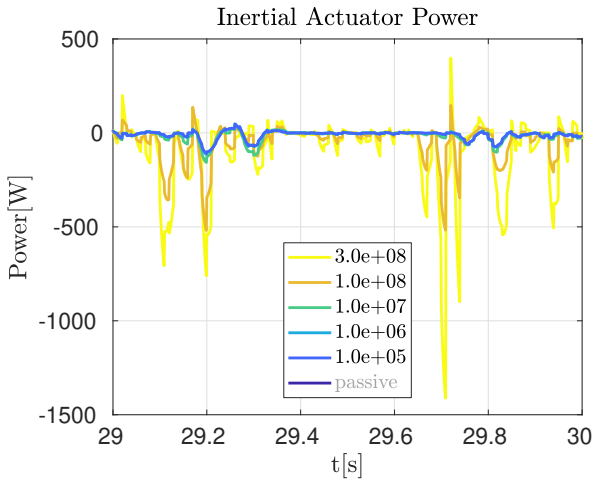

FIGURE 4.24. Plot of IFA Power vs Time with varying α_t weighting parameter.

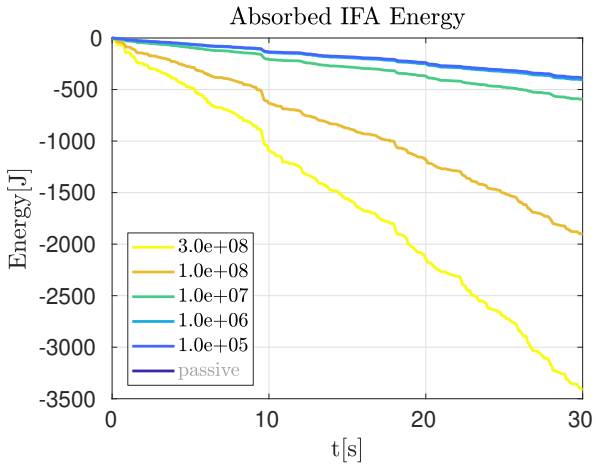

FIGURE 4.25. Plot of Absorbed Energy vs Time with varying α_t weighting parameter.

4.4. Quarter Car Traversing a Bump

The previous sections showed results of the controlled system traversing a random road. In this section, the vehicle is made to traverse a single bump to observe transient behavior. A bump profile is generated and shown in Figure 4.26. The vehicle is traveling at 40mph and has the same state and input constraints as hte previous section. Referring to Equation 3.25, the simulation parameters for results shown in this section are

$$\alpha_q = 0 \tag{4.14}$$

$$\alpha_a = \begin{bmatrix} 5 & 5e-1 & 5e0 & 1e1 \end{bmatrix} \tag{4.15}$$

$$\alpha_t = 1e8 \tag{4.16}$$

$$\alpha_F = 4e-3 \tag{4.17}$$

$$\alpha_V = 3e-2 \tag{4.18}$$

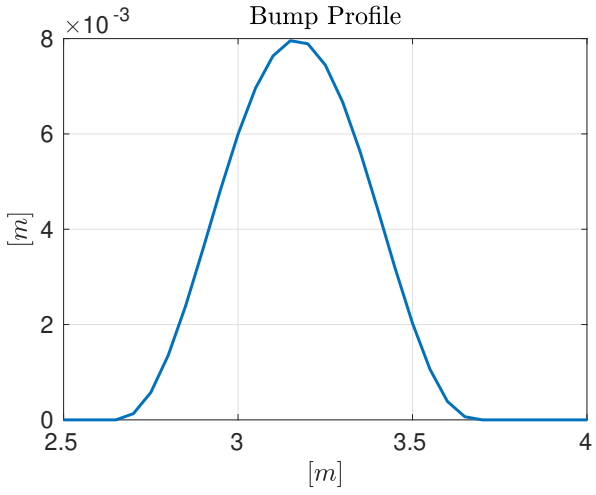

FIGURE 4.26. Plot of road input bump profile vs time.

4.4.1. Fully Active. Relevant output signal plots for the fully active simulation are shown below. The plots clearly show the actuators preparing the controlled system prior to the bump. Figures 4.27, 4.28 and 4.29 show that the peak-to-peak and absolute amplitudes are reduced, and that the system reaches a steady state more quickly than the passive system.

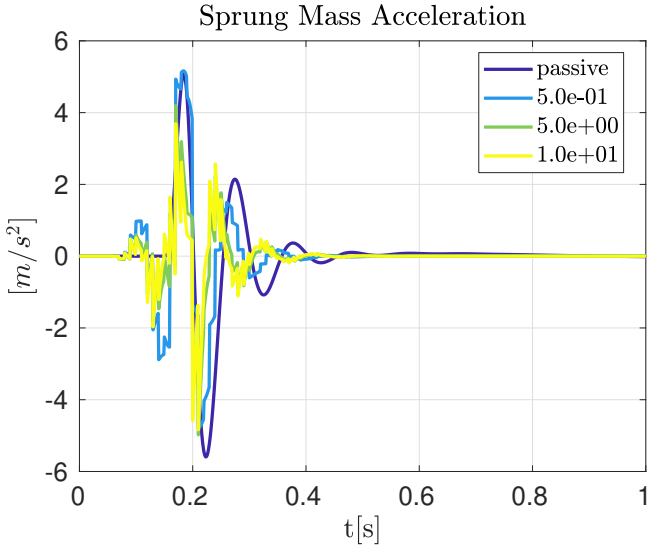

FIGURE 4.27. Plot of Sprung Mass Acceleration vs Time with varying α_a weighting parameter.

The inputs calculated from the control and applied to the system are shown in Figures 4.31 and 4.32.

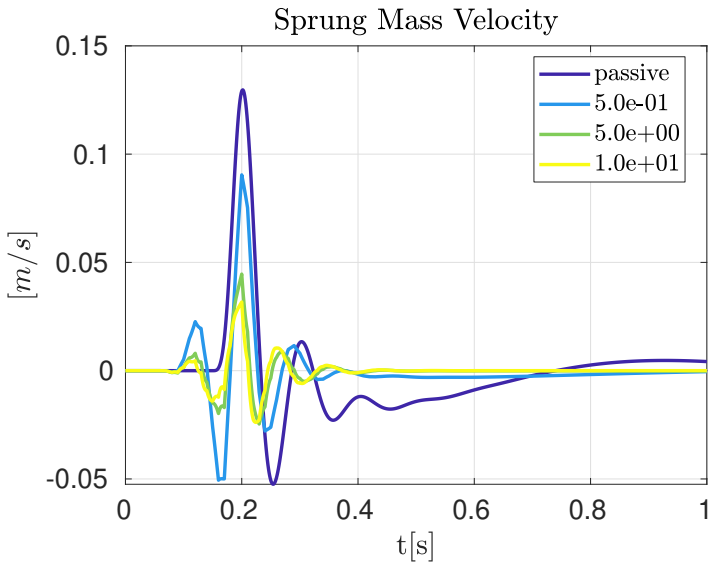

FIGURE 4.28. Plot of Sprung Mass Velocity vs Time with varying α_a weighting parameter.

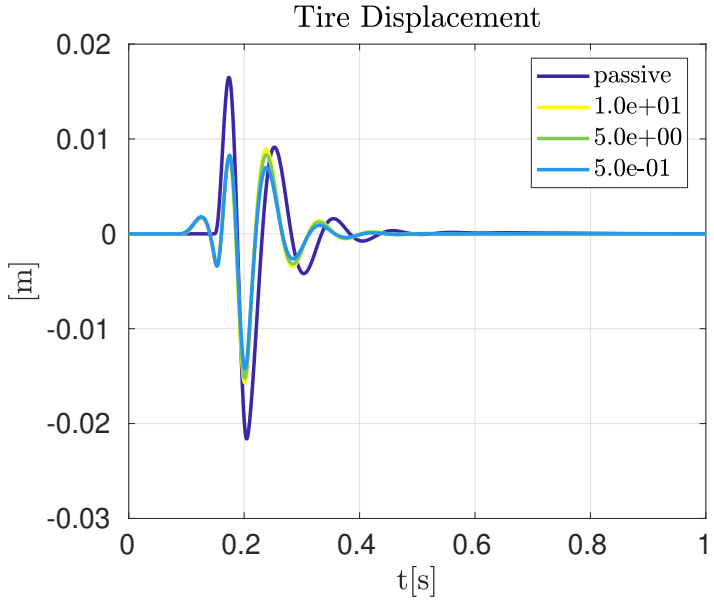

FIGURE 4.29. Plot of Tire Displacement vs Time with varying α_a weighting parameter. In this plot, the control preview's effect on the outputs is evident.

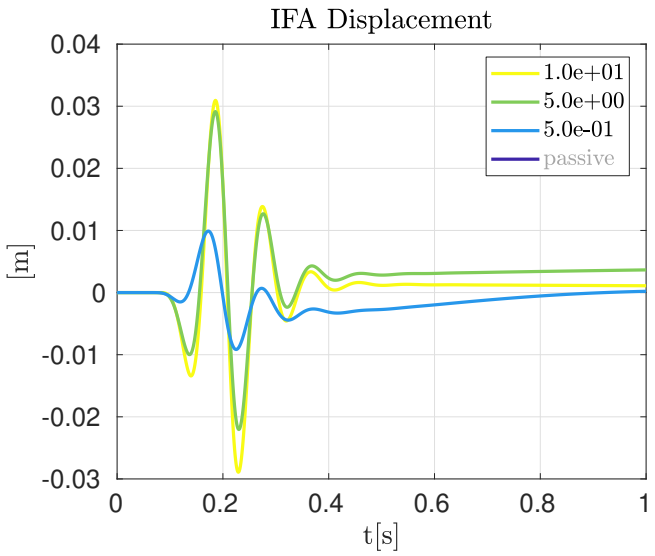

FIGURE 4.30. Plot of IFA Displacement vs Time with varying α_a weighting parameter.

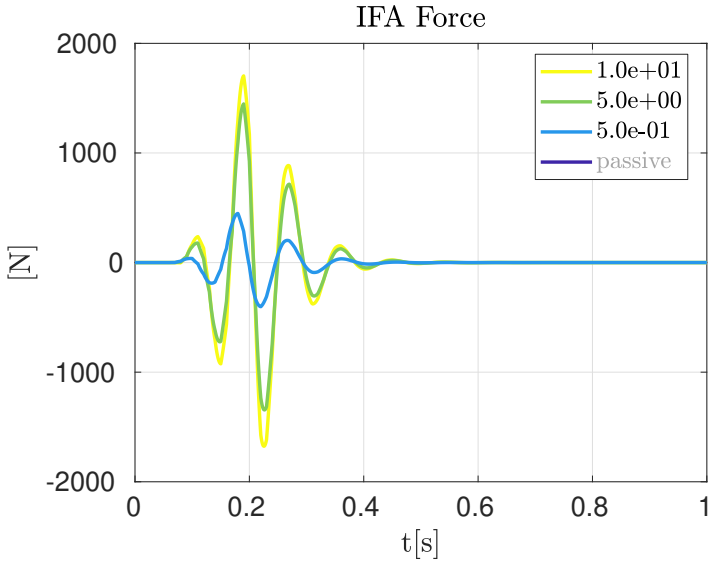

FIGURE 4.31. Plot of IFA Force vs Time with varying α_a weighting parameter.

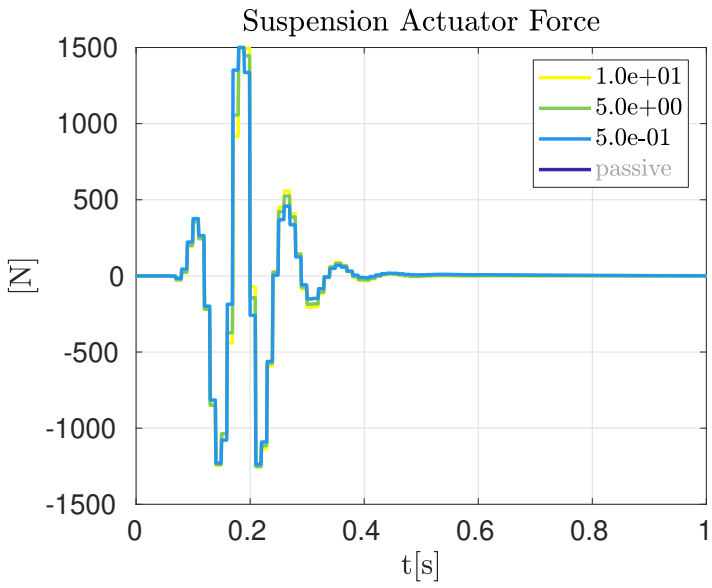

FIGURE 4.32. Plot of Suspension Actuator Force vs Time with varying α_a weighting parameter.

4.4.2. Semi-Active. Relevant output signal plots for the semi-active simulation are shown below. The plots clearly show the actuators preparing the controlled system prior to the bump. Figures 4.33, 4.34 and 4.35 show that the peak-to-peak and absolute amplitudes are reduced, and that the system reaches a steady state more quickly than the passive system.

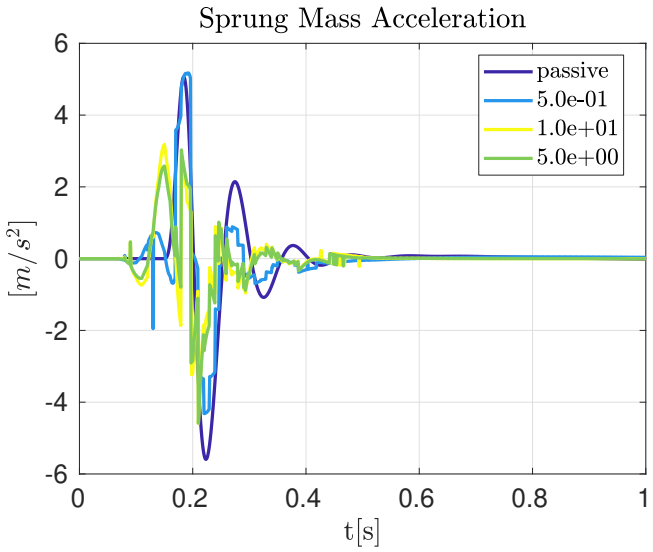

FIGURE 4.33. Plot of Sprung Mass Acceleration vs Time with varying α_a weighting parameter.

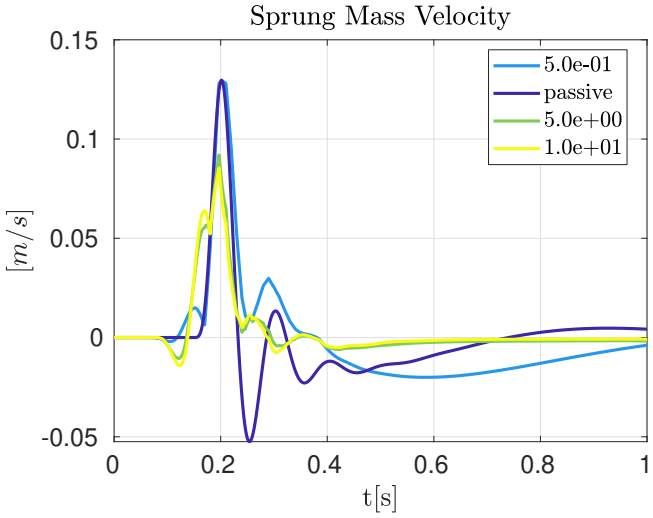

FIGURE 4.34. Plot of Sprung Mass Velocity vs Time with varying α_a weighting parameter.

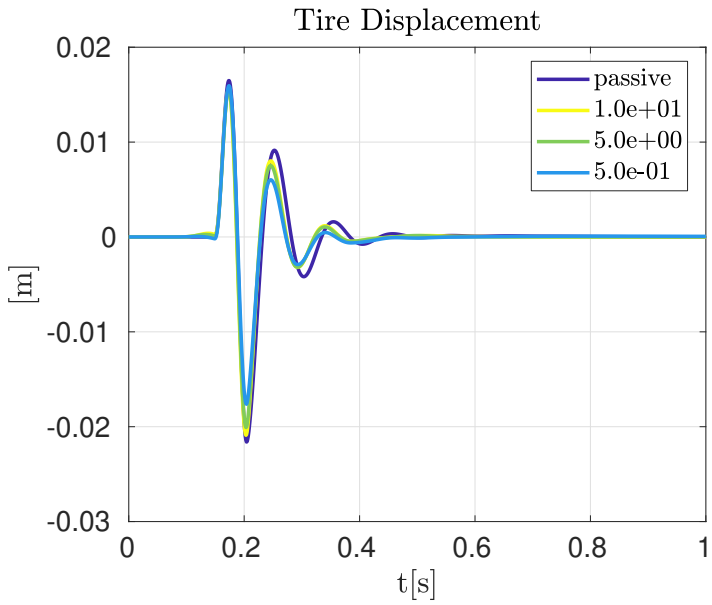

FIGURE 4.35. Plot of Tire Displacement vs Time with varying α_a weighting parameter.

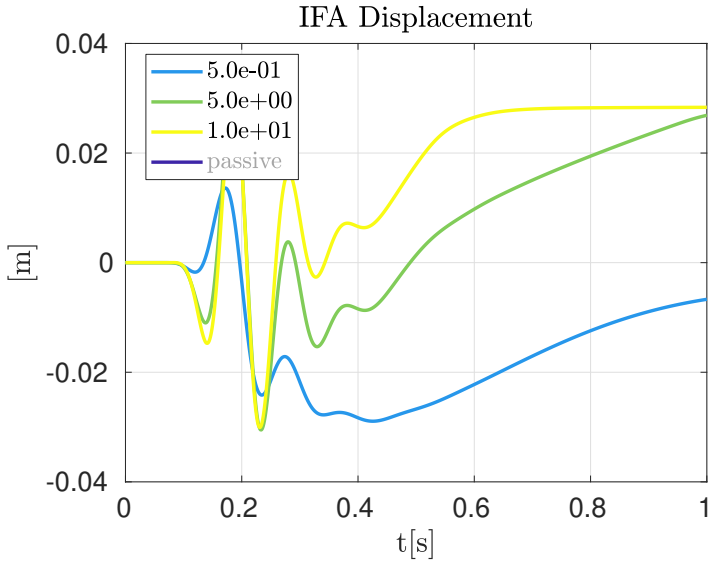

FIGURE 4.36. Plot of IFA Displacement vs Time with varying α_a weighting parameter.

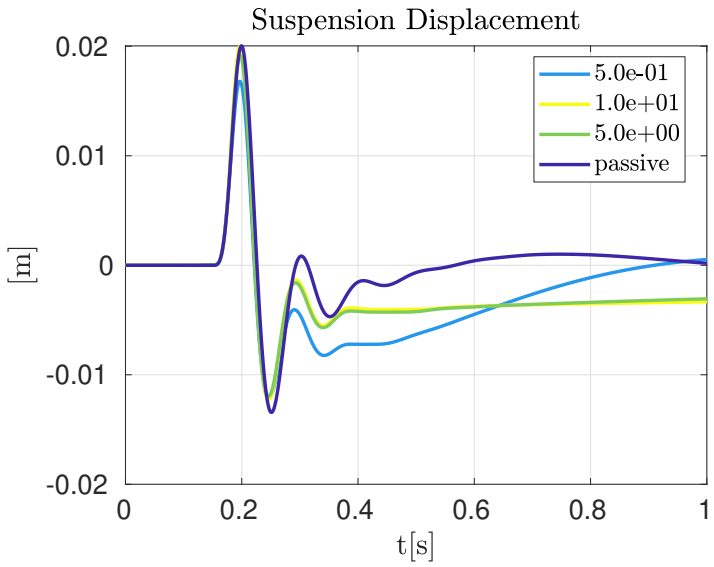

FIGURE 4.37. Plot of Suspension Displacement vs Time with varying α_a weighting parameter.

The inputs calculated from the control and applied to the system are

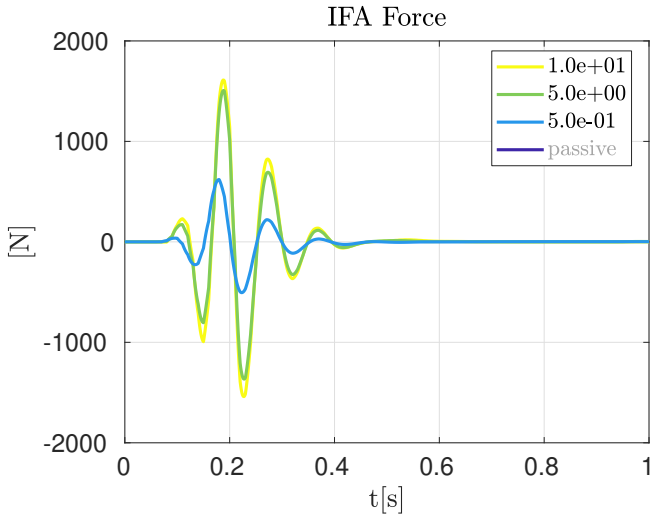

FIGURE 4.38. Plot of IFA Force vs Time with varying α_a weighting parameter.

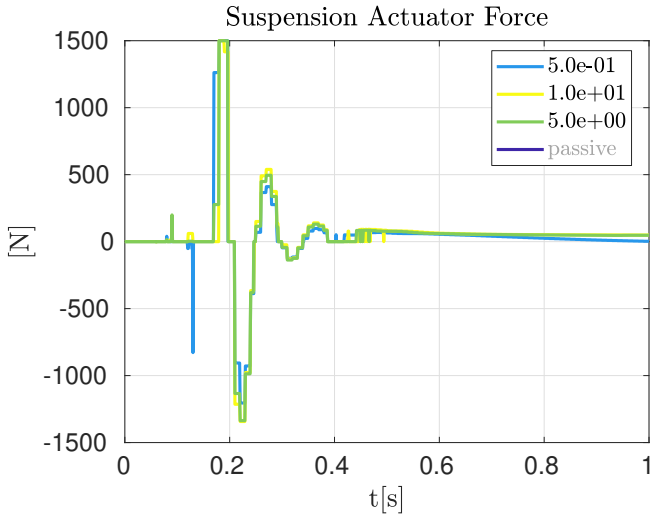

FIGURE 4.39. Plot of Suspension Actuator Force vs Time with varying α_a weighting parameter.

4.5. Discussion

The augmented QC model has been used to validate the proposed active suspension configuration incorporating an IFA along with active- and semi-active conventional actuators. These results

show that, for actuators specified in the 100W range and with minimal cost to the supply energy of the vehicle, a vehicle can be made to meet both comfort and handling metrics. The analysis of preview horizon shows that not much future information is needed to take advantage of that foreknowledge of the controller to keep the vehicle states and signals following a more desirable trajectory.

.

CHAPTER 5

Validation With High Order Model

In this chapter, the high order vehicle model previously discussed is used as a validation platform in the place of real-vehicle testing. The controlled system utilizes the exact same control scheme as the previous section, except utilized at each suspension unit. In each corner, the independent controller assumes that the suspension top mount connects to an independent mass equal to exactly $\frac{1}{4}$ of the weight of the real vehicle sprung mass. The sensor information fed to the internal Quarter Car (QC) model of the Model Predictive Control (MPC) is the velocity of the top mount point. Control parameters N and Δt maintain their same values as from the preceding chapter.

The control weightings were changed slightly after some tuning of the controllers in simulation with the high order model. One interesting result is that performance is better in the high order vehicle when the tire weighting is moved from the tire displacement to the tire spring velocity. This is because in a steady state turn, the actuators would apply constant inputs to try to minimize the tire displacement, which is impossible without a true inertial reference for the force actuators.

$$\alpha_q = 444 \tag{5.1}$$

$$\alpha_a = \begin{bmatrix} 102 & 194 \end{bmatrix} \tag{5.2}$$

$$\alpha_t = 6e4 \tag{5.3}$$

$$\alpha_F = 0 \tag{5.4}$$

$$\alpha_V = 4e - 9 \tag{5.5}$$

5.1. Step Steer Traversing a Random Road

The vehicle is given an initial velocity of 40mph, and a cruise control is implemented to maintain forward speed. At time $t = 0$, the vehicle is given a step steer. Two scenarios are simulated: active and semi-active suspension actuator.

5.1.1. Fully Active Suspension. The results for the fully active suspension are shown in the following plots. Summary results from the simulated step steer are shown in Table 5.1. The high level signal targets of decreased vertical acceleration and increased yawrate and lateral acceleration are met.

	$a_{lat,RMS}[m/s^2]$	$\omega_{z,RMS}[rad/s]$	$a_{vert,RMS}[m/s^2]$	$\text{Power}_{total,RMS}[W]$
Passive	2.921	0.1672	0.626	-
$\alpha_a = 102$	2.935	0.1683	0.400	139
$\alpha_a = 193$	2.994	0.1717	0.560	363

TABLE 5.1. Summary of high level signal outputs from high order simulation for fully active actuated system.

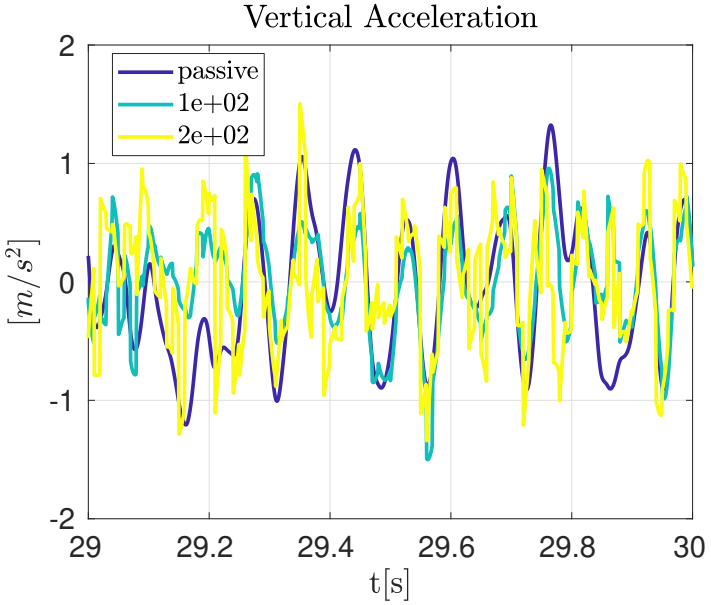

FIGURE 5.1. Plot of Vertical Acceleration vs Time with varying α_a weighting parameter.

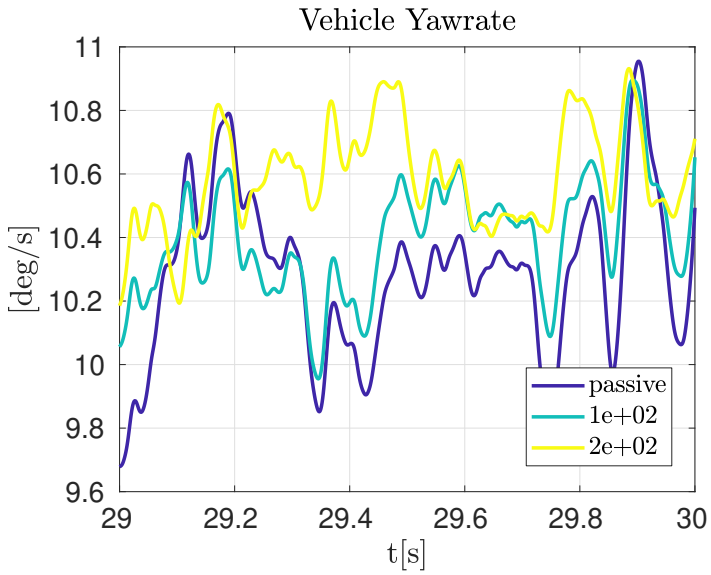

FIGURE 5.2. Plot of Vehicle Yawrate vs Time with varying α_a weighting parameter.

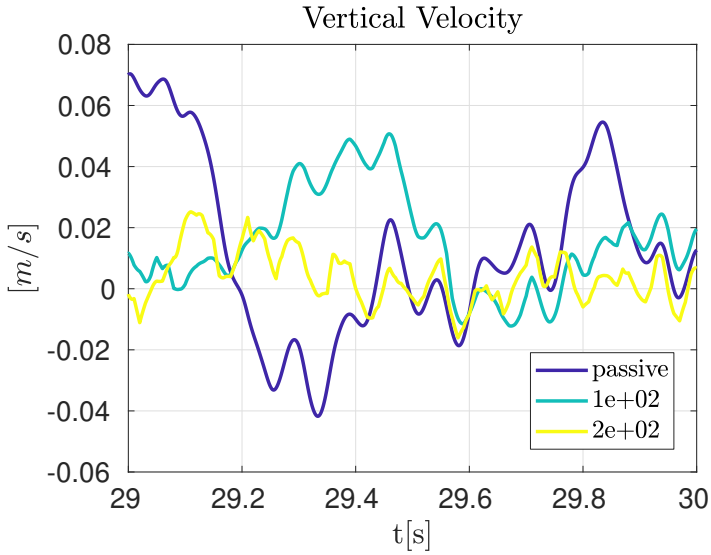

FIGURE 5.3. Plot of Sprung Mass Vertical Velocity vs Time with varying α_a weighting parameter.

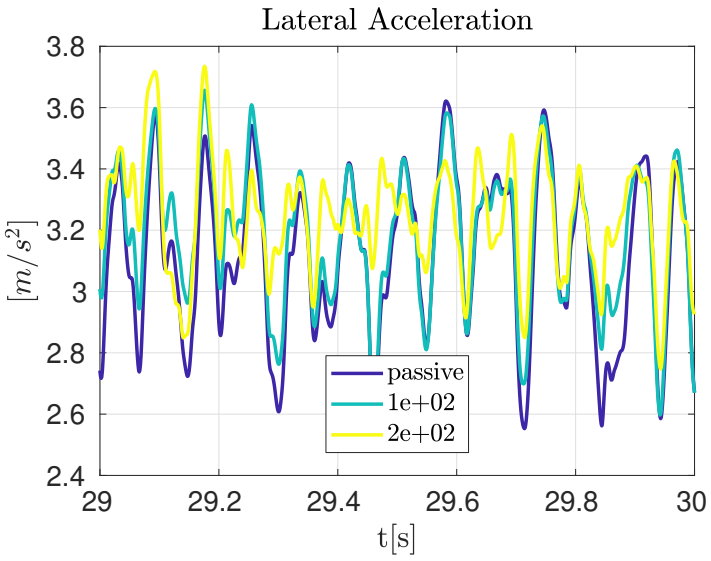

FIGURE 5.4. Plot of Lateral Acceleration vs Time with varying α_a weighting parameter.

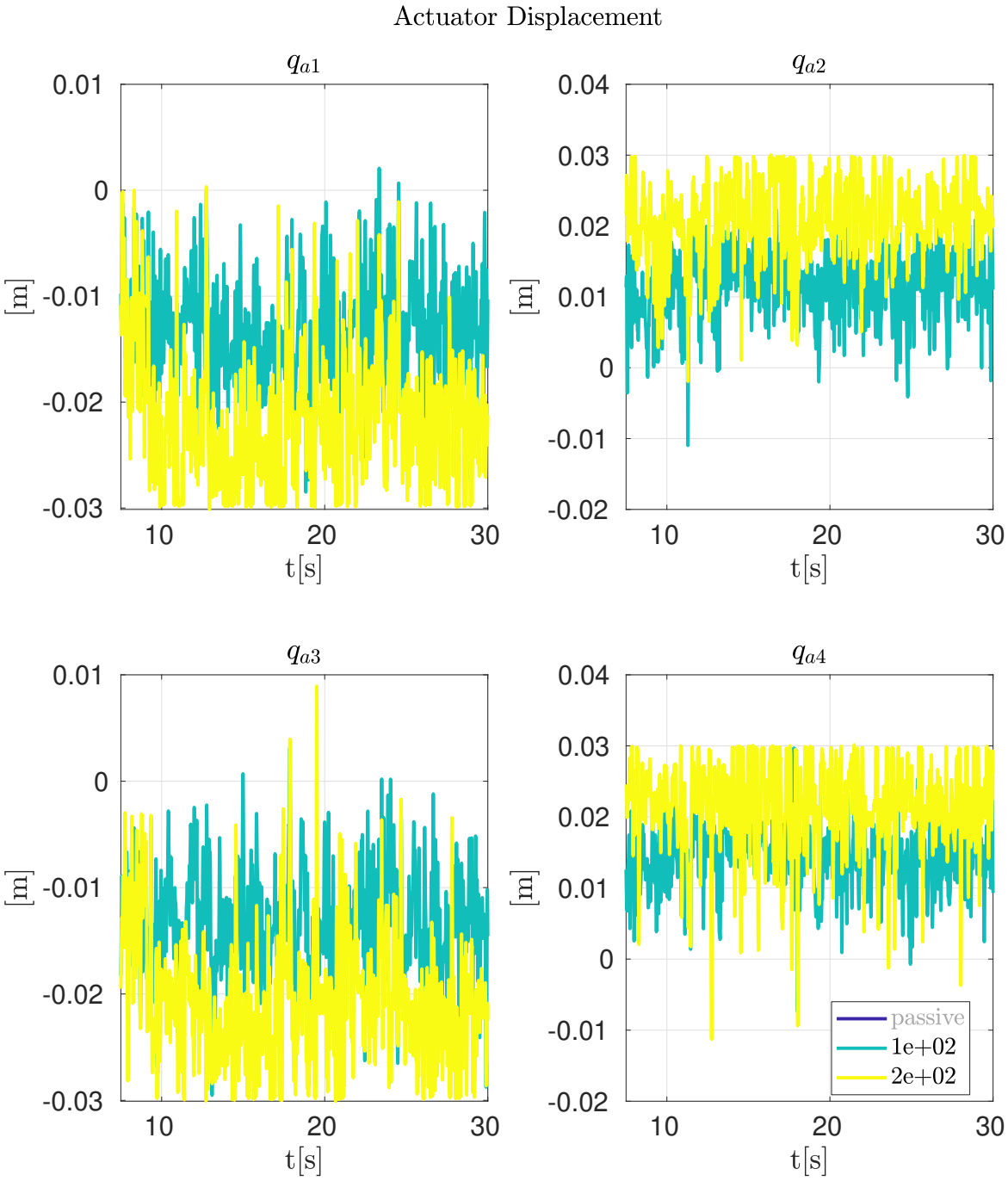

FIGURE 5.5. Plot of IFA Displacement vs Time with varying α_a weighting parameter.

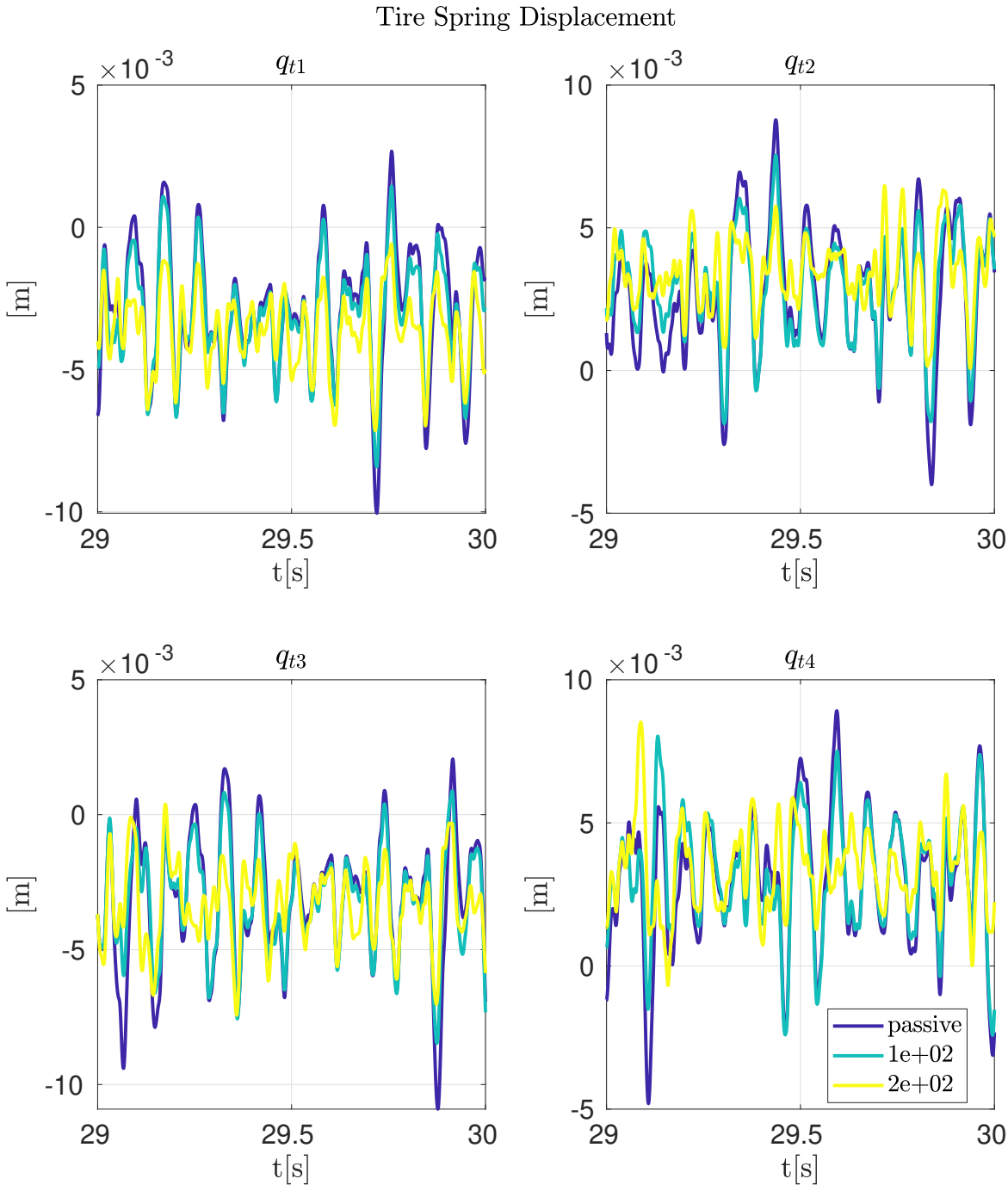

FIGURE 5.6. Plot of Tire Spring Displacements vs Time with varying α_a weighting parameter.

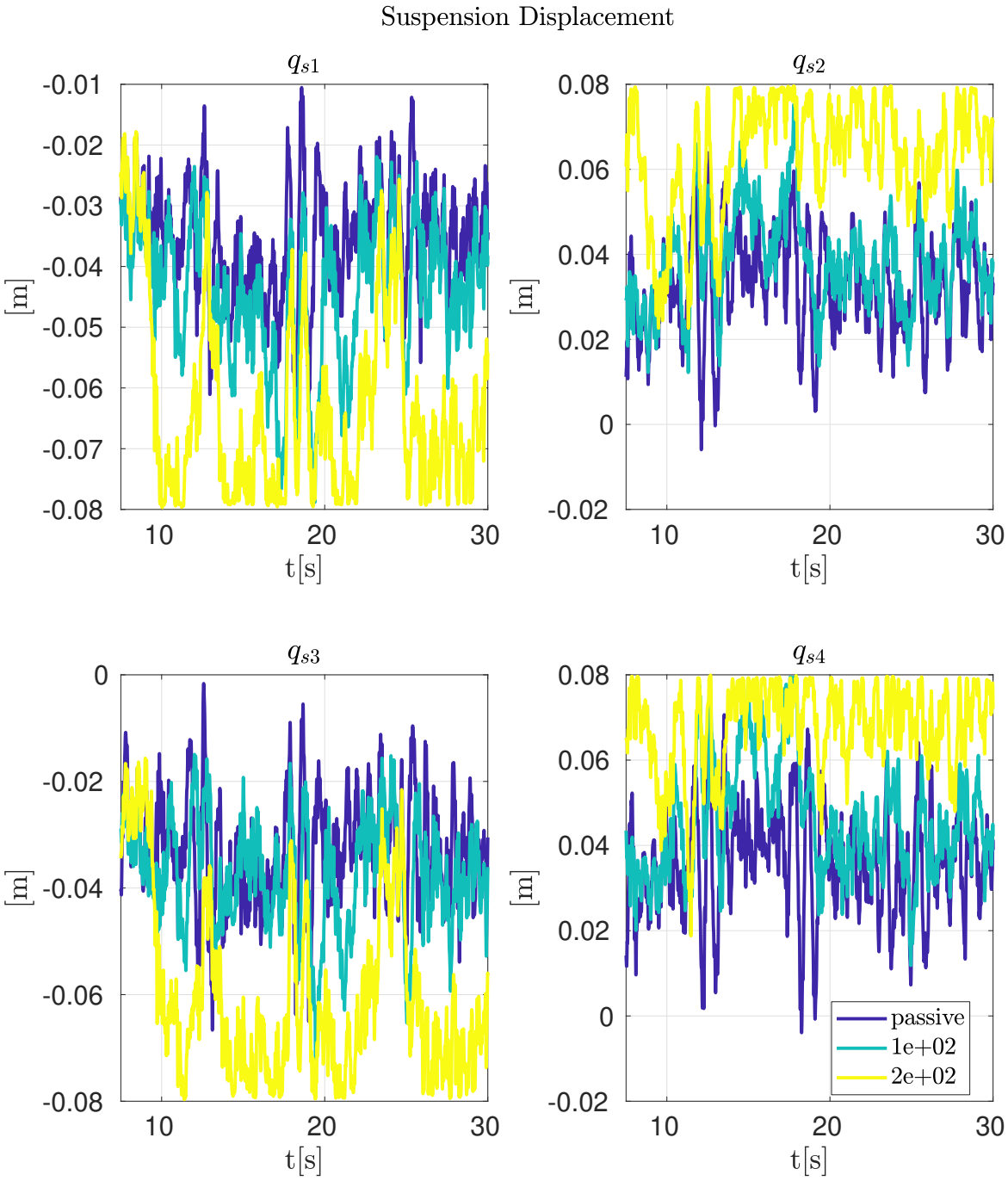

FIGURE 5.7. Plot of Suspension Displacements vs Time with varying α_a weighting parameter.

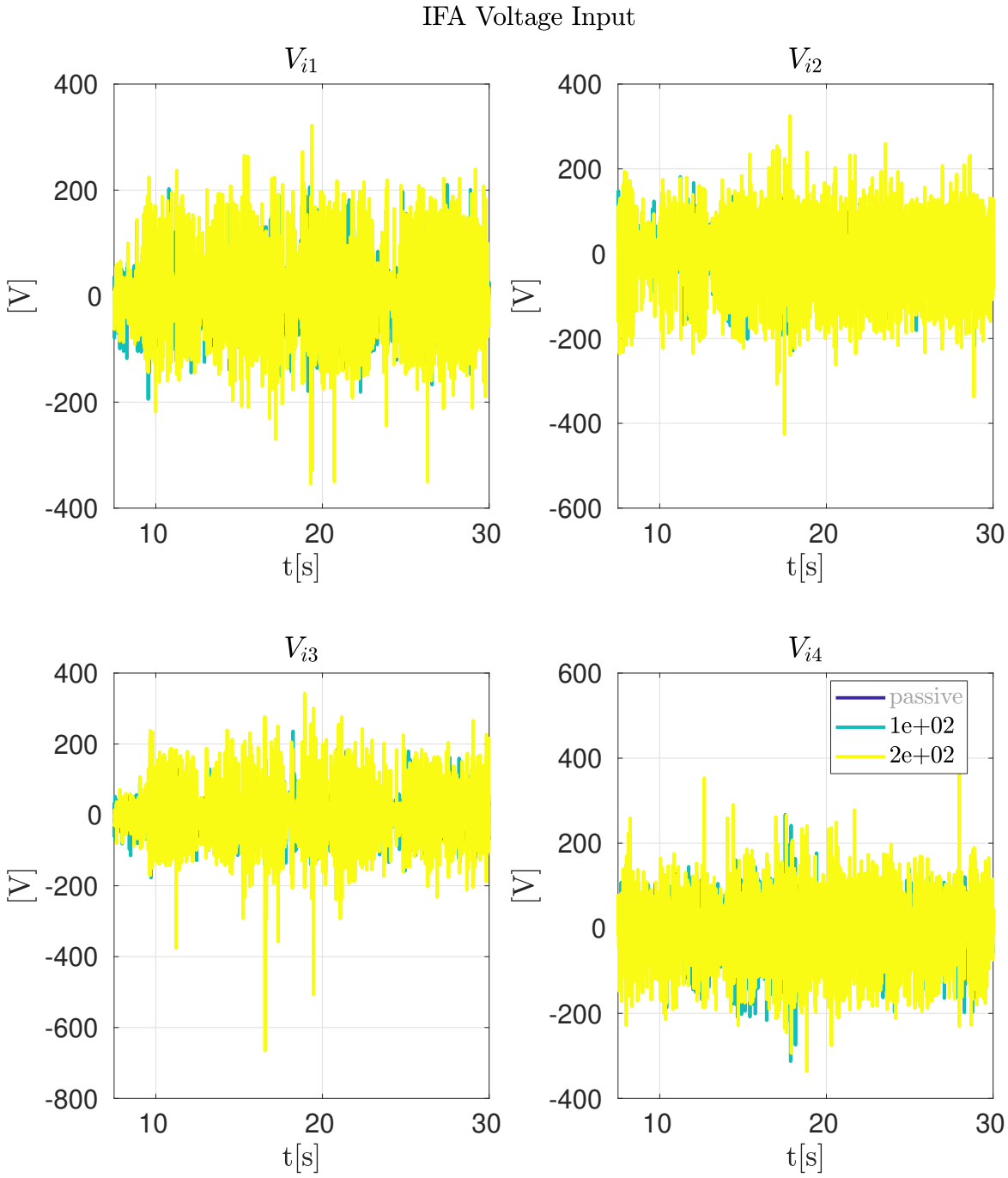

FIGURE 5.8. Plot of IFA Voltage Input vs Time with varying α_a weighting parameter.

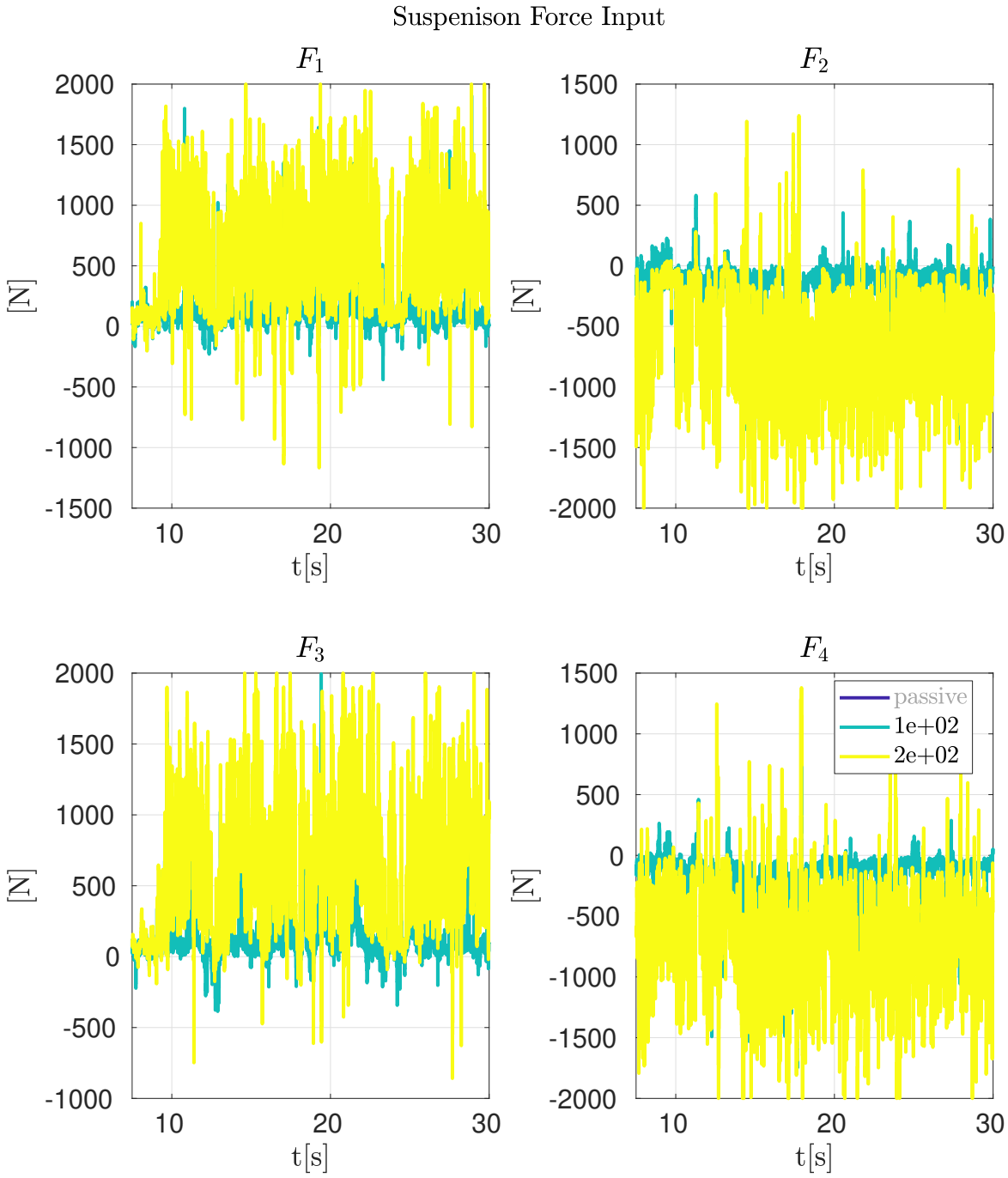

FIGURE 5.9. Plot of Suspension Force Input vs Time with varying α_a weighting parameter.

5.1.2. Semi-Active Suspension. The results for the semi-active suspension are shown in the following plots. Summary results from the simulated step steer are shown in Table 5.2. The high level signal targets of decreased vertical acceleration and increased yawrate and lateral acceleration are met.

	$a_{lat,RMS}[m/s^2]$	$\omega_{z,RMS}[rad/s]$	$a_{vert,RMS}[m/s^2]$	$\text{Power}_{IFA_{Total},RMS}[W]$
Passive	2.921	0.1672	0.626	-
$\alpha_a = 102$	2.930	0.1678	0.447	115
$\alpha_a = 193$	2.932	0.1679	0.459	199

TABLE 5.2. Summary of high level signal outputs from high order simulation for semi active actuated system.

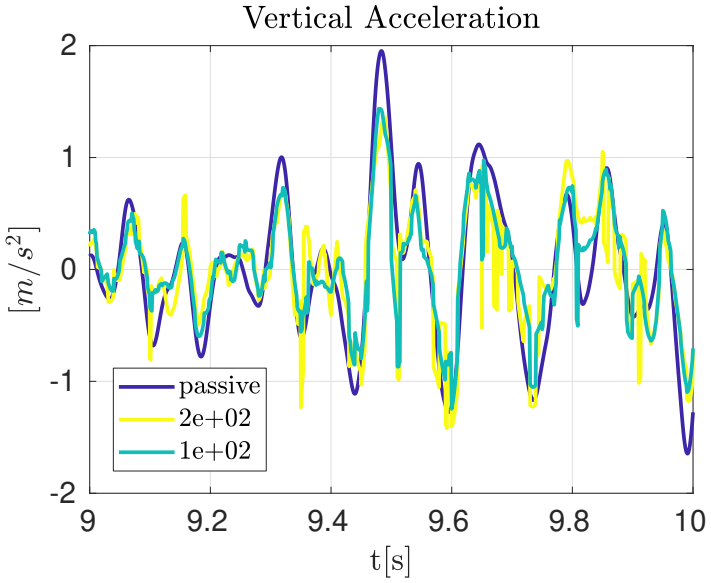

FIGURE 5.10. Plot of Vertical Acceleration vs Time with varying α_a weighting parameter.

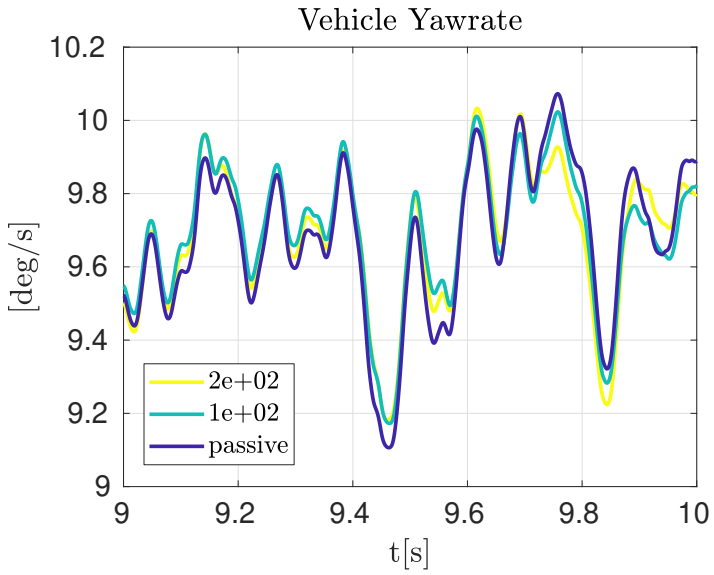

FIGURE 5.11. Plot of Vehicle Yawrate vs Time with varying α_a weighting parameter.

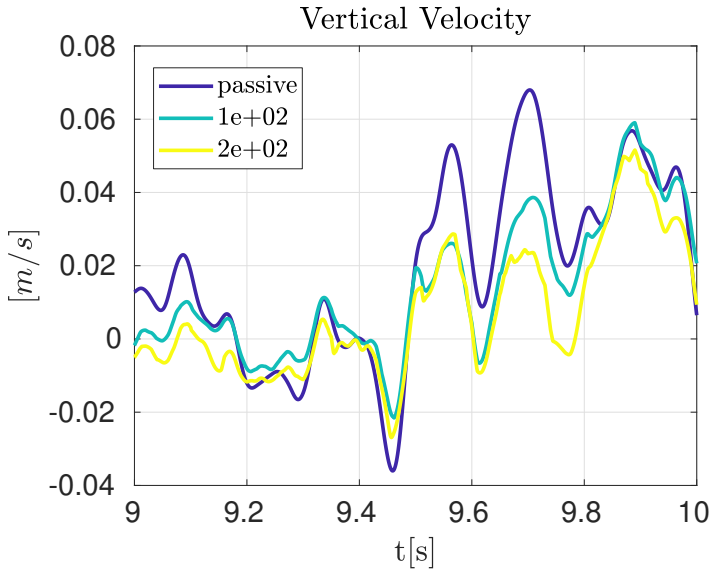

FIGURE 5.12. Plot of Sprung Mass Vertical Velocity vs Time with varying α_a weighting parameter.

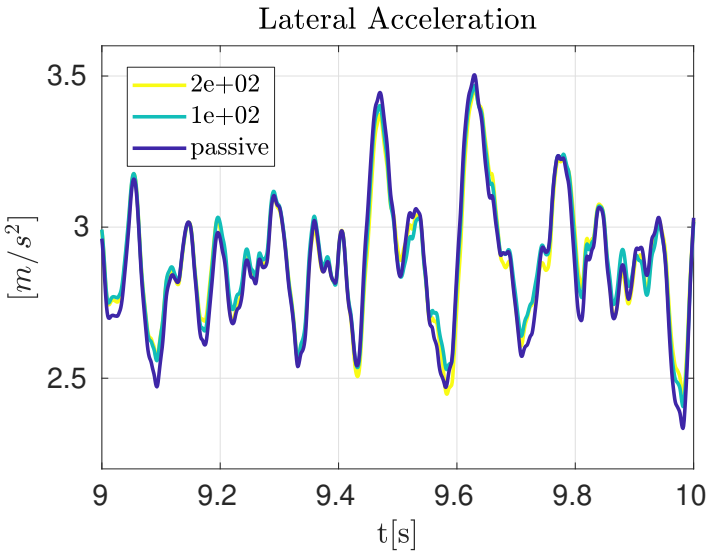

FIGURE 5.13. Plot of Lateral Acceleration vs Time with varying α_a weighting parameter.

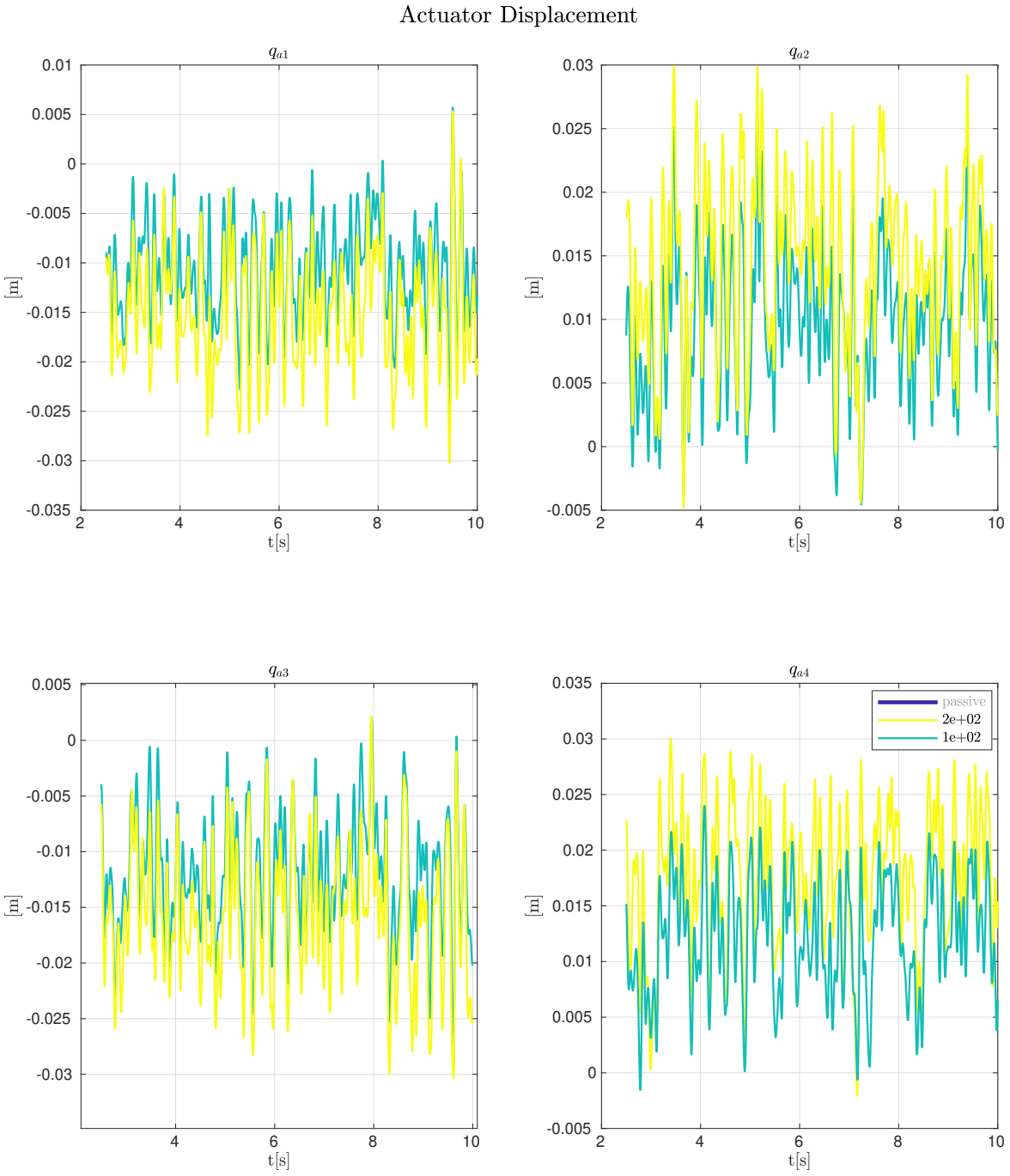

FIGURE 5.14. Plot of IFA Displacement vs Time with varying α_a weighting parameter.

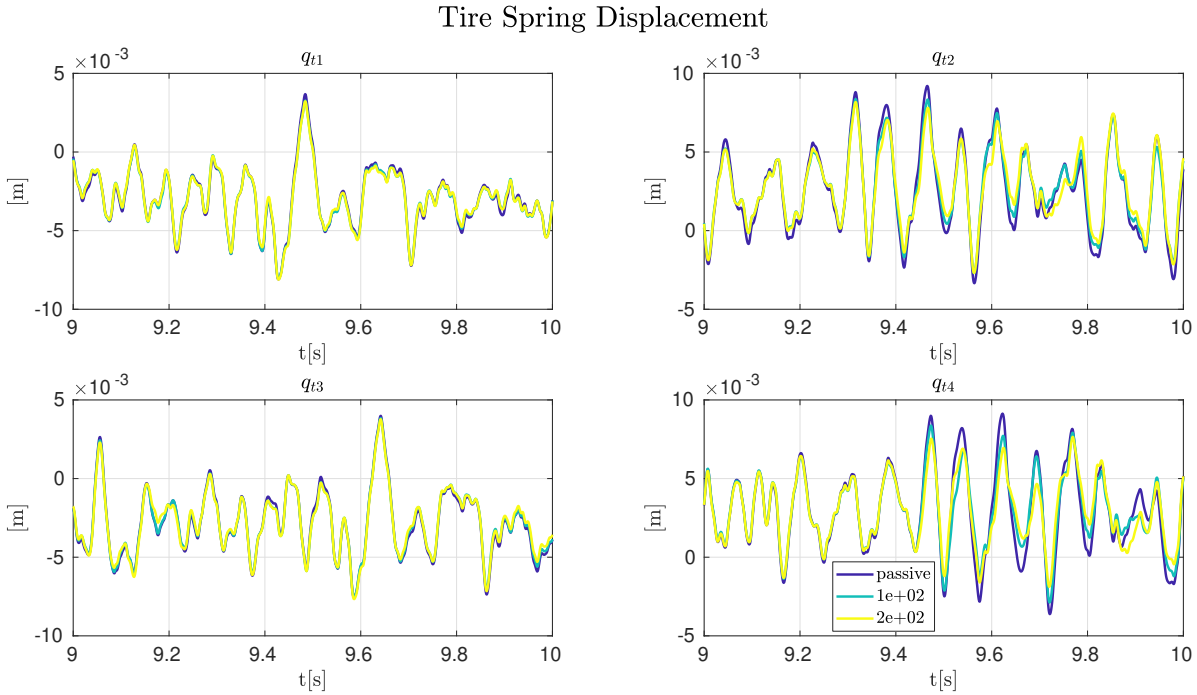

FIGURE 5.15. Plot of Tire Spring Displacements vs Time with varying α_a weighting parameter.

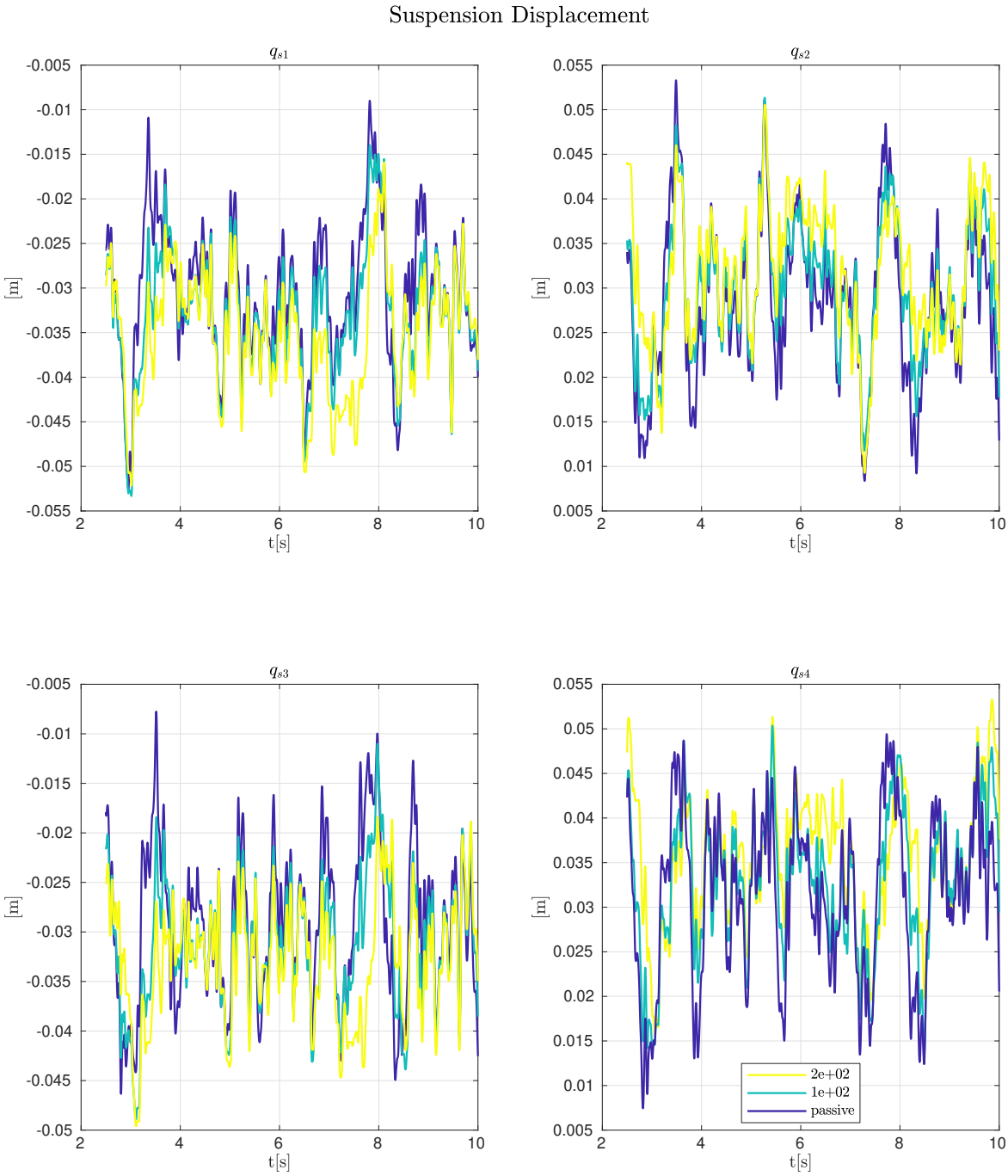

FIGURE 5.16. Plot of Suspension Displacements vs Time with varying α_a weighting parameter.

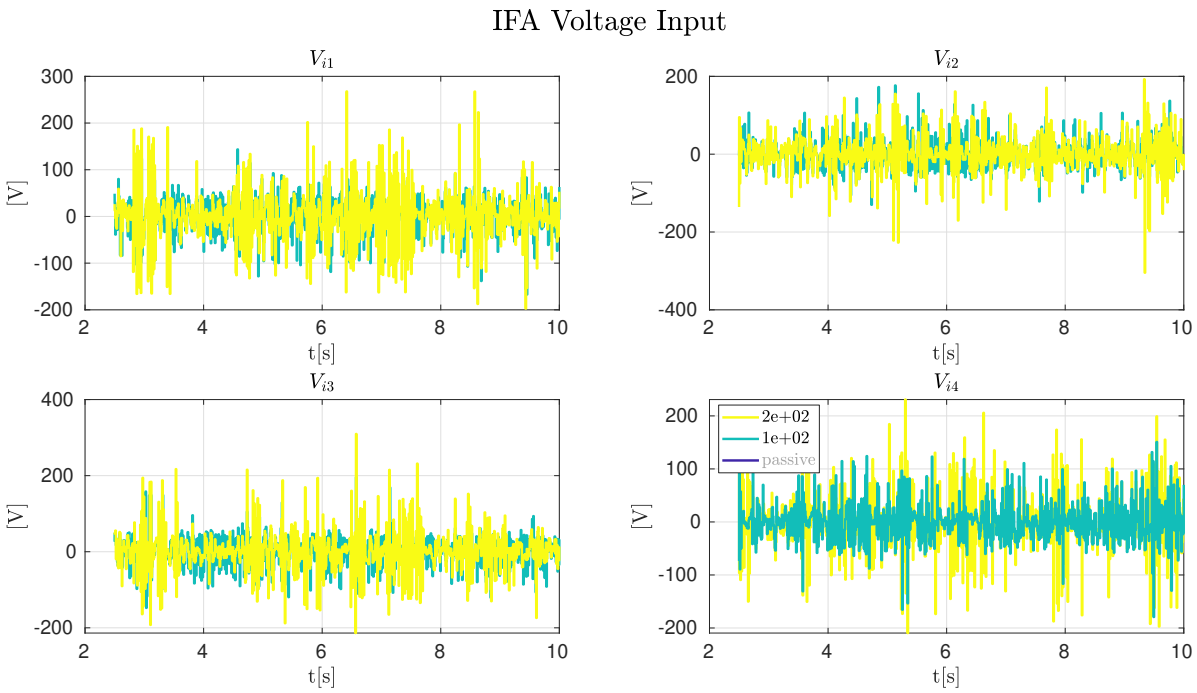

FIGURE 5.17. Plot of IFA Voltage Input vs Time with varying α_a weighting parameter.

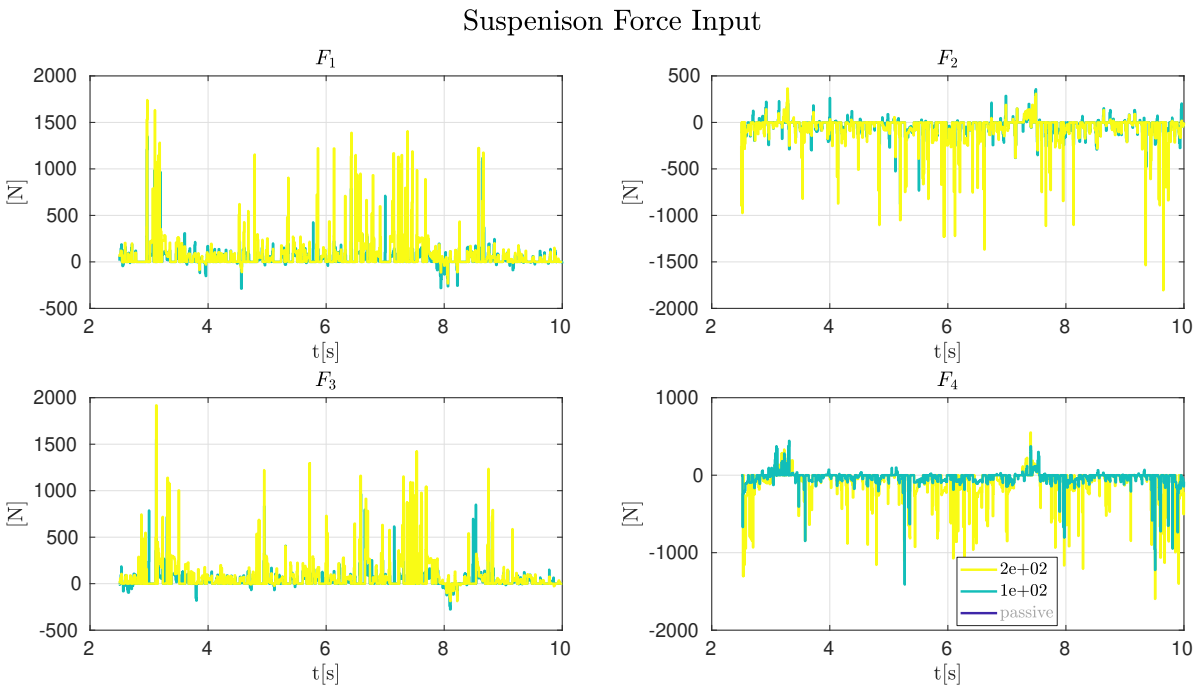

FIGURE 5.18. Plot of Suspension Force Input vs Time with varying α_a weighting parameter.

5.2. Discussion of Results

The results presented in this chapter show the capabilities of the controlled suspension system. The benefit of these results lie in the ability of the controlled system to minimize the sprung mass vertical acceleration while also benefiting lateral dynamics through minimization of tire vertical dynamic deflection.

The semi-active system does not perform as well as the fully active system. It is clear that the high level signals most negatively impacted by the semi-active constraint imposed on the conventional suspension actuator are in the lateral dynamics. However, despite the non-ideal non-linearity introduced by the semi-active constraint, the system still shows desirable behavior, and behaves better than the passive system.

The use of low order (QC) models in the corner MPCs implies that these independent actuated systems behave as unknown disturbances to each other. This is a direct result of the order of internal model that was chosen for the MPC. Indeed, it is therotically possible to select a higher order internal model such that all external measured roadway disturbances would be acting on the same internal model, eliminating the mutually induced disturbances between the corners of hte vehicle. However, this method would greatly increase the size of the internal model, and this research was intended to provide a computationally realistic control implementation that highlights the benefits of the IFA controlled system.

The fully active system results shown utilize an average combined actuator power of 100W per corner. If power electronics for the real system were designed to permit bi-directional power flow, as described in Chapter 3, then the load on the vehicle's energy supply could be significantly less than 100W per corner.

As a final point of discussion, 361 high order model simulations were conducted consisting of 1 passive run and 90 30-second simulations sweeping penalization factors α_a and α_t each for 4 configurations: "Constrained," in which the constraints specified in Section 4.2 are imposed; "Unconstrained," in which these constraints are removed; and another each for Constrained and Unconstrained, except "Semi"-active in which the conventional suspension actuator can only dissipate power. All of the 364 simulations were for a steady state corner over a Class B road for a steered wheel angle of 1 degree. The Pareto Fronts plotted in Figure 5.19 show only the best-case

simulations of the 360, in which either sprung mass vertical acceleration a_s or tire deflection q_t are minimized. The lateral dynamics are represented in the right plot of Figure 5.19, in which the negative slope of the ω_z vs q_t plots indicates a positive correlation between minimized tire deflection and increased vehicle handling characteristic.

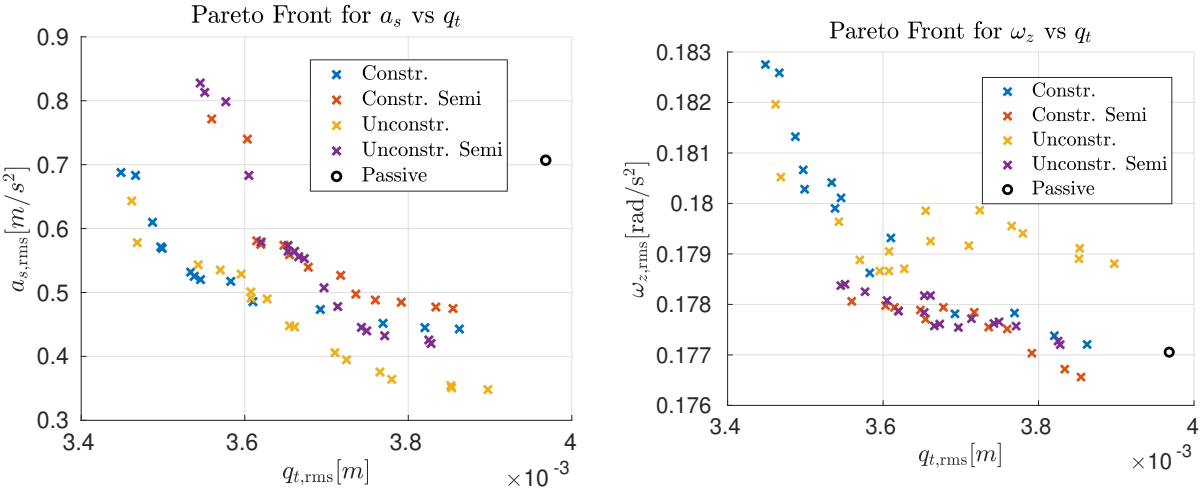

FIGURE 5.19. Pareto Front for suite of simulations sweeping α_t and α_a

The uniqueness of these results is a direct result of the system configuration proposed. The Multi-Input, Multi-Output (MIMO) controlled system of an IFA combined with a conventional suspension actuator allow for different weightings to be applied, allowing a tuner (or potentially, a driver/operator) to change relative performance trade-offs of high level signals.

.

CHAPTER 6

Conclusions

The models used for this dissertation place the inertial actuator directly onto the sprung mass. There are arguments for placing the actuator elsewhere; for instance, it could be placed directly on the unsprung mass. There are important considerations in the choice of actuator placement. If placed on the unsprung mass, the actuator would be in the best location to filter the disturbance input since there is less dynamics between the disturbance and the Inertial Force Actuator (IFA) filter. However, the added fixed weight of the actuator housing would decrease the sprung-to-unsprung mass ratio, which is known to deteriorate vehicle performance [**12**]. Alternatively, if the actuator maximum allowable displacement is sufficiently large, the actuator could potentially offset this problem and allow the tire to maintain the desired constant normal force with the ground.

When placed on the sprung mass, the actuator can directly affect one of the controlled output variables (sprung mass acceleration), but is separated by dynamics from the disturbance input. Also, since the sprung mass / proof mass ratio is rather large, significant actuator displacement and/or proof mass mass may be needed to operate effectively. Many methods of floating a proof mass for manipulation are possible, and with the continuing electrification of vehicles, batteries make for a viable medium.

The primary objectives and secondary constraints mentioned or implied (minimal variation of tire displacement from nominal; minimal sprung mass acceleration; minimal displacement of inertial force actuator from nominal; minimal power demand by active suspension system on vehicle power system) favorably suggest that research may be best cast in an optimization framework. By doing so, and due to the increased dimensional space with respect to the traditional quarter car (resulting from the proposed actuator), we believe great potential lies in this proposal.

A new actuator application has been proposed for active vehicle suspensions. The primary goals of this new system are to maximally increase vehicle handling and comfort performance metrics, with the secondary goal of minimal power demand on (or maximal power supply to) the

vehicle electrical system by the controlled actuators. The proposal is motivated by suggestions in the research that inertial forces on vehicles would garner specific advantages. This proposal emphasizes that these inertial forces can be applied using IFAs, particularly when cast as a MIMO control problem with conventional actuators.

Skyhook and optimal control results were presented. The results of these simulations are promising for further investigation and analysis of the proposed suspension platform, in part because the MIMO configuration (IFA and conventional suspension actuation) broadens the parameter and configuration space of the controlled system.

The simulation results using preview control show even further benefit of the proposed configuration. With tuning availability, the control parameters can be directly manipulated to arbitrarily select higher penalties for comfort or road holding

6.1. Future Work

The work to further this technology includes specifying preview sensor fidelity, implementing observers/estimators for the full-state feedback control, and further simulation testing in various driving scenarios of the controlled nonlinear system. Another unfinished work is testing system performance in the absence of a preview sensor; for instance, implementing the controlled suspension at the rear of the vehicle and utilizing an estimator at the front suspension to estimate the road surface in lieu of a preview sensor.

.

APPENDIX A

Additional Plots and Figures

A.1. Additional plot outputs for section 2.1

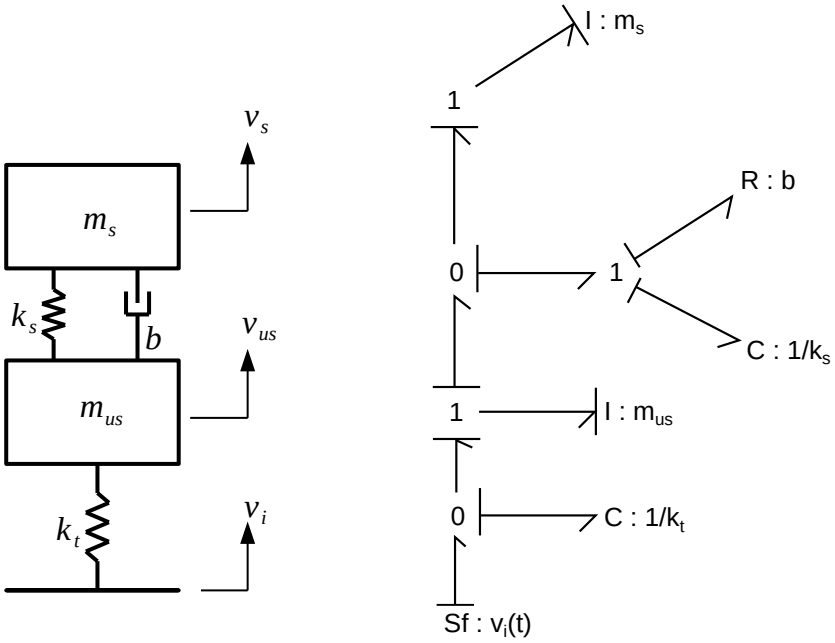

FIGURE A.1. Quarter Car (QC) schematic and bond graph

A.2. Additional plot outputs for section 4.2.1

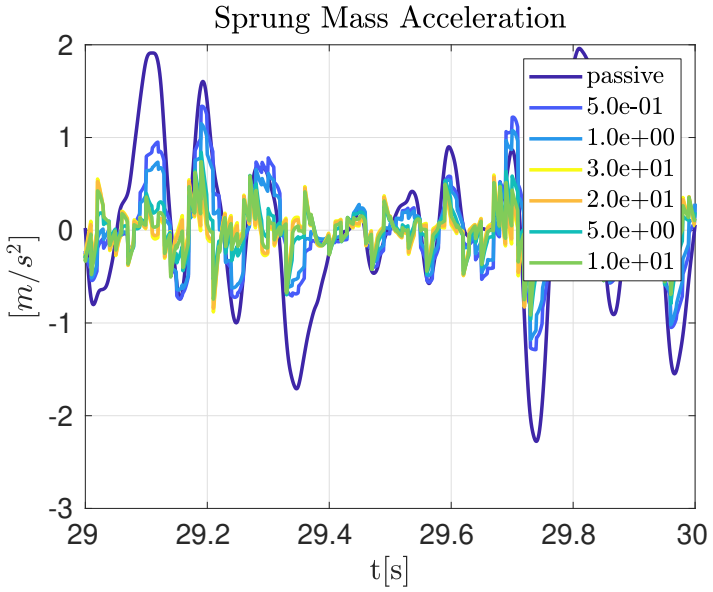

FIGURE A.2. Plot of Sprung Mass Acceleration vs Time with varying α_a weighting parameter.

[ht]

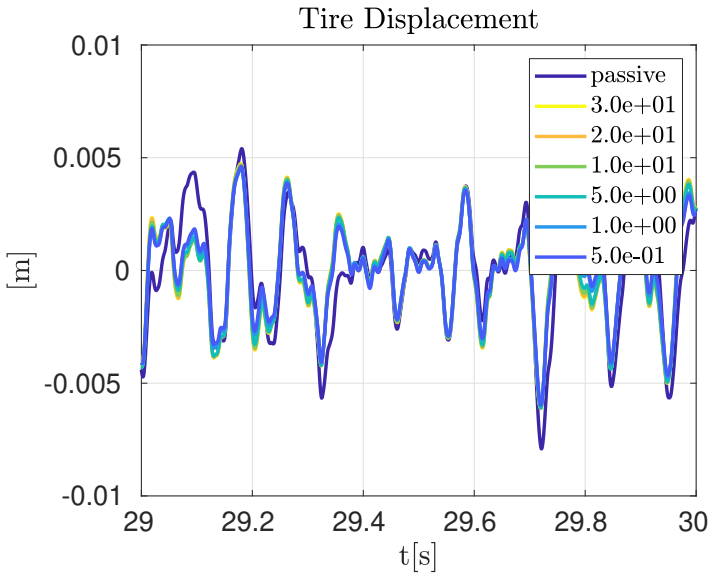

FIGURE A.3. Plot of Tire Deflection vs Time with varying α_a weighting parameter.

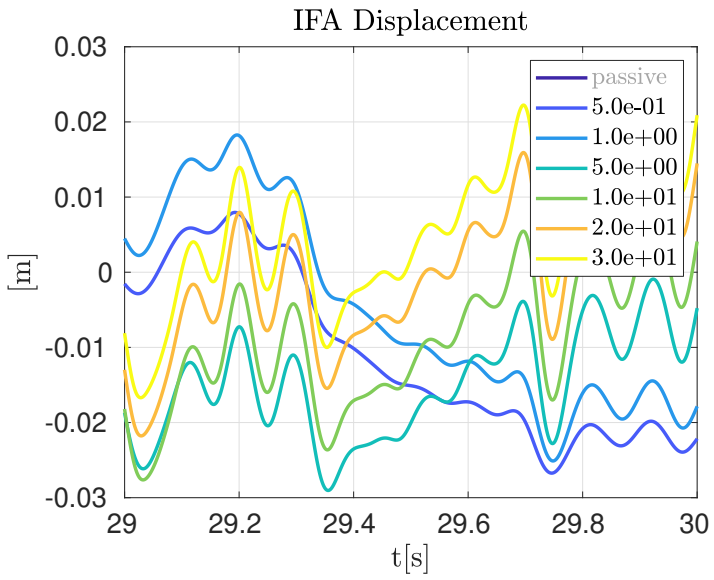

FIGURE A.4. Plot of IFA Deflection vs Time with varying α_a weighting parameter.

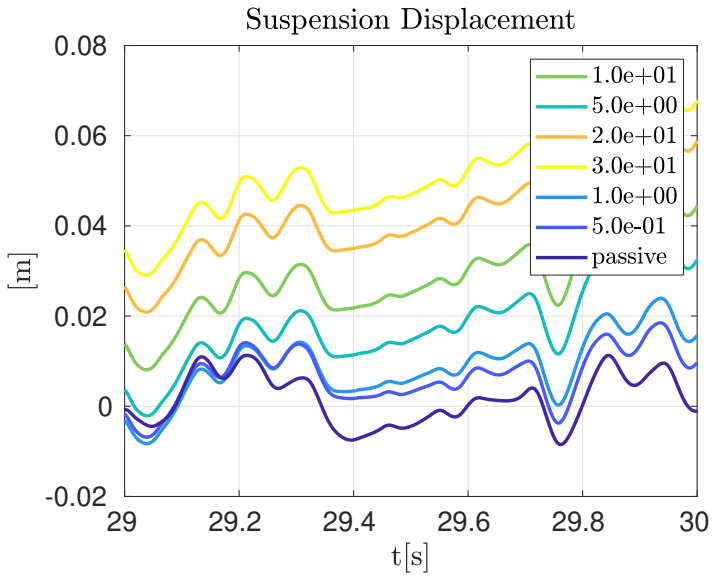

FIGURE A.5. Plot of Suspension Deflection vs Time with varying α_a weighting parameter.

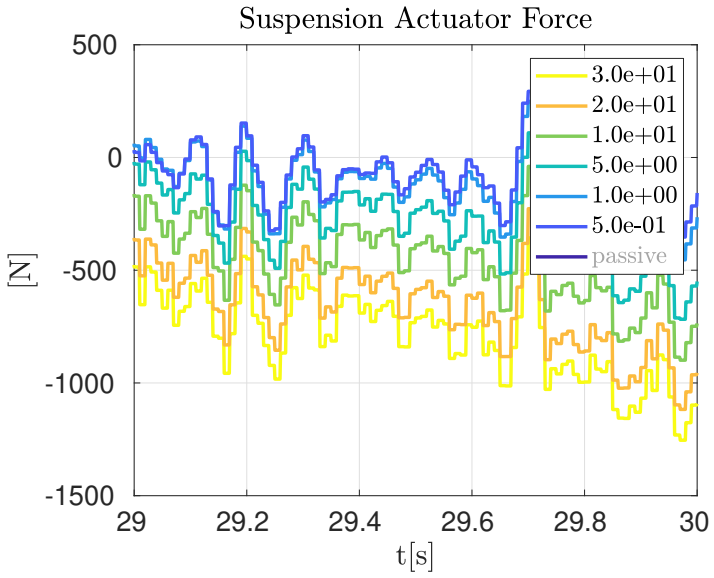

FIGURE A.6. Plot of Suspension Actuator Force vs Time with varying α_a weighting parameter.

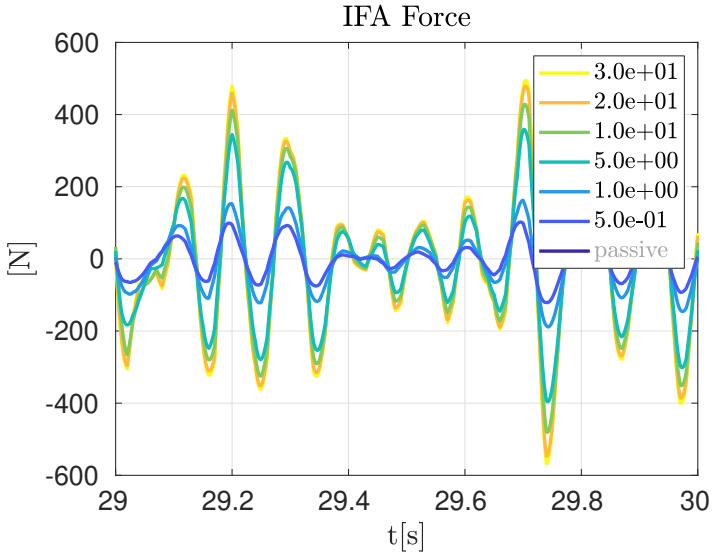

FIGURE A.7. Plot of IFA Force vs Time with varying α_a weighting parameter.

A.3. Additional plot outputs for section 4.2.2

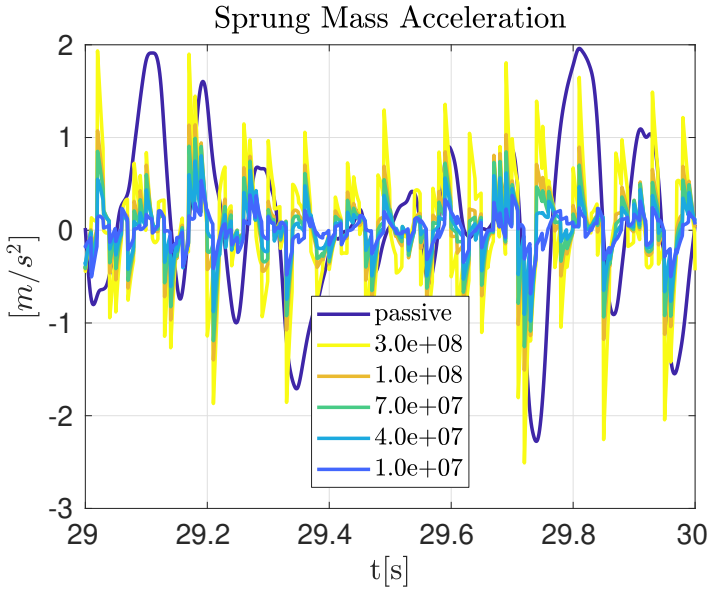

FIGURE A.8. Plot of Sprung Mass Acceleration vs Time with varying α_t weighting parameter.

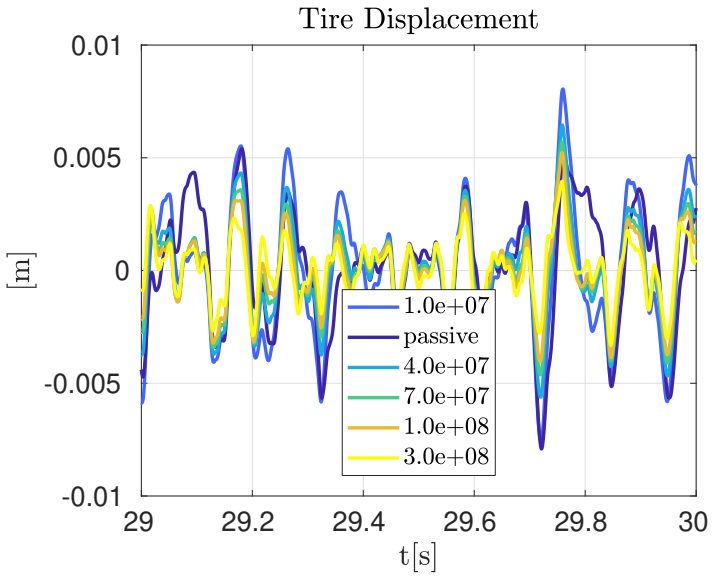

FIGURE A.9. Plot of Tire Deflection vs Time with varying α_t weighting parameter.

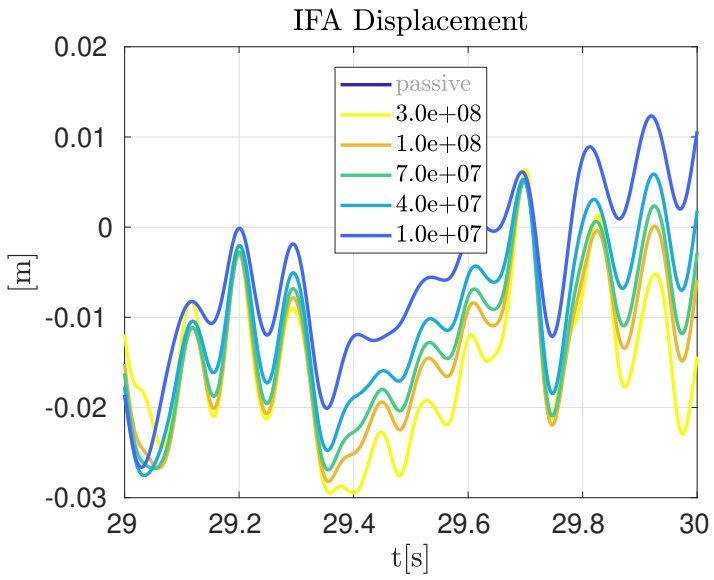

FIGURE A.10. Plot of IFA Deflection vs Time with varying α_t weighting parameter.

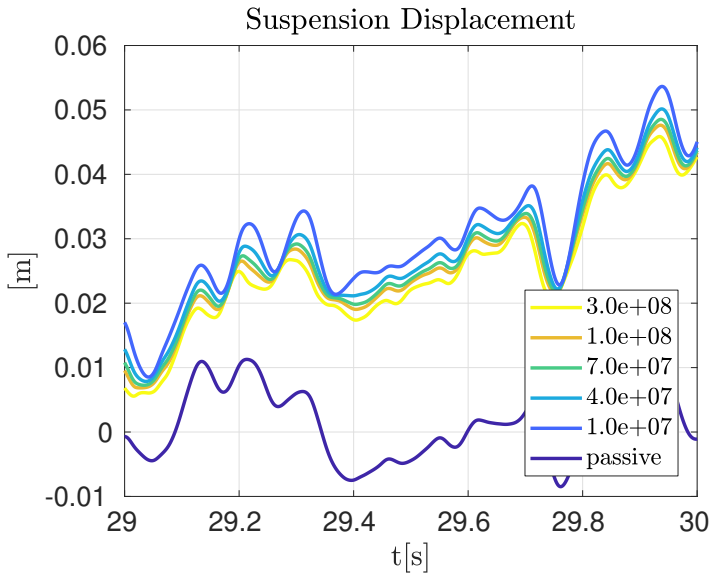

FIGURE A.11. Plot of Suspension Deflection vs Time with varying α_t weighting parameter.

A.4. Additional plot outputs for section 4.3.1

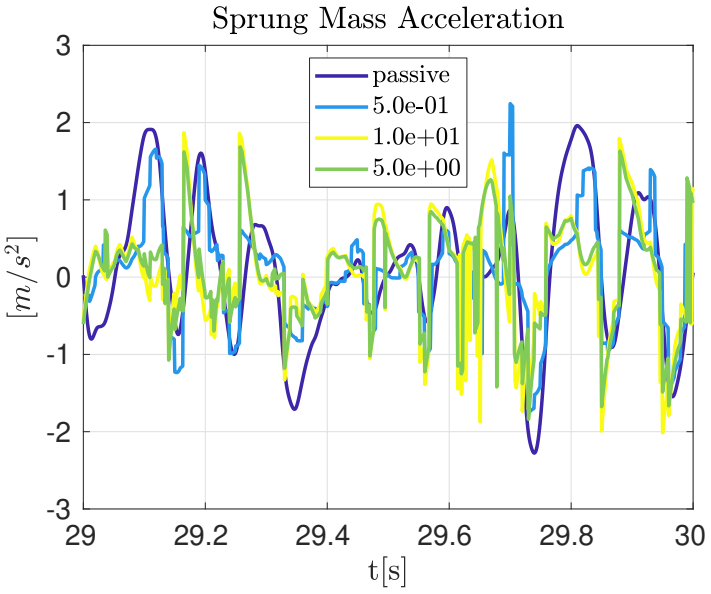

FIGURE A.12. Plot of Sprung Mass Acceleration vs Time with varying α_a weighting parameter.

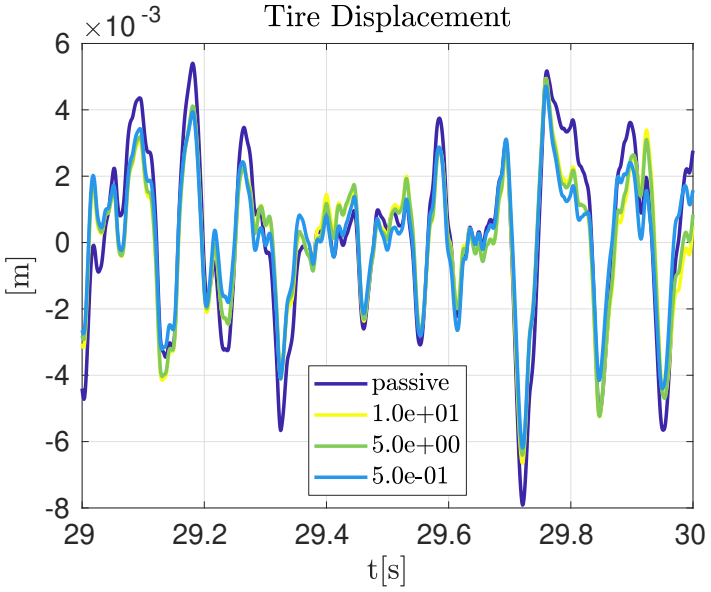

FIGURE A.13. Plot of Tire Deflection vs Time with varying α_a weighting parameter.

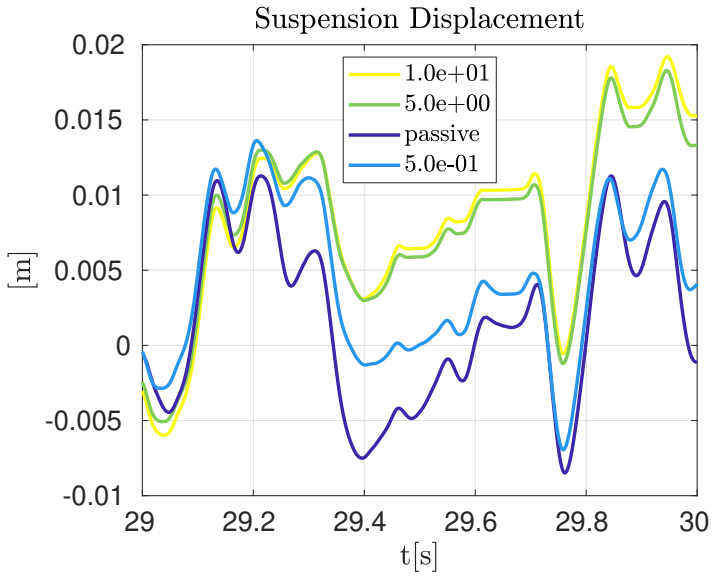

FIGURE A.14. Plot of Suspension Deflection vs Time with varying α_a weighting parameter.

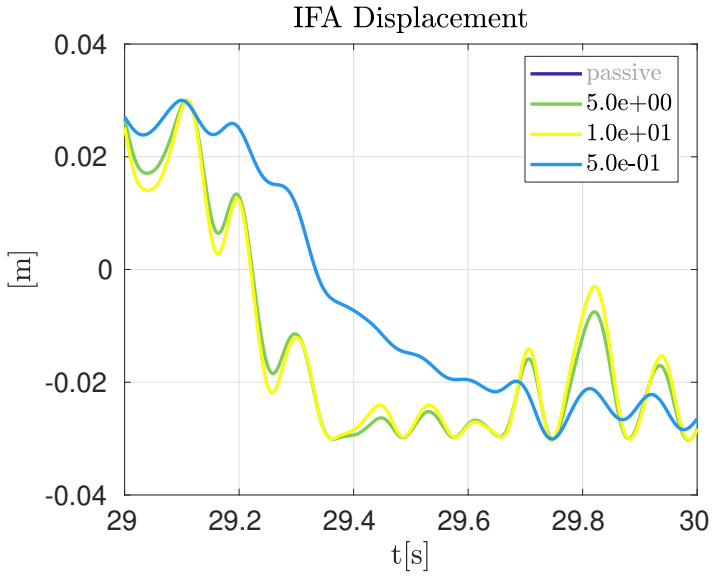

FIGURE A.15. Plot of IFA Deflection vs Time with varying α_a weighting parameter.

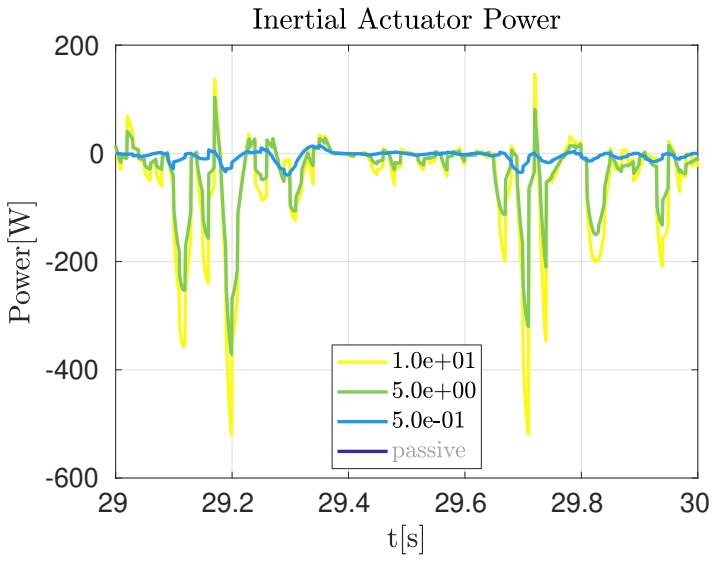

FIGURE A.16. Plot of IFA Power vs Time with varying α_a weighting parameter.

A.5. Additional plot outputs for section 4.3.2

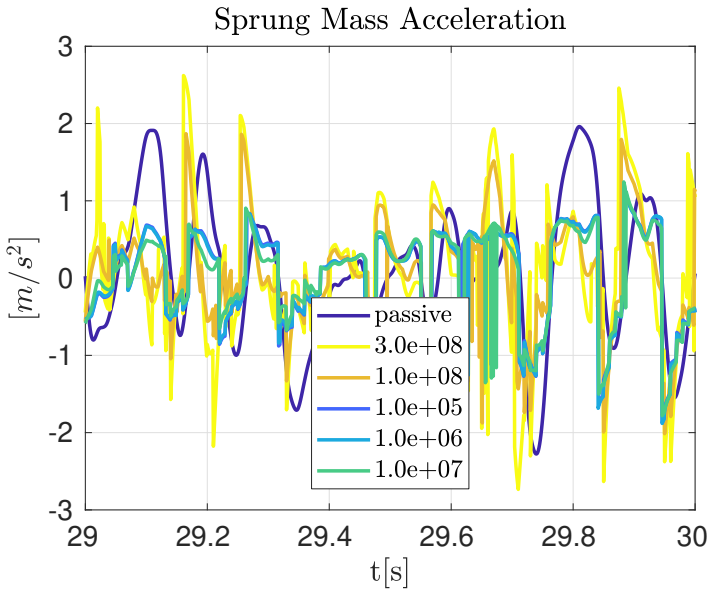

FIGURE A.17. Plot of Sprung Mass Acceleration vs Time with varying α_t weighting parameter.

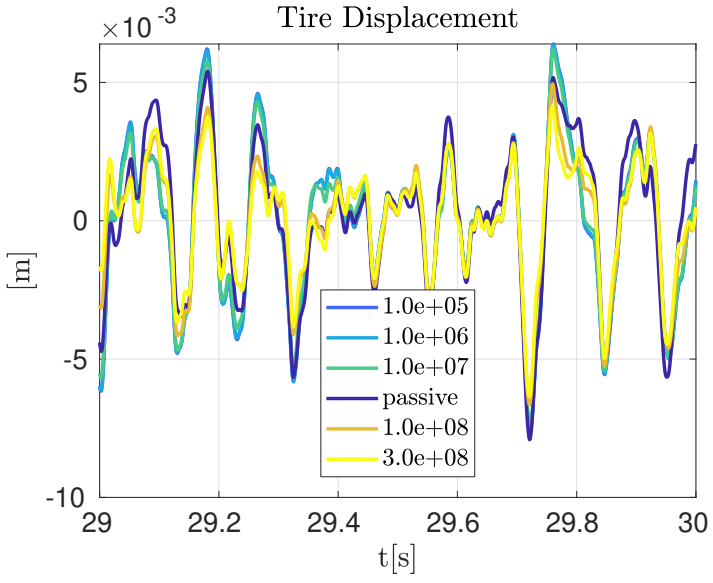

FIGURE A.18. Plot of Tire Deflection vs Time with varying α_t weighting parameter.

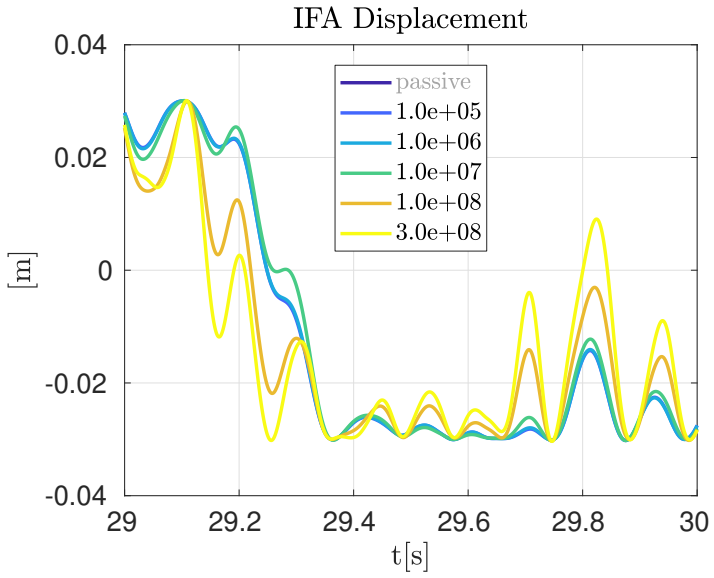

FIGURE A.19. Plot of IFA Deflection vs Time with varying α_t weighting parameter.

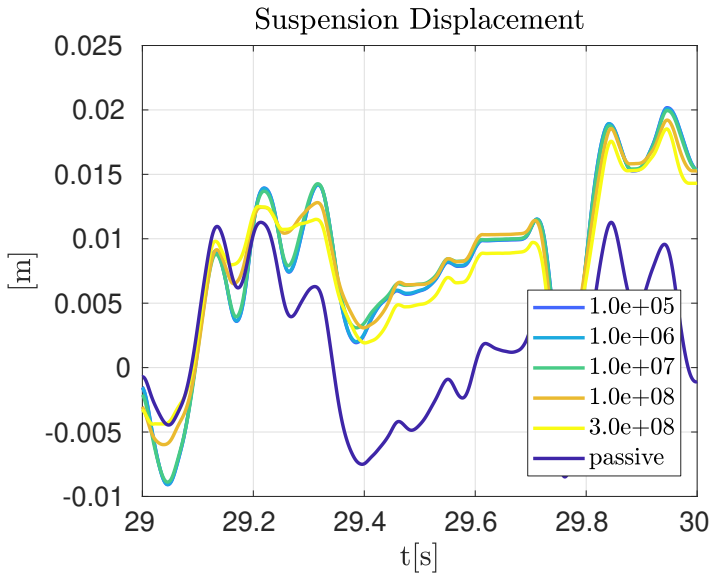

FIGURE A.20. Plot of Suspension Deflection vs Time with varying α_t weighting parameter.

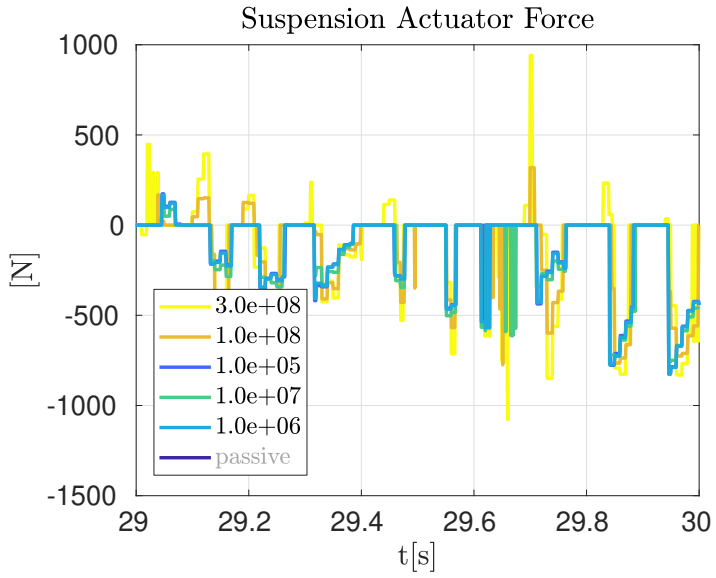

FIGURE A.21. Plot of Suspension Actuator Force vs Time with varying α_t weighting parameter.

FIGURE A.22. Plot of IFA Force vs Time with varying α_t weighting parameter. This plot shots how the suspension Force is obeying the passivity constraint.

A.6. Additional plot outputs for section 4.4.1

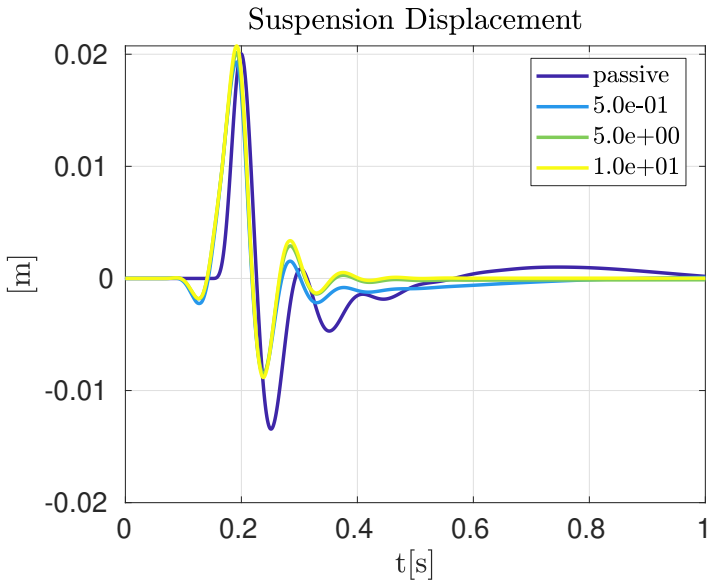

FIGURE A.23. Plot of Suspension Displacement vs Time with varying α_a weighting parameter.

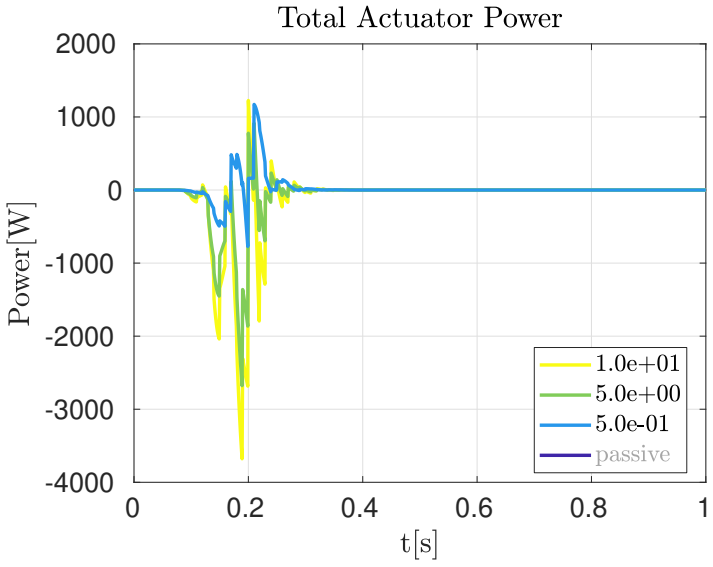

FIGURE A.24. Plot of Combined Actuator Power vs Time with varying α_a weighting parameter.

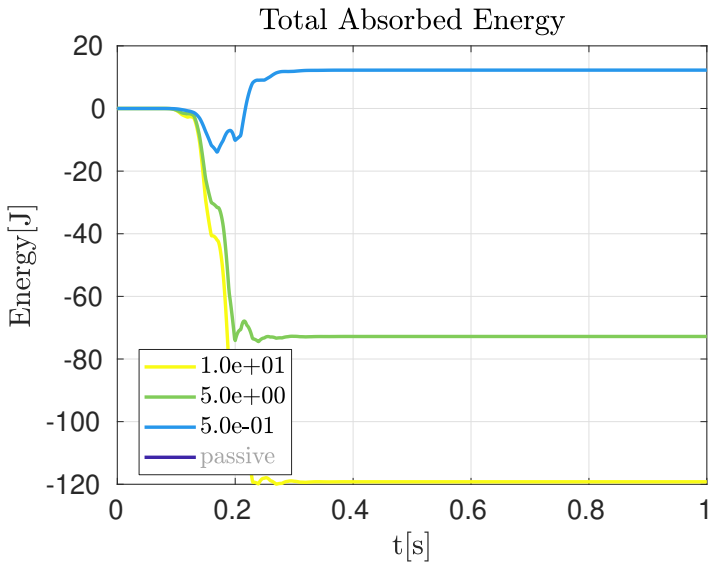

FIGURE A.25. Plot of Combined Actuator Energy Load vs Time with varying α_a weighting parameter. Note that for the smaller value of α_a, the actutors are supplying energy to the vehicle while meeting their primary targets.

A.7. Additional plot outputs for section 4.4.2

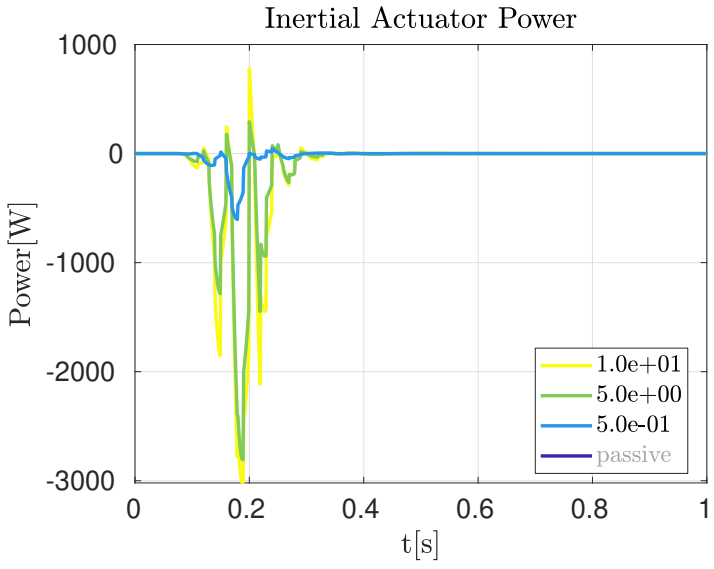

FIGURE A.26. Plot of IFA Power vs Time with varying α_a weighting parameter.

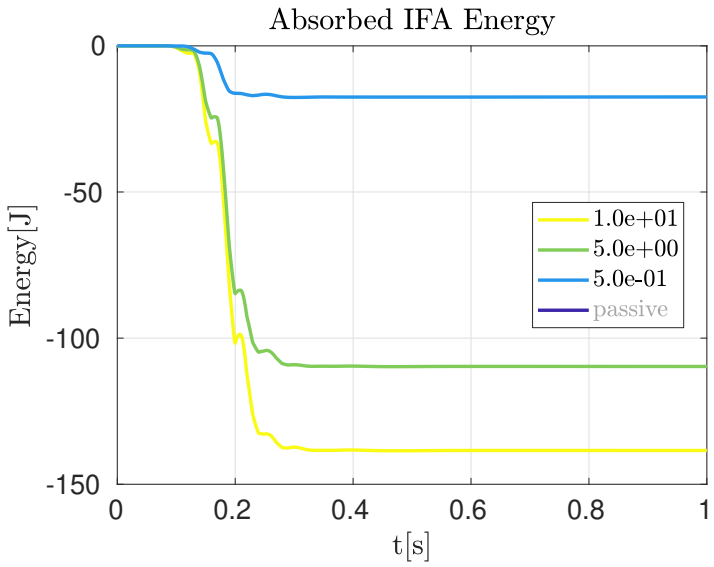

FIGURE A.27. Plot of IFA Energy Load vs Time with varying α_a weighting parameter.

.

Bibliography

[1] *Cylindrical Frameless Linear Voice Coil Actuator LA43-67-000A — Sensata Technologies.* https://www.sensata.com/cylindrical-frameless-linear-voice-coil-actuator-la43-67-000a.

[2] *Cylindrical Frameless Linear Voice Coil Actuator LA50-65-000A — Sensata Technologies.* https://www.sensata.com/products/motors-actuators/cylindrical-frameless-linear-voice-coil-actuator-la50-65-000a.

[3] *Inertial Force Actuators - Motran Industries, Inc.* http://www.motran.com/inertial-force-actuators.html.

[4] M. Agostinacchio, D. Ciampa, and S. Olita, *The vibrations induced by surface irregularities in road pavements – a Matlab® approach*, European Transport Research Review, 6 (2014), pp. 267–275.

[5] W. Belgacem, A. Berry, and P. Masson, *Active vibration control on a quarter-car for cancellation of road noise disturbance*, Journal of Sound and Vibration, 331 (2012), pp. 3240–3254.

[6] L. Benassi and S. Elliott, *Active vibration isolation using an inertial actuator with local displacement feedback control*, Journal of Sound and Vibration, 278 (2004), pp. 705–724.

[7] L. Benassi, S. Elliott, and P. Gardonio, *Active vibration isolation using an inertial actuator with local force feedback control*, Journal of Sound and Vibration, 276 (2004), pp. 157–179.

[8] F. Borrelli, A. Bemporad, and M. Morari, *Predictive Control for Linear and Hybrid Systems*, Cambridge University Press, 2017.

[9] I. M. Díaz, E. Pereira, M. J. Hudson, and P. Reynolds, *Enhancing active vibration control of pedestrian structures using inertial actuators with local feedback control*, Engineering Structures, 41 (2012), pp. 157–166.

[10] H. Dugoff, P. S. Fancher, and L. Segel, *An Analysis of Tire Traction Properties and Their Influence on Vehicle Dynamic Performance*, in International Automobile Safety Conference, Feb. 1970, p. 700377.

[11] S. J. Elliott, M. Serrand, and P. Gardonio, *Feedback Stability Limits for Active Isolation Systems with Reactive and Inertial Actuators*, Journal of Vibration and Acoustics, 123 (2001), pp. 250–261.

[12] D. Hrovat, *Influence of unsprung weight on vehicle ride quality*, Journal of Sound and Vibration, 124 (1988), pp. 497–516.

[13] I. ISO, *Mechanical Vibration and Shock-Evaluation of Human Exposure to Whole-Body Vibration-Part 1: General Requirements*, 1997.

[14] ———, *Mechanical Vibration—Road Surface Profiles—Reporting of Measured Data*, 2016.

[15] D. Karnopp, *Active Damping in Road Vehicle Suspension Systems*, Vehicle System Dynamics, 12 (1983), pp. 291–311.

[16] ———, *Vehicle Dynamics, Stability, and Control*, no. 221 in Dekker Mechanical Engineering, CRC Press, Boca Raton, FL, 2nd ed ed., 2013.

[17] B. S. Kim, C. H. Chi, and T. K. Lee, *A study on radial directional natural frequency and damping ratio in a vehicle tire*, Applied Acoustics, 68 (2007), pp. 538–556.

[18] D. Y. C. Leung and D. J. Williams, *Modelling of Motor Vehicle Fuel Consumption and Emissions Using a Power-Based Model*, in Urban Air Quality: Measurement, Modelling and Management, R. S. Sokhi, R. San José, N. Moussiopoulos, and R. Berkowicz, eds., Springer Netherlands, Dordrecht, 2000, pp. 21–29.

[19] H. Pacejka, *Tire and Vehicle Dynamics*, Elsevier, 2005.

[20] J. T. Salihi, *Energy Requirements for Electric Cars and Their Impact on Electric Power Generation and Distribution Systems*, IEEE Transactions on Industry Applications, IA-9 (1973), pp. 516–532.

[21] D. Sammier, O. Sename, and L. Dugard, *Skyhook and H8 Control of Semi-active Suspensions: Some Practical Aspects*, Vehicle System Dynamics, 39 (2003), pp. 279–308.

[22] D. Simon, *Optimal State Estimation: Kalman, H Infinity, and Nonlinear Approaches*, John Wiley & Sons, 2006.

[23] M. C. Smith and G. W. Walker, *Performance Limitations and Constraints for Active and Passive Suspensions: A Mechanical Multi-port Approach*, Vehicle System Dynamics, 33 (2000), pp. 137–168.

[24] Y. Suda, S. Nakadai, and K. Nakano, *Hybrid Suspension System with Skyhook Control and Energy Regeneration (Development of Self-Powered Active Suspension)*, Vehicle System Dynamics, 29 (1998), pp. 619–634.

[25] H. Tseng and J. Hedrick, *Semi-Active Control Laws - Optimal and Sub-Optimal*, Vehicle System Dynamics, 23 (1994), pp. 545–569.

[26] H. E. Tseng and D. Hrovat, *State of the art survey: Active and semi-active suspension control*, Vehicle System Dynamics, 53 (2015), pp. 1034–1062.

[27] M. Valášek, M. Novák, Z. Šika, and O. Vaculín, *Extended Ground-Hook - New Concept of Semi-Active Control of Truck's Suspension*, Vehicle System Dynamics, 27 (1997), pp. 289–303.

[28] R. A. Williams, *Automotive active suspensions Part 1: Basic principles*, Proceedings of the Institution of Mechanical Engineers, Part D: Journal of Automobile Engineering, 211 (1997), pp. 415–426.

[29] Y. Yao, G. Li, Y. Sardahi, and J.-Q. Sun, *Stability enhancement of a high-speed train bogie using active mass inertial actuators*, Vehicle System Dynamics, 57 (2019), pp. 389–407.

[30] M. Zilletti, *Feedback control unit with an inerter proof-mass electrodynamic actuator*, Journal of Sound and Vibration, 369 (2016), pp. 16–28.